공학박사학위논문

Vortex-induced Vibration Generated by Flow Interaction between Two Cable-stayed Bridges in Tandem

병렬 사장교의 유동장 간섭 현상에 의한 와류진동

2016 년 8 월

서울대학교 대학원
건설환경공학부
박 진

ABSTRACT

A vortex-induced vibration (VIV) was observed in the upstream deck of a pair of cable-stayed bridges in 2011. This represents the first case of such an observation in an actual long-span cable-supported bridge in service. The observed VIV was reproduced in a wind tunnel and a series of wind tunnel tests were carried out to identify causes of the VIV. The successful reproduction showed that the VIV was amplified by an interference effect caused by parallel arrangement of decks.

An in-depth study was conducted on the interactive vibrations in parallel arrangement. For the VIV, the gap distance between two decks was considered as the key parameter. The considered gap distances covered wide range from one to twenty times of the depth of deck. By variation wind velocity, the amplitudes of VIVs in both decks were estimated. Particle image velocimetry (PIV) tests were also performed to identify the change of streamlines in between two decks for different gap distances. Also the distribution of swirling strength of the generated vortices was evaluated from the velocity data obtained from PIV tests. Alternating eddies were formed in phase with the upstream deck motion and were transmitted to the downstream deck regardless of the gap distances. According to the research results, it can be concluded that the interactive VIV in two parallel cable-stayed bridges is critically affected by the gap distance up to five to seven times of the depth of the deck. This vulnerable gap distance

is closely related to the moving distance of one vortex during one-period oscillation of the deck.

Key Words: cable-stayed bridge, tandem arrangement, wind tunnel test, VIV, PIV, gap distance

Student Number: 2011-30983

Table of Contents

List of Figures

List of Tables

Chapter 1

Introduction

Jindo bridges are composed of a pair of cable-stayed bridges in tandem arrangement with close gap space (see Figure 1.1). Two bridges are constructed as twin bridges with similar structural concept and configuration. The total length of bridges are about 480m with a main span length of 340m. The left side bridge in Figure 1.1 was opened to traffic first in 1984, thus it is called the 1st Jindo Bridge. Then, the 2nd Jindo Bridge, the right side, was built in 2005.

On April 19, 2011, a wind-induced vibration was observed on the deck of the 2nd Jindo Bridge. Considering the wind velocity and the motional frequency, the abnormal vibration seemed to be a vortex-induced vibration (VIV). The 2nd Jindo Bridge had been reported on similar abnormal vibrations in several times since it was constructed. The extraordinarily large VIV in 2011, which exceeded the maximum allowable acceleration recommended by the serviceability criterion, caused a trouble. Although the VIV does not induce collapse of structure because of its self-limiting nature, it is possible to lead to fatigue and serviceability problems on the structure. Thus, the necessity for mitigation of VIV and investigation of causes arises to prevent a recurrence of the problem.

The VIV problem on the Jindo Bridges has following distinct characteristics; Two bridges have already equipped with vanes for mitigation of VIV on their decks; The 2nd Jindo Bridge oscillated at upstream in 2011; The 1st Jindo Bridge has not been reported about the VIV, although two bridges are similar in the structural concept and the outer configuration.

Figure 1.1. Jindo Bridges

1.1 Literature survey

Only a few studies on VIV of parallel bridges have been conducted in the past three decades. Most of them were issued in the design stage when a new bridge was constructed near an existing bridge. Those studies repeatedly mentioned that the interference effect due to the parallel disposition of bridges might lead to interactive vortex-induced vibration on bridge girders. Honda et al (1993) reported for a slender box girder bridge that the VIV was amplified by the aerodynamic interference and an increase of structural damping was an effective countermeasure for the interactive VIV. Small to medium sized cable-stayed bridges were investigated by Grillaud et al (1992) and Larsen et al (2000). Grillaud et al (1992) focused that the geometrical modifications of the upstream bridge allow to reduce the VIV of the downstream bridge, while Larsen et al (2000) highlighted the aerodynamic outcomes of bridges depended on whether the position of bridge was up or downstream. Meng et al (2011) reported interactive VIV for a pair of single tower cable-stayed bridges and proposed a strategy for mitigating the interactive VIV through investigation on fairing. They commented that large eddies were generated in the region between decks using a computational fluid dynamics approach. He and Li (2015) proposed another strategy attaching the grating of different opening ratio in the central slotting of the girders. Kimura et al (2008) conducted parameter study for the separation distance between two bridges. They reported that

the interference effect could be significant even with a separation distance as large as 8 times the deck width. It is worthy of notice that the separation distance of the Jindo Bridges is less than twice of the deck width. Irwin et al (2005) studied on Tacoma Narrows Bridges. They reported that neither significant VIV nor flutter instability was observed. Larsen et al (2000), Liu et al (2009) and Argentini et al (2015) also reported the interference VIVs. The previous studies focused on the specific case study and failed to carry out general conclusions. The VIV of Jindo bridges is possible to be affected by the interference effects due to tandem arrangement. Thus, it is necessary to the investigation on phenomena at Jindo Bridges and further study on interactive VIV at two bridges in tandem.

Since the limited number of studies exists on the aerodynamics of parallel bridges, the corresponding studies in other fields are introduced. Study on two cylinders is a representative case for the parallel structures in cross-flow because of its simplicity of geometrical configuration and applicability in various fields of engineering. Sumner (2010) reviewed numerous number of the last 20 years of publications about two static cylinders in cross-flow. Most of reviewed publications focused on the wake structure according to the relative positions between two cylinders. Among them, results about two cylinders in tandem arrangement are related with the parallel bridges. For the tandem cylinders, the flow patterns are divided into three categories as referred by Xu and Zhou (2004). Xu and Zhou (2004) investigated the Strouhal numbers with various

separation distances using hot-wire anemometers and LIF flow visualization. They reported that the Strouhal numbers could be categorized according to the center-to-center distance and each category showed distinct characteristics in the vortex structures. Although the aerodynamic configurations are different between cylinders and bridge decks, the fact categorizing the characteristics according to the separation distance is referable in parallel bridge problems. Vibrations of two cylinders were studied by Zdravkovich (1985) and Brika and Laneville (1999). Both studies concluded that the amplitude of the upstream cylinder is very close to that of the single cylinder regardless of gap distances.

In bridge engineering field, the studies on twin box girder have been conducted in the last 10-20 years. Effects of gap distance on the twin box girders have been also studied. The dynamic behaviors of them are still different with parallel bridges because the up and downstream girders are dynamically coupled. It is, however, expected that the twin box girders show more relative results about structure-flow interaction in static state. Larsen et al (2008) conducted pressure measurements for a twin box girder and investigated the vortex characteristics at different Reynolds numbers. They reported that the vortex shedding of parallel decks became stronger than that of single deck and high pressure fluctuations at downstream bridge was caused by impinging vortices shed from the upstream deck. Kwok et al (2012) conducted pressure measurements with various gap distances around sectional twin box model. They found that the pressure

distribution on the downstream section dramatically changed according to the gap distance, comparing that of the upstream section. Chen et al (2014) utilized pressure measurements and flow field observations with various gap distances around sectional twin box model. They categorized unsteady vortices and flow structures into two divisions according to the gap distance and reported that generation of vortices in the gap region was restricted when the ratio of open gap width to the deck height was below 1.70. Laima and Li (2015) observed the pressure distributions around sectional models, the Strouhal number and flow patterns. They divided the vortex shedding patterns into three categories according to the gap distances. The vortex shedding occurred behind the downstream deck in smaller gap distances; the upstream deck in moderate gap sizes; and both decks freely when the gap size approached infinity.

1.2 Objective and scope

Existence of the interactive vibrations in parallel bridges is identified through literature survey, but general conclusion on cause of the interactive vibrations is not proposed. Therefore, the preceding researches cannot explain the VIV observed at Jindo Bridges.

In this paper, for the investigation on interactive VIV of Jindo Bridges, this study utilizes the results from wind tunnel tests with 2-dimensional section models and aeroelastic analyses with aerodynamic parameters extracted from wind tunnel tests. It is difficult to draw the general conclusion on the interactive vibrations because of the complex geometrical configurations of deck sections with its own originality. Therefore, this study focuses on identifying the relationship between key parameters and phenomena.

Investigation of vortex-induced vibration is conducted by a series of wind tunnel tests with 2-dimensional section model. The separation distance between two decks is considered as the key parameter since its importance is obtained from the preceding researches. A particle image velocimetry (PIV) system is also utilized to analyze flow fields since it is known that the characteristics of VIV are closely related with the flow fields. Because the 2nd Jindo Bridge has experienced VIV problems, the investigations are conducted focusing on the situation of VIV in 2011. Therefore, the investigation is

limited in case of vertical VIVs. Through these investigations, the cause of VIV in 2011 and the relation between the gap distance and interactive VIV are identified.

Chapter 2

Similitude and setup in wind tunnel testing

2.1 Similitude for wind tunnel tests

For correct simulation in wind tunnel, the meaningful dimensionless parameters should be maintained constant from prototype to model. In general, a length scale, density ratio, Froude number, Cauchy number, or Reynolds number are considered for 2-dimesional section model test in wind tunnel (Tanaka, 1990). Each dimensionless parameter involves similarity scales for physical quantities. For example, if L_m and L_p are the representative length of model and of prototype, respectively, then the length scale, λ_L, is defined as

$$\lambda_L = \frac{L_m}{L_p} \tag{2.1}$$

Note that subscripts m and p keep to refer respectively to model and prototype in following discussion. The following sections discuss the consideration of similitude taken into this study. The consequence of distortion of the similitude requirement is examined for the correct interpretation of the results.

2.1.1 Length scale and scaled section models

Length scale can be arbitrary chosen by a researcher. Wind tunnel tests were conducted with 2-dimensional section models which were manufactured with the length scale of $\lambda_L = 1/36$. Figure 2.1 shows the manufactured section models. For the convenience of discussion, the 1st and 2nd Jindo Bridges are referred to as B1 and B2 hereafter. The scale is considered to use a large-scale section model as much as possible unless the blockage ratio exceeds 5%. The blockage ratios are summarized in Table 2.1. The section models are equipped for end plates of 0.40 m (width) 0.13 m (height) which are made of transparent acrylic plastic in order to observe flow field near the section models. The section models are made of balsa wood which guarantees enough stiffness for rigid body assumption. The reason why the models are painted black is also PIV tests near the section models. The model length is 0.9 m which corresponds to the length of 32 m in prototype. A grade exists in prototype. Since the maximum difference in elevation is, however, less than 90 mm, a grade is ignored in the models. The decks of B1 and B2 are equipped with barriers, handrails, inspection rails, vanes and cable anchorages. All of these details are successfully represented in the models with the consistent scale. The geometry and dimension of the section models are shown in Figure 2.2 and values in parentheses represent the dimensions for the prototype.

Table 2.1. Blockage ratio

	Cross sectional area of the test section of wind tunnel (C)	Model projected area normal to wind (S)	
		Single B1 or Tandem arrangement	Single B2
Area (m^2)	$1 \times 1.5 = 1.5$	$0.9 \times 0.078 = 0.070$	$0.9 \times 0.076 = 0.068$
Blockage ratio S/C (%)	-	4.7	4.5

a

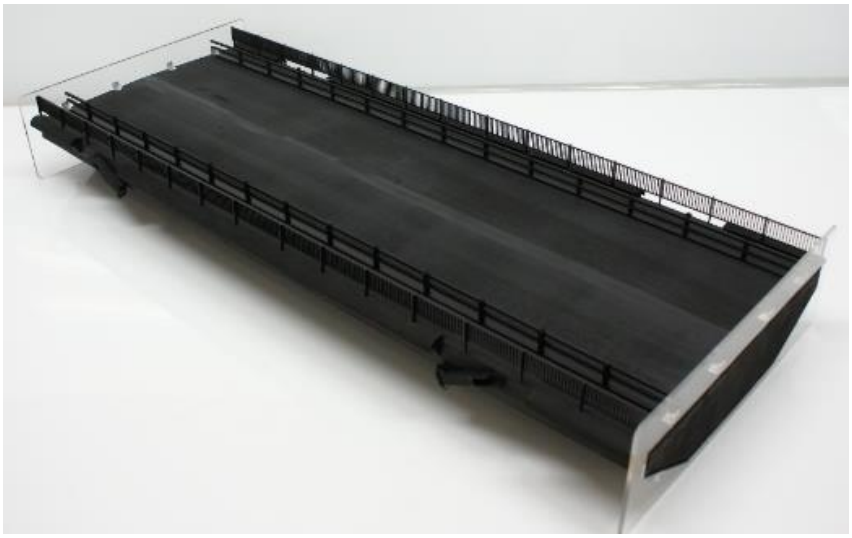

b

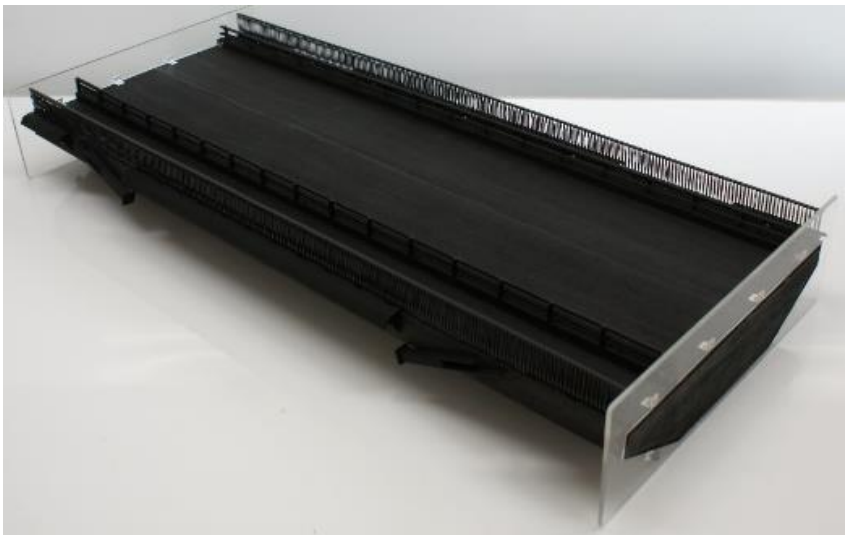

Figure 2.1. Section models of (a) B1 and (b) B2

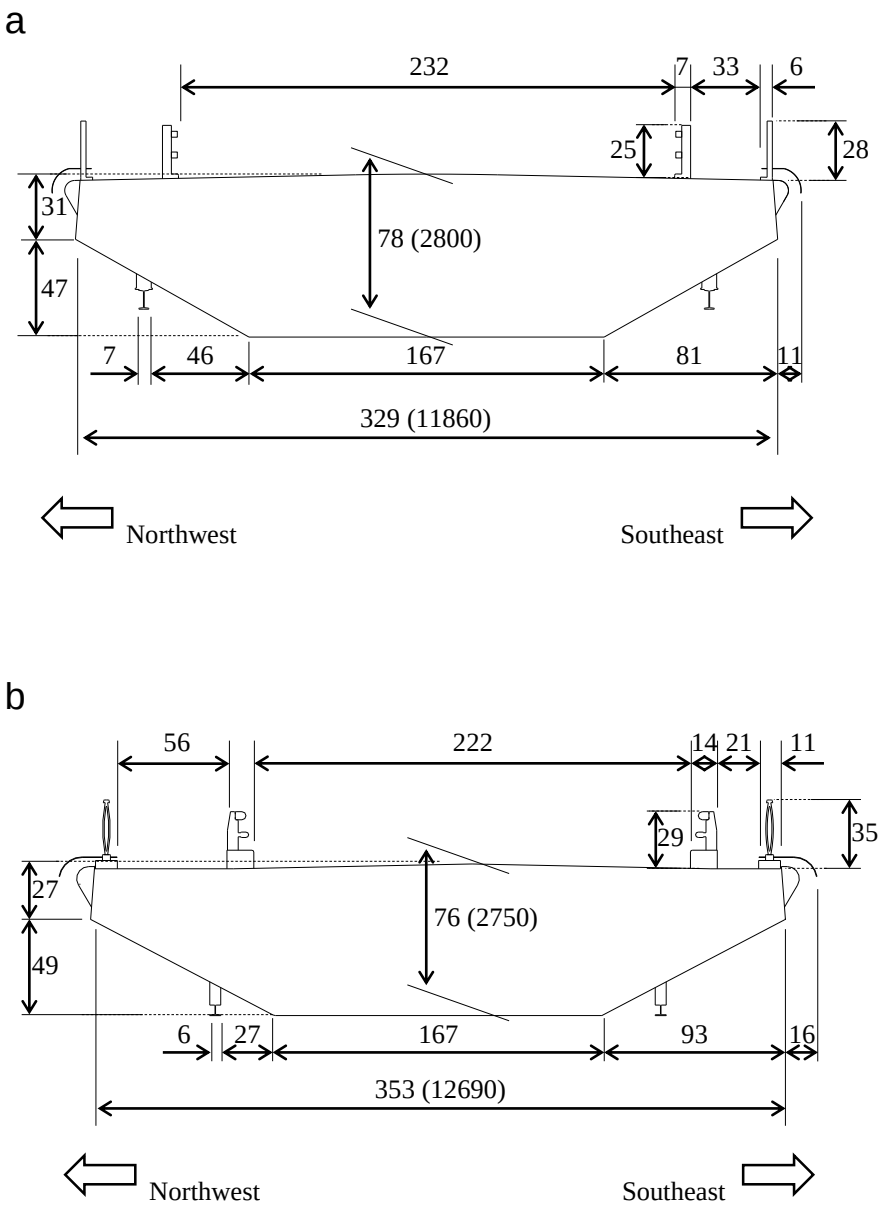

Figure 2.2. Dimension (mm) of section models (Values in parentheses represent the dimensions for the prototype): (a) B1 and (b) B2

2.1.2 Density ratio

The density ratio means the ratio of density between the structure and fluid. It is related with inertia force. During the wind tunnel test, the density of fluid is fixed since the test is performed in air as same as that surrounding the prototype. Thus, the density of structure should be same at prototype and model. If ρ is density of the structure, then a density scale, λ_ρ, is defined as

$$\lambda_\rho = \frac{\rho_m}{\rho_p} \tag{2.2}$$

The density scale is fixed as $\lambda_\rho = 1$. In general, the aeroelastic model is the equivalent model instead of the exact replica. It means that the aeroelastic model simply imitates the outer configuration and dynamic properties. In this case, the density ratio can be replaced by the mass ratio or the mass moment of inertia ratio according to the mode. Let *m* is mass per unit length, then the density scale for vertical mode is determined by the length scale as following,

$$\lambda_\rho = \frac{m_m}{m_p} = \frac{L_m^2}{L_p^2} = \lambda_L^2 \tag{2.3}$$

For the torsional mode the mass per unit length is replaced by the mass moment of

inertia per unit length, *I*, then the density scale for torsional mode is defined as

$$\lambda_\rho = \frac{I_m}{I_p} = \frac{L_m^4}{L_p^4} = \lambda_L^4 \tag{2.4}$$

2.1.3 Froude number and Cauchy number

Froude number is the ratio of fluid inertia force to vertical force due to gravity and Cauchy number is the ratio of structural elastic force to fluid inertia force. Physically, two dimensionless parameters are quite different but technically it is determined depending on a frequency scale, λ_f, in wind tunnel. The frequency scale is the ratio of the natural frequency, *f*, of model to prototype. In Froude number similitude, the frequency scale should be following relation

$$\lambda_f = 1/\sqrt{\lambda_L} \tag{2.5}$$

According to this relation, the frequency scale is set to $\lambda_f = 6$ as long as Froude number similitude is adopted. Gravitational effects are required for certain cases, e.g. suspension bridges. For 2-dimensional section model test, Froude number similitude is excluded. Because the restoring force of structure is provided only by its linear elastic properties which are simulated by linear elastic coil springs. The gravitational effect

does not affect aeroelastic responses of section model.

In Cauchy number similitude, the frequency scale can be arbitrary chosen by a researcher as long as the density ratio is taken into the consideration. In most wind tunnel tests, rather than the original definition of Cauchy number, a following form is utilized

$$Ca = \left(\frac{fL}{V}\right)^2 \lambda_\rho \tag{2.6}$$

where V is wind velocity. A new dimensionless parameter, V/fL, is called the reduced velocity. Cauchy number similitude allows that the aeroelastic responses can be analyzed as a function of reduced velocity. This implies that the aeroelastic responses with arbitrarily chosen for the frequency scale show same results at the same reduced velocity. Thus, testing over a wide range of reduced velocity to cover necessary range in reality is usually not a difficult.

To verify the effects of frequency scale, the test results according to the frequency scale are shown in Figure 2.3. The results show the vertical single amplitudes of B2 under various wind speeds. The frequency scale varies from 4.8 to 11.7 which covers the scale due to Froude number similitude. Vortex-induced vibration is clearly observed from wind speed of 10 m/s to 14 m/s regardless of the frequency scale. In the case of

amplitude, values are different up to 20%. As the tendency of response is consistent, Cauchy number similitude using the reduced velocity is proper to analyze vortex-induced vibration phenomena.

The low frequency scale allows to observe aeroelastic responses at high wind speed within the maximum wind speed of wind tunnel. However, the resolution of wind speed becomes bad. In contrast, the high frequency scale can improve the resolution of wind speed. Another problem of high frequency scale is difficulty of setup because the stiffness of coil spring increases by square of the frequency scale. Since this study focuses on VIVs at relatively low wind speed, the frequency scale is set to high value of $\lambda_f = 11.7$ as much as possible. It is almost twice larger value than $\lambda_f = 6$ which is according to Froude number similitude.

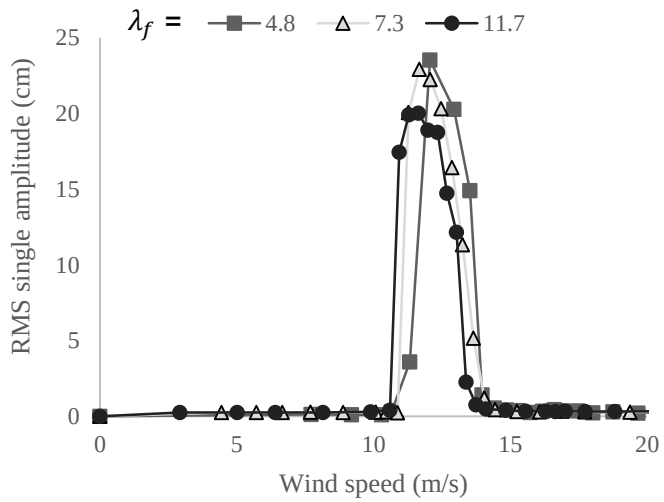

Figure 2.3. Aeroelastic responses of B2 according to the frequency scale

2.1.4 Reynolds number

Reynolds number that is the ratio of the fluid inertia force to the fluid viscose force is an important parameter in flow induced phenomena. It affects the flow pattern because of the shift of flow separation points with the change of it. However, it is impractical to satisfy Reynolds number similitude in most of wind tunnel tests. Because it requires simply that $\lambda_V \lambda_L = 1$ or

$$\lambda_V = \frac{1}{\lambda_L} \tag{2.7}$$

where , λ_V is velocity scale which is defined as following

$$\lambda_V = \frac{V_m}{V_p} \tag{2.8}$$

Briefly, a model with reduced geometric scale requires increased wind speed in testing. Furthermore, even wind tunnel can provide proper speed, only static experiment can be conducted. For the dynamic testing, Reynolds number similitude conflict with Froude number or Cauchy number similitude. Another view of the same effect is that, under the prior setting of length and frequency scales, Reynolds number is distorted:

$$\frac{(Re)_m}{(Re)_p} = \lambda_V \lambda_L = \lambda_f \lambda_L^2 = 0.0090 \approx 0.01 \tag{2.9}$$

The consequence of this huge distortion of Reynolds number is carefully examined for the correct interpretation of the results.

There is a general belief that in case of the structure with sharp corners like bridge girders, the flow separation position is fixed at those corners and the flow pattern is less sensitive according to the Reynolds number. Hence, the effect of Reynolds number have been ignored in bridge aerodynamics. However, since Schewe and Larsen (1998) reported that Reynolds number affects the Strouhal number and static load coefficients of a bridge deck, Reynolds number is considered as an important parameter depending on the bluff bridge deck cross section (Lee et al, 2013; Matsuda et al, 2001; Schewe, 2001).

To analyze Reynolds number effects of the target bridge section, wind tunnel testing results according to Reynolds number are compared to monitoring data of prototype. Figure 2.4 shows the Strouhal number of the target bridges according to Reynolds number. The Strouhal numbers are measured by a hot-wired anemometer in wind tunnel in static condition. The values of prototype is estimated by the wind velocity and motional frequency of deck during the VIVs that one is observed in 2011 with seasonal wind and another is observed in 2012 with typhoon Tembin. The result shows that there

is no significant gap between Strouhal numbers of prototype and model despite Reynolds number difference. Figure 2.5 shows the peak amplitude of VIV of B2 which is placed upstream in tandem arrangement. The monitoring results are obtained also B2 positioned upstream. Wind speeds for the peak amplitudes show similar results regardless of Reynolds number. It is well matched with the Strouhal number result. In the case of amplitude, since wind tunnel tests are conducted at lower damping ratio condition that that of prototype, the results from test show relatively large values. Also, turbulence conditions are not considered in wind tunnel. Even the amplitude of prototype in 2011 and 2012 are different because the amplitude of VIV is sensitive to the wind conditions: wind speed, turbulence intensity, and time duration of wind. The experimental results in Figure 2.5 were obtained from independent setup conditions. Thus the amplitude of VIV are scattered due to the unexpected error of setup parameters, but any obvious tendency between amplitude and Reynolds number is not observed. This implies that whether Reynolds number effect on amplitude of VIV does not exist or do minor role compared to error of other parameters. Whichever is correct, although the absolute value of amplitude from wind tunnel cannot be used to interpret circumstance of prototype, the relative amplitude according to situations with a consistent setup is still useful to understand phenomena. Thus, the final setup parameters for section models are summarized in Table 2.2. The natural frequencies of prototype are referred to HDEC (2000) for B1 and Jang et al (2010); Spencer Jr et al

(2011) for B2. The critical damping ratio, ζ, is obviously an important parameter for the structural responses. In most cases the damping ratio was set to a minimum level of 0.1% for a better observation of vibrations.

Table 2.2. Setup parameters

Parameters	Similarity scale	B1		B2	
		Prototype	Model	Prototype	Model
Length (m)	$\lambda_L = 1/36$	32.400	0.900	32.400	0.900
Breadth (m)	λ_L	11.860	0.329	12.690	0.353
Depth (m)	λ_L	2.800	0.078	2.750	0.076
Aspect ratio	1	4.236	4.218	4.615	4.645
Mass (kg/m)	λ_L^2	6950	5.400	8978	6.874
Mass moment of inertia (kg m^2/m)	λ_L^4	84030	0.051	152.836	0.090
Vertical frequency (Hz)	λ_f =11.7	0.513	5.785	0.436	5.096
Torsional frequency (Hz)	λ_f =11.7	1.490	17.21	1.834	21.40
Vertical damping ratio (%)	1	0.5-0.7	0.1	0.2-0.3	0.1
Torsional damping ratio (%)	1	-	0.1	-	0.1

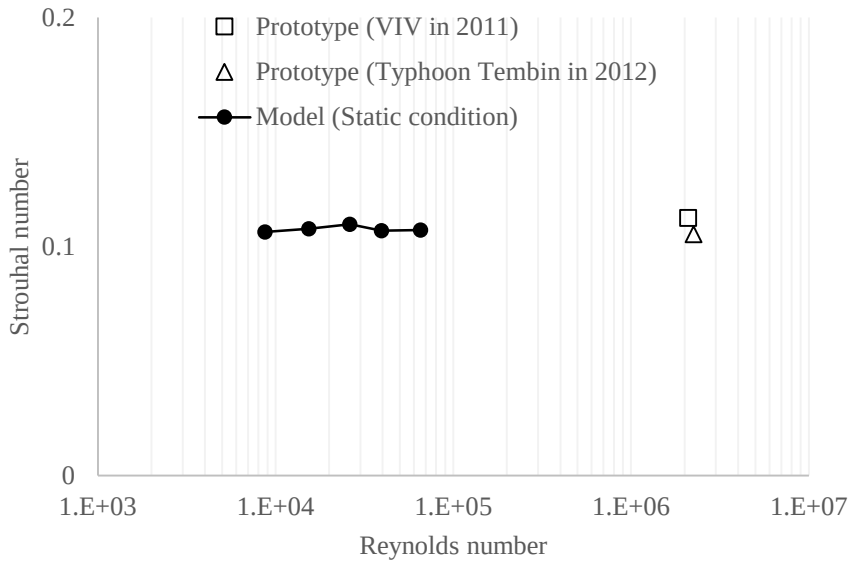

Figure 2.4. Strouhal number of the target bridge according to Reynolds number

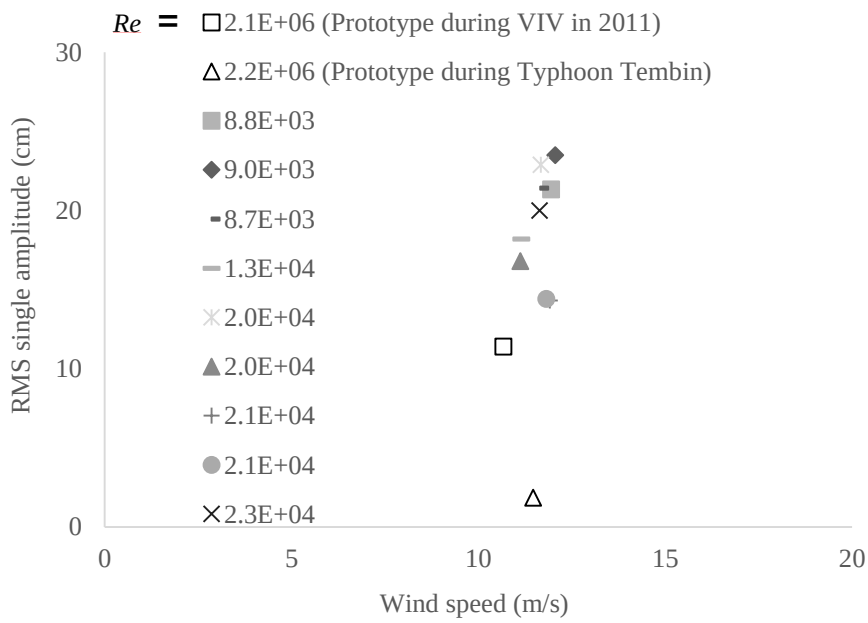

Figure 2.5. Peak amplitude of VIV of B2 according to Reynolds number

2.2 Setting for wind tunnel tests

All experiments were carried out in the wind tunnel of Department of Civil and Environmental Engineering at Seoul National University, Korea (see Figure 2.6). The test section of the wind tunnel is 1.5 m in height, 1.0 m in width and 4.0 m in length. The maximum wind velocity of the wind tunnel is 23 m/s.

Two decks of Jindo Bridge are closely spaced with a net distance of 10m between them as shown in Figure 2.7. B1 is placed at the southeast and B2 is placed at the northwest. Both the section models were separately mounted on spring-supported systems which permit vertical and torsional motions of the models with the consistent length scale as shown in Figure 2.7. It would be preferable to express the gap distance in terms of non-dimensional values for the identical representation between a prototype bridge and a wind tunnel model. The gap distance in non-dimensional forms as L/D, where L is the gap distance between two decks, D is the depth of upstream deck, as shown in Figure 2.8. Figure 2.9 shows the section models installed in wind tunnel.

The sensor deployment is shown in Figure 2.10. The vertical and torsional displacements of two decks were measured by total 8 (4 for each section model) laser displacement transducers with the sampling frequency of 500 Hz. The upcoming wind velocity was measured with a Pitot tube located in front of decks. A high-resolution PIV system was composed of a high resolution, two-mega pixel CCD camera, a double-

pulsed ND:YAG laser device emitting two pulses of 135 mJ at the wavelength of 532 nm, a seed generator spreading fine olive oil droplets of 1 μm and a trigger generator.

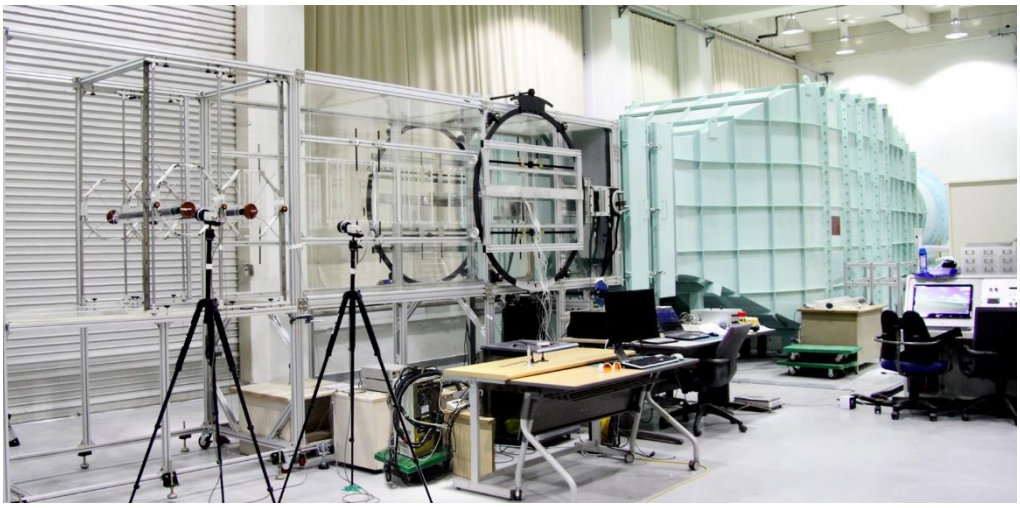

Figure 2.6. Wind tunnel of Department of Civil and Environmental Engineering at Seoul National University

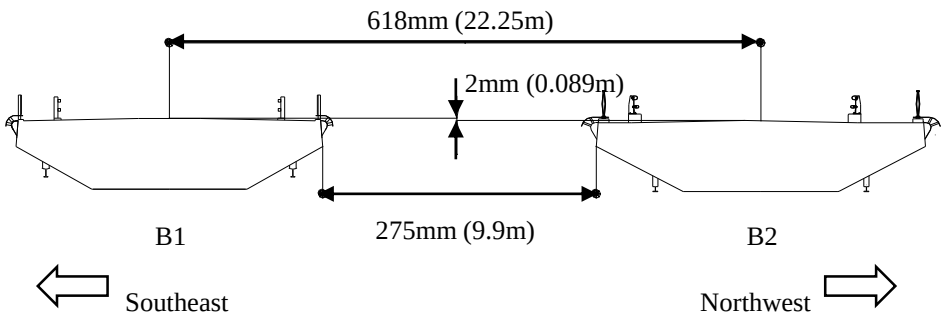

Figure 2.7. Disposition of the decks in wind tunnel (Dimensions for the prototype are shown in parentheses)

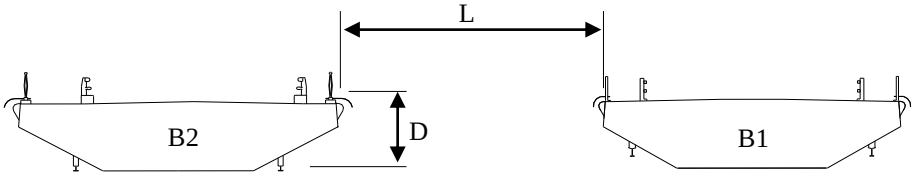

Figure 2.8. Nomenclature of wind tunnel tests

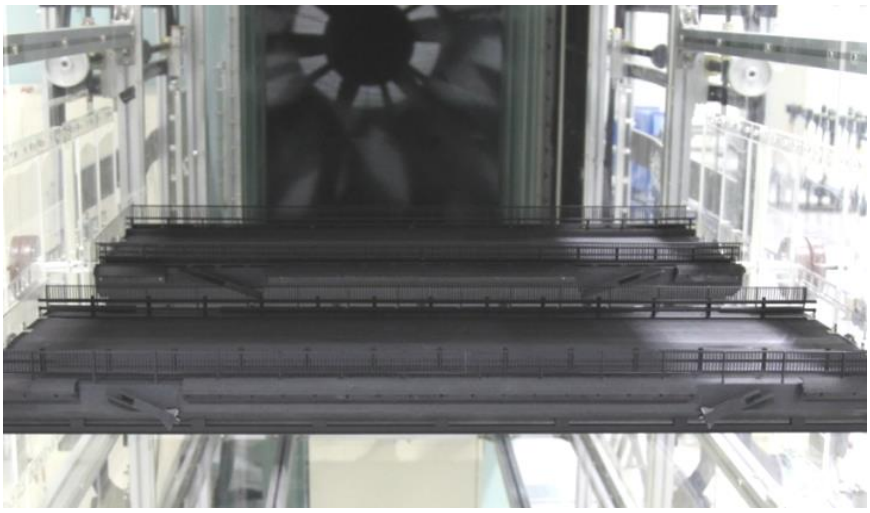

Figure 2.9. Installation of section models in wind tunnel

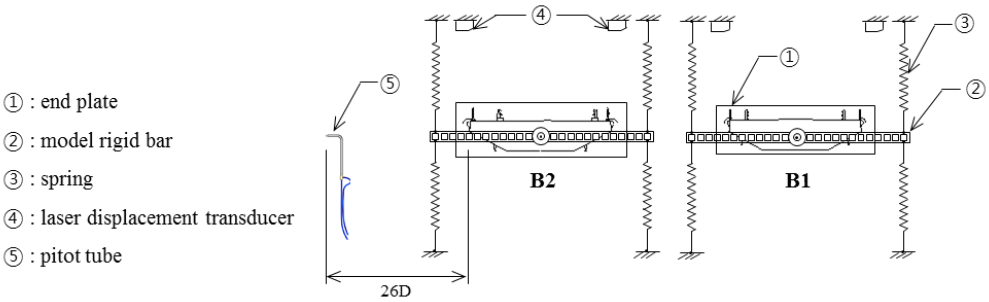

Figure 2.10. Sensor deployment

Chapter 3

Vortex-induced vibration of Jindo Bridges

3.1 Field observation of VIV of Jindo Bridges

3.1.1 VIV due to the seasonal wind

The vibration of B2 in 2011 was recorded by the built-in monitoring systems installed in two bridges, as shown in Figure 3.1. Although an anemometer had been installed on the deck of B2, it was temporarily unavailable. The wind velocity that was measured with sampling frequency of 10 Hz by an ultrasonic anemometer installed on one side of the deck of B1. Time series of observed wind speed is shown in Figure 3.2. The several spikes in Figure 3.2 seems to be originated from the malfunctioning of the sensor. However, the number of spikes is limited, so it is negligible to estimate the 10-minute averaged wind velocity. The 10-minute averaged wind velocities estimated by a moving average method are shown in Figure 3.2 with a broken line. Since the anemometer was installed only at a height of 3 m above deck surface and placed on the downstream bridge, the measured wind might be disturbed by two decks. The effect of this on the mean wind velocity was estimated by the wind tunnel test. The observed wind blew from the northwest and B2 was located upstream providing a normal disposition to the arriving wind.

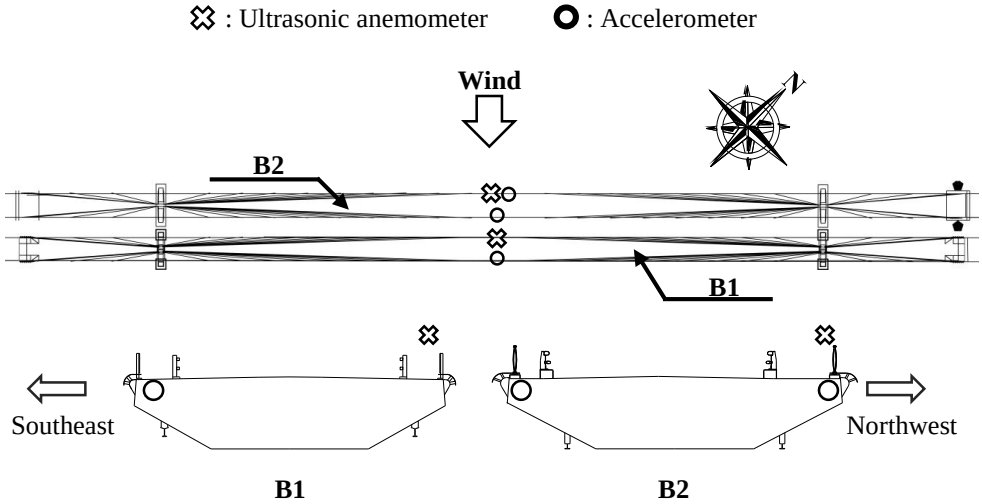

Figure 3.1. Built-in monitoring sensors used for the observation of VIV

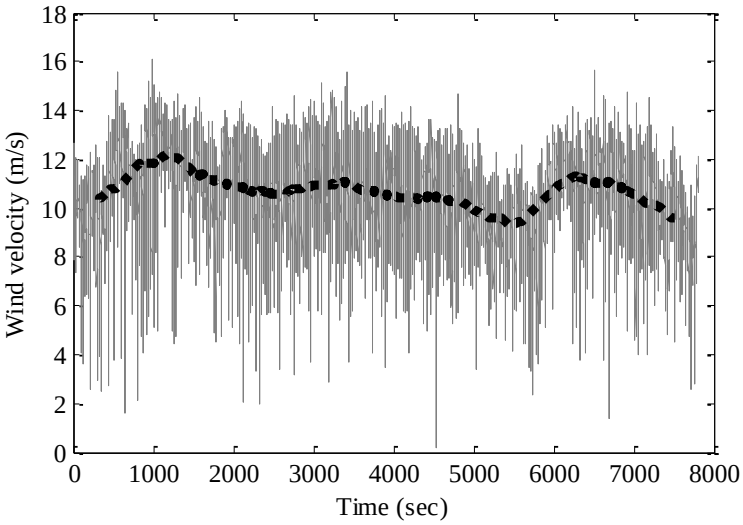

Figure 3.2. Observed wind velocity on the deck of B1 (gray) and 10-minute moving average (black)

Figure 3.3 shows the vertical acceleration of the deck of B2 obtained from accelerometers installed on both sides of the deck at the center of main span (see in Figure 3.1). As shown in Figure 3.4, the spectral density of the acceleration clearly indicates that B2 vibrated in its 1st vertical mode. According to a design guideline for steel cable-supported bridges (KSCE, 2006), the maximum allowable acceleration is recommended to be less than 0.5m/s^2 up to a wind velocity of 25 m/s at a deck level to satisfy the serviceability performance. The observed acceleration in Figure 3.3 exceeded this allowable limit, and the 10-minute averaged wind velocity was less than 25 m/s during the time when acceleration exceeded the allowable range.

The observed vibration is judged to be a VIV because relatively low wind velocity and vibration in single mode with self-limiting amplitude are representative characteristics of VIV. The observation of the VIV on two parallel cable-stayed bridges which were in-service was the first such case.

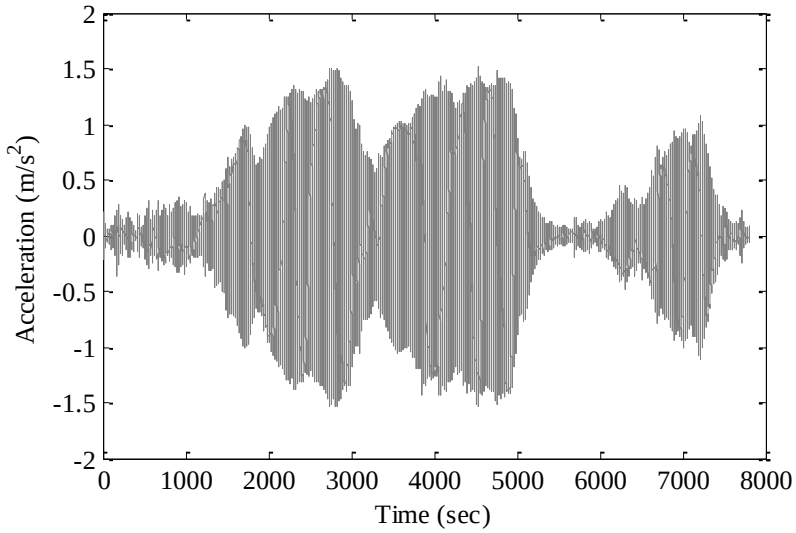

Figure 3.3. Observed acceleration at the center of the main span of B2

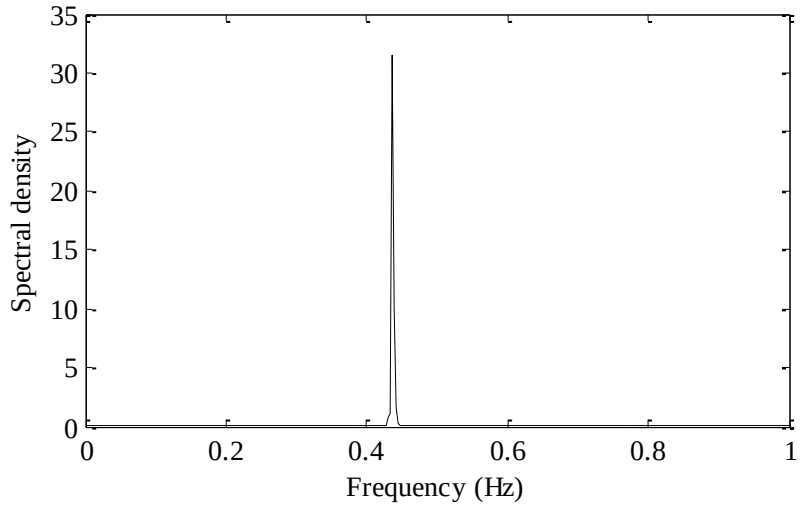

Figure 3.4. The spectral density of the acceleration

3.2 Reproduction of the observed VIV in the wind tunnel

3.2.1 Mean wind speed near deck section

Since the ultrasonic anemometers in monitoring system were placed near the deck, measured wind data may be disturbed. To estimate the disturbance of the mean wind speed, the mean wind profiles are measured with a hot-wire anemometer as illustrated in Figure 3.5. For the downstream deck, the ratio of wind speed above handrail, V_{hot}, to free stream wind speed, V, increase from 0.6 to 1.10 according to the height from surface as shown in Figure 3.6. For the upstream deck, the ratio decrease from 1.2 to 1.0 as shown in Figure 3.7. The installation support of ultrasonic anemometer stands three meters tall in height, and it is 1.1 times the depth of deck. According to the wind tunnel tests, the mean wind speed in Figure 3.2 seems to be as same as the free stream wind speed. The VIV in 2011 occurred with the 10-minute average wind speeds of 9-12 m/s. which corresponded to the reduced velocity of 7.5-10.

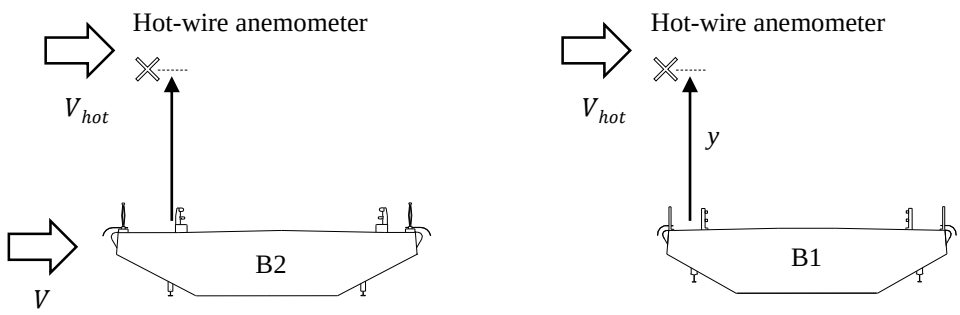

Figure 3.5. Setup of wind profile measuring

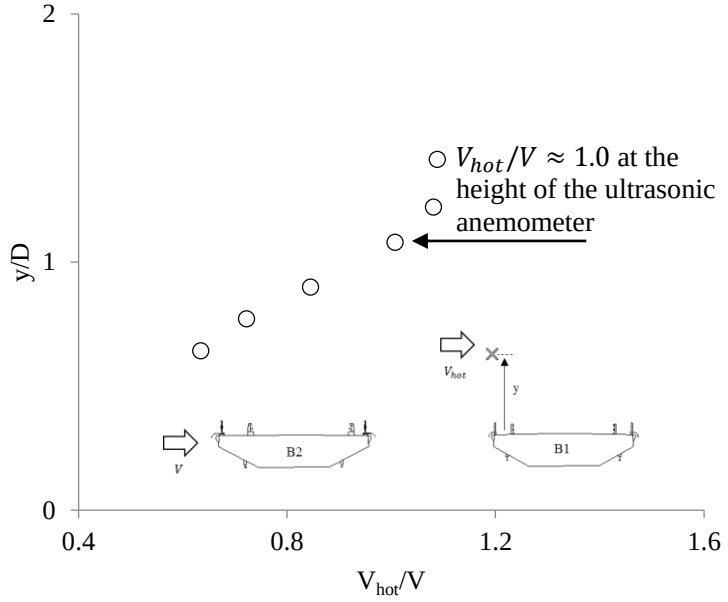

Figure 3.6. Wind profile above the girder of B1

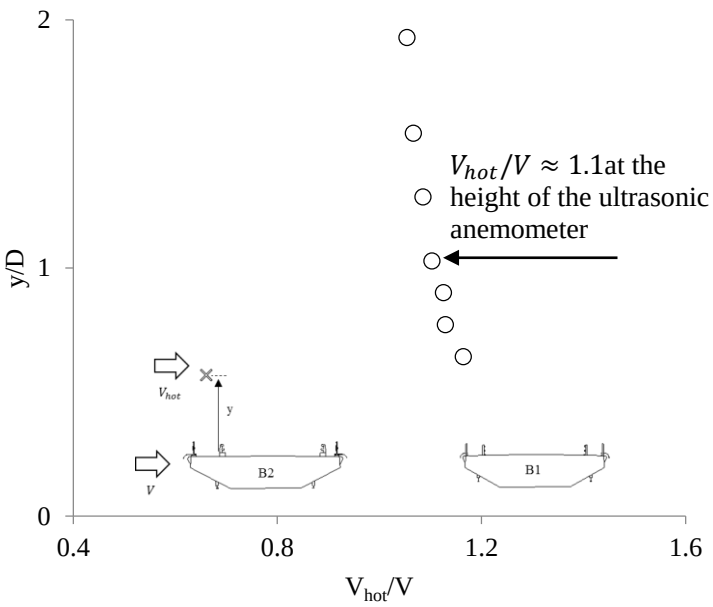

Figure 3.7. Wind profile above the girder of B2

3.2.2 VIV of the single stand-alone bridges in smooth flow

Prior to investigation for the parallel arrangement of bridges, the aerodynamic behavior of the single stand-alone bridge is evaluated in smooth flow with a turbulence intensity of less than 1%. The high frequency setup is utilized in a series of VIV test. Figure 3.8 shows the relationships between the maximum RMS single amplitudes of vertical vibration and wind velocities (A-V curves) of each single deck. The amplitudes are obtained at fully-developed VIVs for each wind velocity. For a non-dimensional representation, RMS responses in single amplitude for both decks are divided by the depth (D) of B2. Note that the damping ratios of two decks are set to a minimum level of 0.1% for a better observation of vibration. For the case of a minimum level of damping ratio, two sections show conventional VIVs for heaving motion.

The vertical VIVs begin to occur at the almost same wind velocity of 9.6 m/s in spite of the difference between vertical frequencies. To analyze this, the Strouhal numbers are estimated. The Strouhal number can be written as

$$St = \frac{f_v \cdot D}{V} \tag{3.1}$$

where, St is the Strouhal number and f_v is the vortex-shedding frequency. The vortex-shedding frequency is measured by a hot-wire anemometer behind the section of which

the motion is artificially restrained. Figure 3.9 and Figure 3.10 show the change in vortex shedding frequencies as a function of wind velocity for the single case of B1 and B2, respectively. The Strouhal numbers of B1 and B2 are identified to be 0.145 and 0.124, respectively, normalized by the depth of each deck.

The conventional VIV is known to occur at wind velocity in which the vortex-shedding frequency is tuned to the natural frequency of structure, i.e., $f_v = n$. Introducing this relation into the equation 3.1, the reduced velocity of VIV, $(V/\mathrm{nD})_{\mathrm{VIV}} = V/f_v\mathrm{D} = 1/St$, is simply obtained from a reciprocal of the Strouhal number. It is $1/St = 8.10$ for B2 that is corresponding to the wind speed of 9.7 m/s and well agree with the A-V curve in Figure 3.8. The reciprocal of *St* for B1 is 6.70, and demands a conversion into the x-axis of Figure 3.8 because the axis normalized by B2's parameters for the purpose of comparison. A conversion value is 8.03 which is also agree with the A-V curve. Thus the difference in the Strouhal numbers causes that the VIV of each single deck begins at the same reduced velocity despite different vertical frequencies.

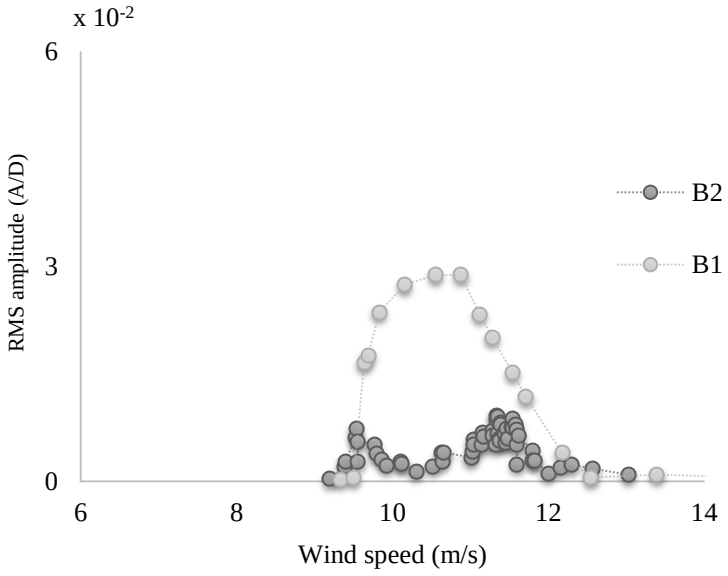

Figure 3.8. A-V curves for each single deck

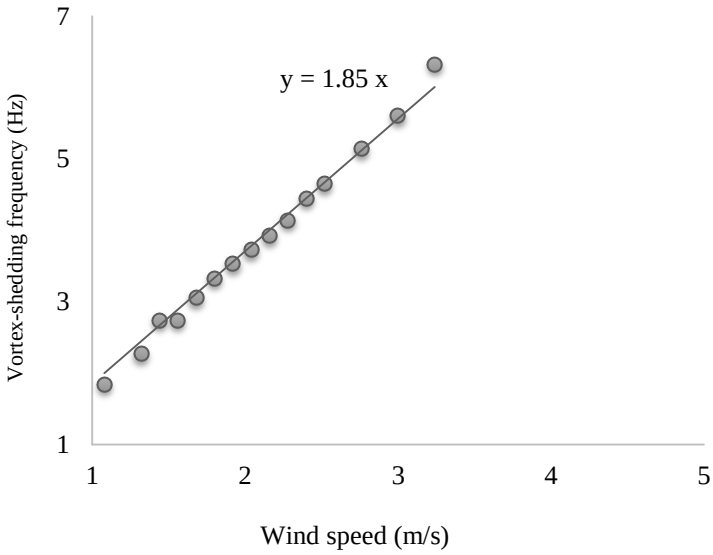

Figure 3.9. Vortex-shedding frequencies of B1

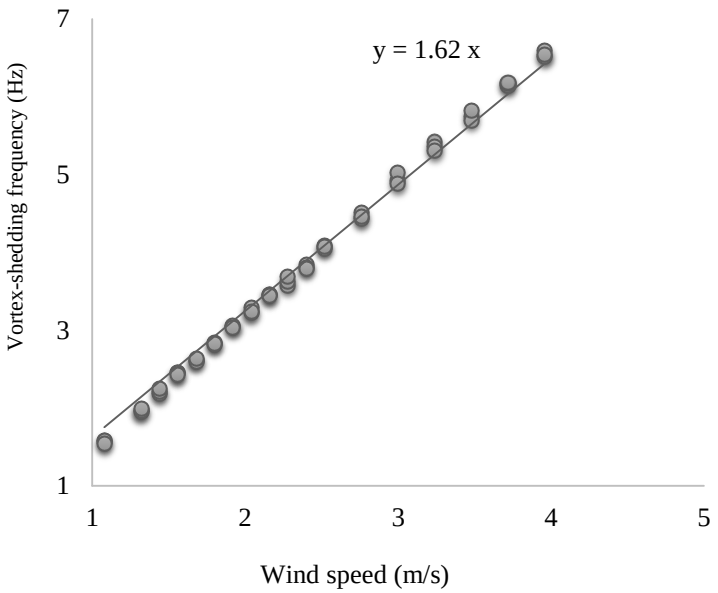

Figure 3.10. Vortex-shedding frequencies of B2

3.2.3 Interactive behavior at tandem arrangement

Figure 3.11 shows A-V curves of both sections in parallel arrangement. Describing NW wind, B2 is placed upstream as is the case of the field observation. Since the vertical frequency of B2 is lower than that of B1, the VIV starts first in B2 at a wind speed of 10.4 m/s. With a further increase in reduced velocity, the VIV move to B1 at a wind speed of 12.2 m/s. The increase of amplitude of VIV due to the parallel disposition is observed in both decks. The RMS single amplitude of B2 reaches up to 0.06 which is 10 times larger than considering the single case and the amplitude of B1 reaches up to 0.10. Although significant VIVs have been reported only for B2 until now, it is interesting that B1 is possibly subjected to an even larger VIV than B2 as long as

the structural damping ratios of two bridges are same.

An interesting point is that the lock-in wind velocity range of B1 remarkably increases comparing Figure 3.8. That of B2 slightly changes also in parallel arrangement. Figure 3.12 shows the shedding frequencies of B2 at the case of parallel arrangement for a NW wind. It is note that the low frequency setup is temporally adopted. The shedding frequency is measured between the two decks and the Strouhal number is 0.109 normalized by the depth of B2. The Strouhal number is changed by the parallel arrangement as the twin box girder and two cylinders. For more information, the Strouhal number for a SE wind, in which B1 is located upstream, is 0.128 normalized by the depth of B1. For purposes of comparison, Figure 3.12 also shows the shedding frequencies while the motion of deck is being released. It clearly shows two lock-in plateaus which demonstrate the VIV of each deck. The lock-in plateau tuned with B2 suddenly jumps to another as increase of wind speed. Although two section model have different the Strouhal number, the lock-in plateau of B1 develops corresponding to the shedding frequency of B2. This indicates that two sections vibrate with the same Strouhal number in parallel arrangement.

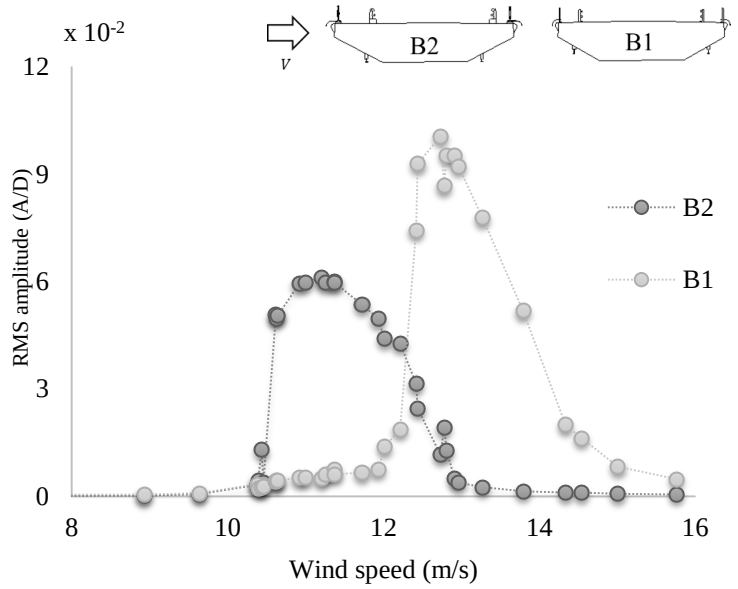

Figure 3.11. A-V curves of as-is parallel arrangement for NW wind

Flows tuned to the deck motion bring an interactive vibration at the lock-in plateau. The time histories of two decks at the wind speed of 11.4 m/s in Figure 3.13 and their spectral densities are drawn in Figure 3.14. While B2 vibrates in a large displacement, B1 also shows a small vibration which is tuned to two frequencies: one for B1 and another for B2. As the spectral density shows almost equal contribution of two frequency components. At the wind speed of 12.2 m/s in Figure 3.11, the amplitude of B2 decreases, while that of B1 increases. Time histories and their spectral density at this reduced velocity are illustrated in Figure 3.15 and Figure 3.16. The spectral density of B1 shows two frequency peaks. The frequency component of B1 increases and B2 decreases. This indicates that the effect of B2 on B1 becomes weaker as long as the

amplitude of B2 decreases. Until this reduced velocity, the time histories of B1 show beat phenomena due to the contribution of two close frequencies. As the wind speed increases to 12.8 m/s in Figure 3.11, the amplitude of B1 prevails with its own natural frequency, while the vibration of B2 becomes weaker, as shown in Figure 3.17. However, the motional frequency of B2 remains unchanged from its natural frequency as shown in Figure 3.18.

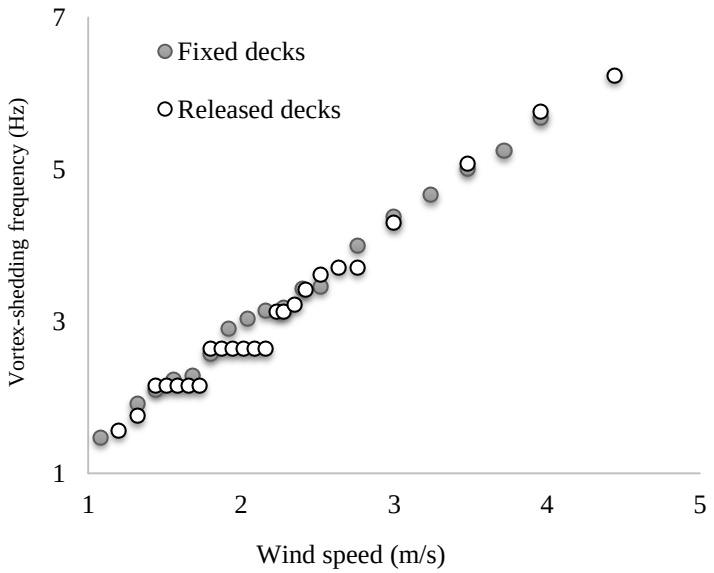

Figure 3.12. Vortex-shedding frequencies while the motion of deck is being restrained or released

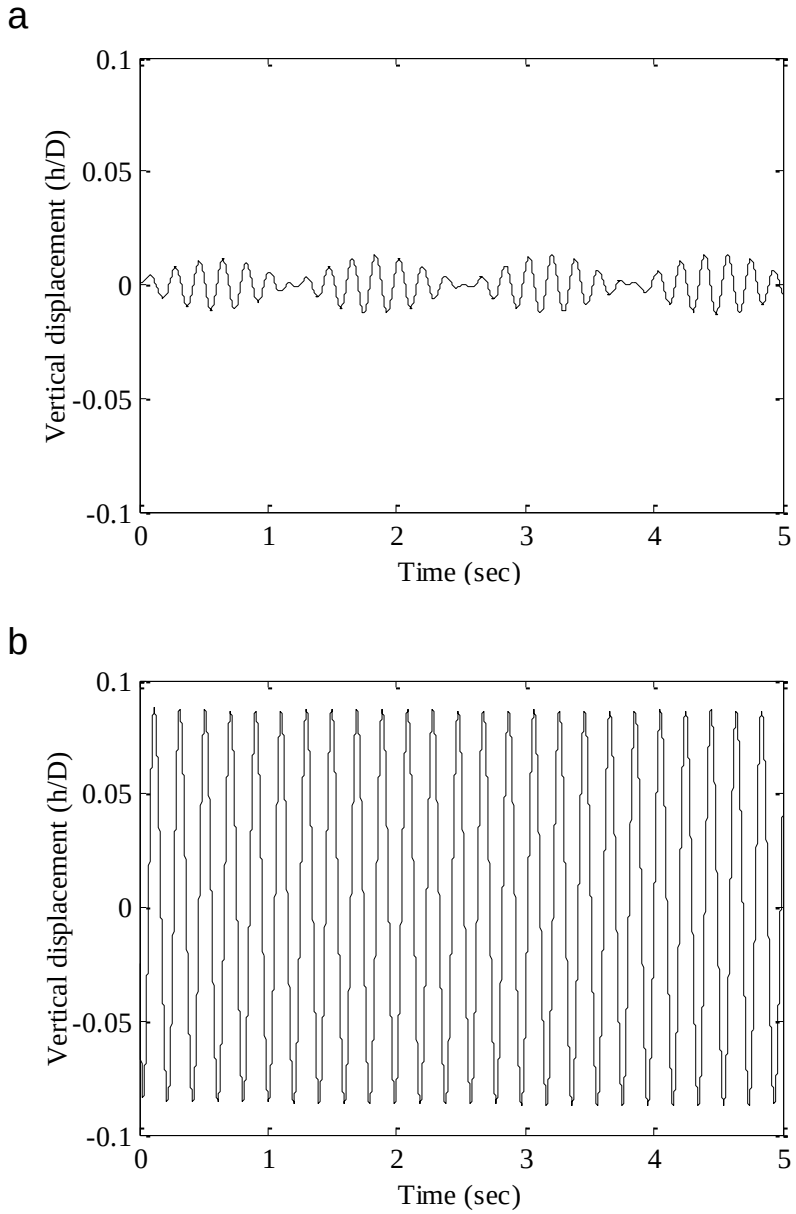

Figure 3.13. Time histories for vertical response of (a) B1 and (b) B2 at V=11.4

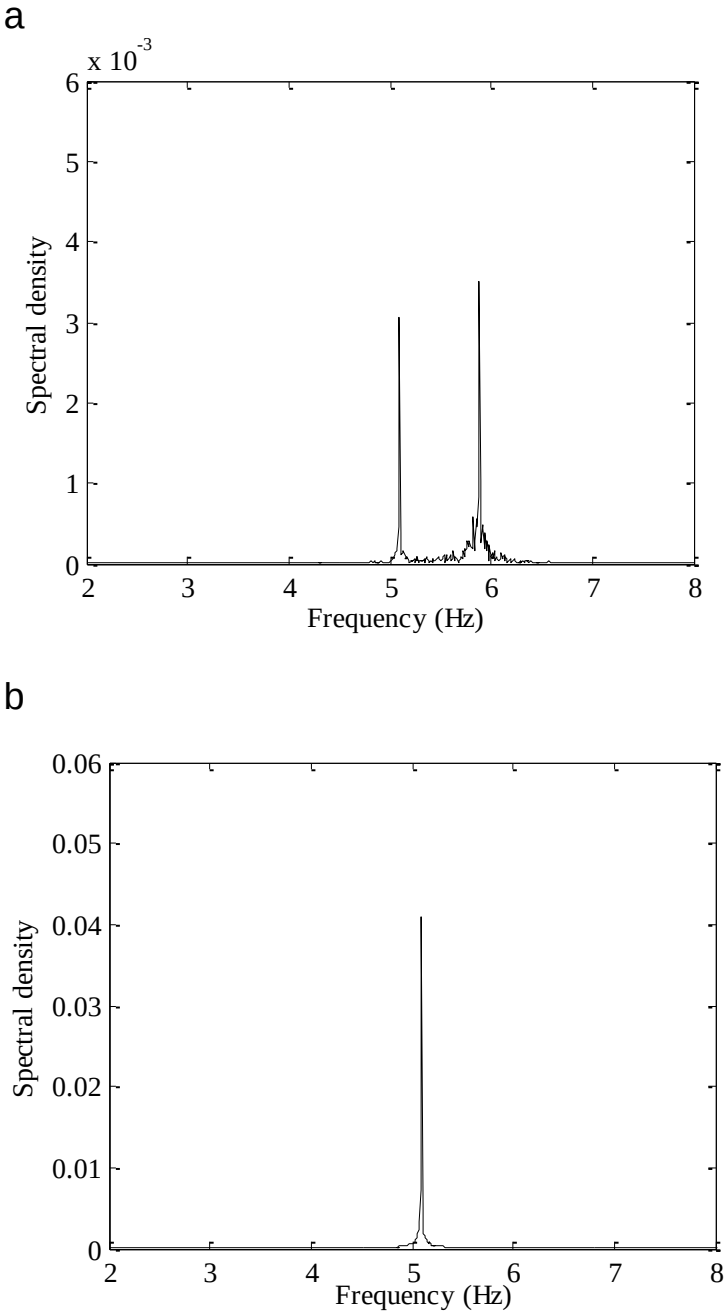

Figure 3.14. Spectral densities for vertical responses of (a) B1 and (b) B2 shown in Figure 3.13

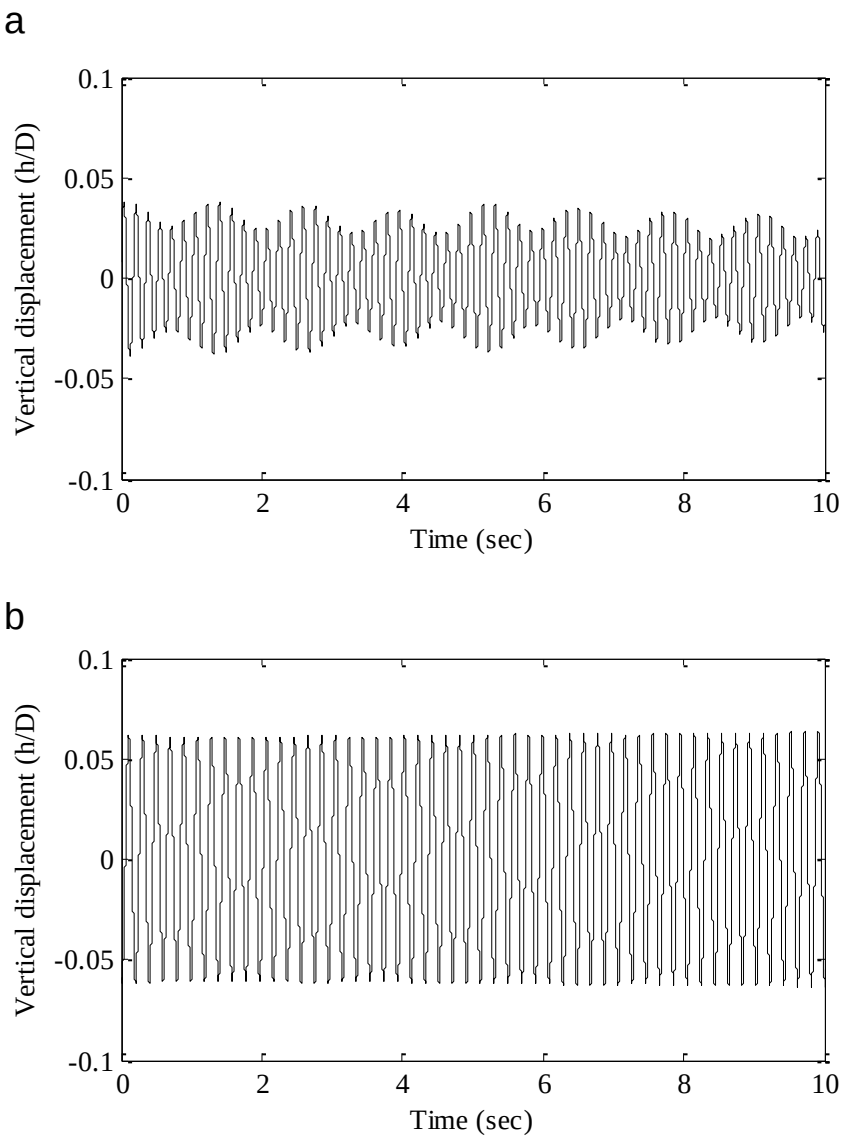

Figure 3.15. Time histories for vertical response of (a) B1 and (b) B2 at V=12.2

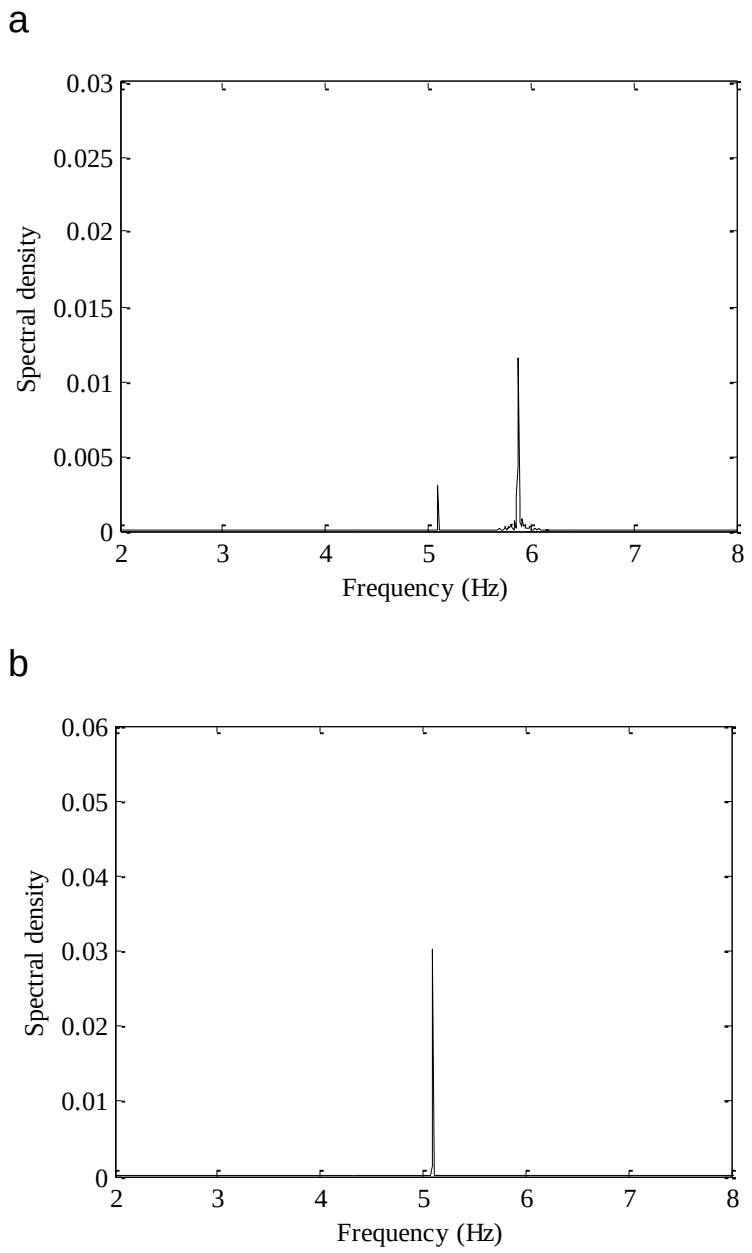

Figure 3.16. Spectral densities for vertical responses of (a) B1 and (b) B2 shown in Figure 3.15

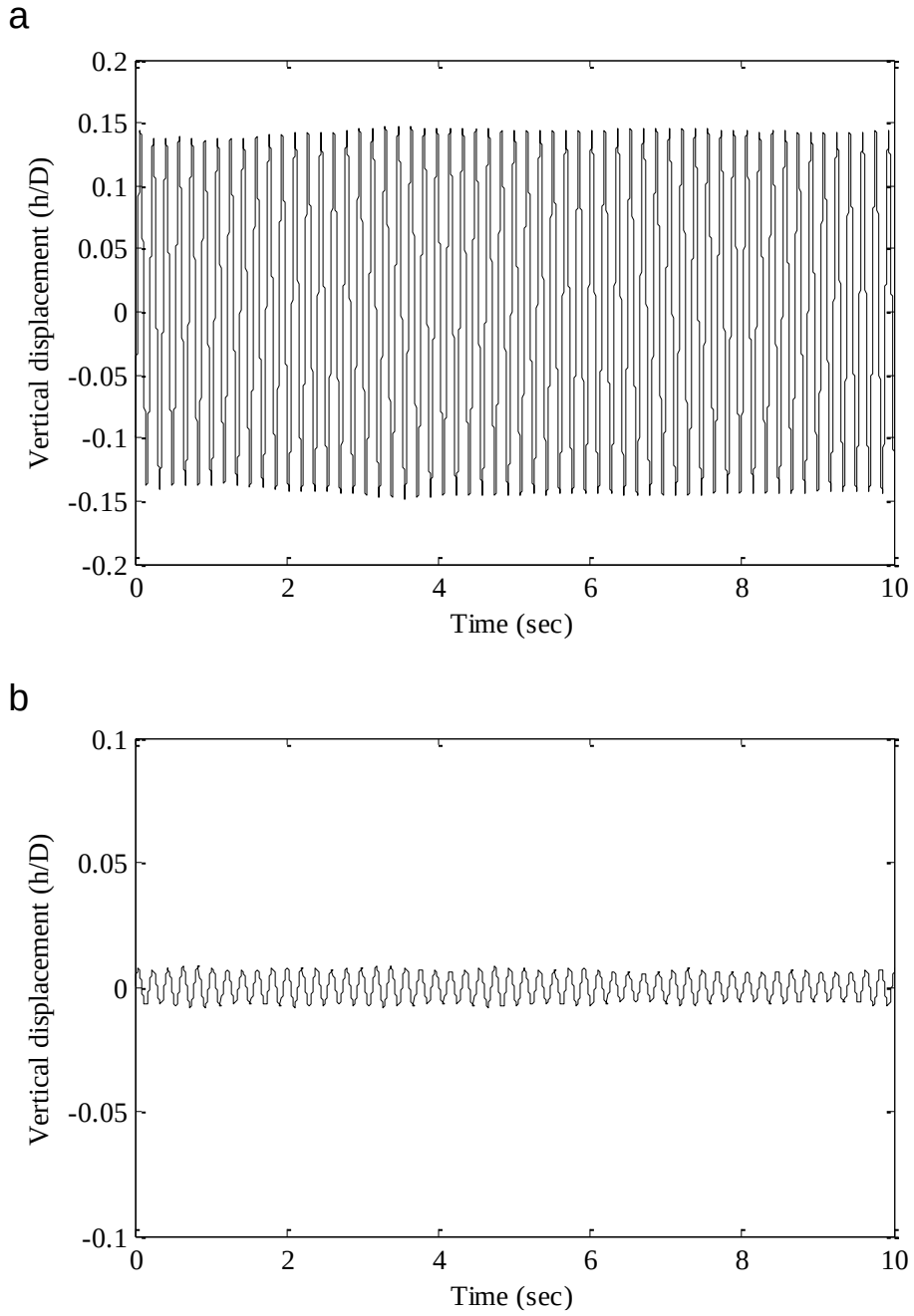

Figure 3.17. Time histories for vertical response of (a) B1 and (b) B2 at V=12.8 when the maximum VIV of B1 occurs

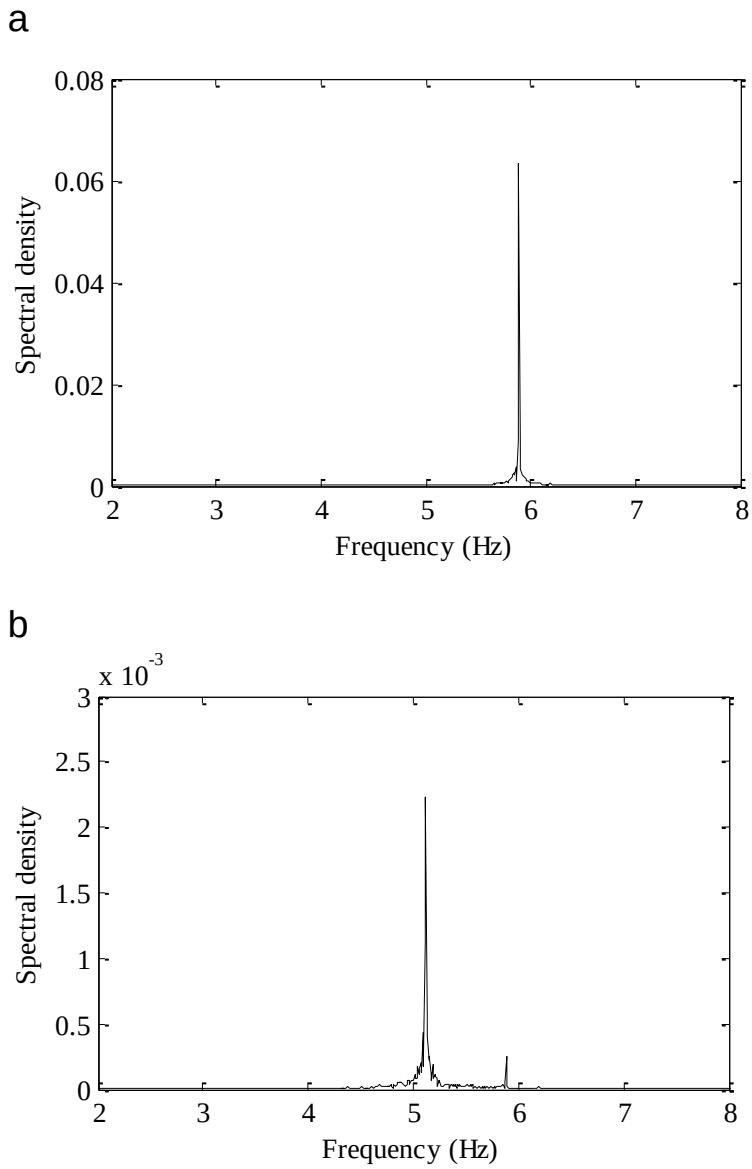

Figure 3.18. Spectral densities for vertical responses of (a) B1 and (b) B2 shown in Figure 3.17

3.2.4 Effect of wind direction

For the case of a SE wind, B1 is placed upstream and B2 is placed downstream. The VIV is initiated in B2 at downstream as long as B2 has lower vertical frequency than that of B1 as shown in Figure 3.19. The VIV of B2 begins at the wind speed of 9.8 m/s which is somewhat lower than considering the NW wind Figure 3.11. The amplitude of vibration increases until the wind speed of 11.3 m/s. At this point, B1 begins to vibrate upstream and, as a result, the VIV of B2 is suddenly reduced. The VIV of B1 is developed upstream up to the wind speed of 12.1 m/s. Comparing results in Figure 3.11 and Figure 3.19, B2 initiates VIV regardless of position because of its lower frequency. Two section models show the larger amplitudes when they are placed at downstream.

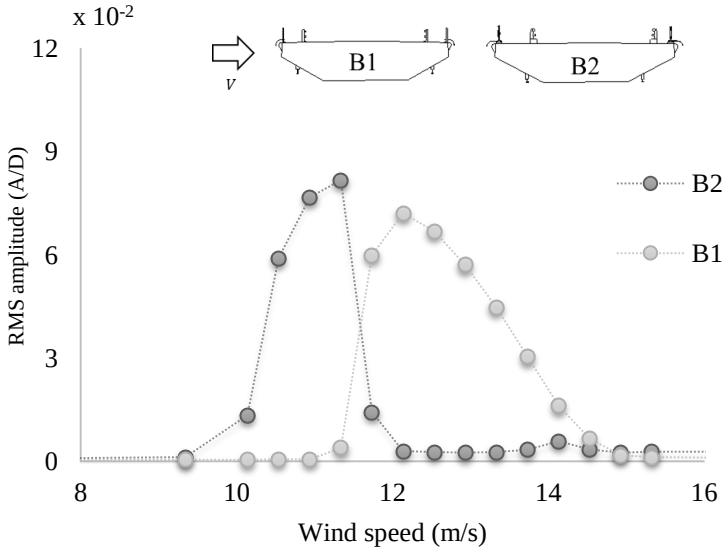

Figure 3.19. A-V curves of as-is parallel arrangement for SE wind

3.2.5 Estimation of the performance of as-is vanes

The A-V curves with the as-is vanes eliminated from B2 are obtained. Figure 3.20 shows the results when B2 is single stand-alone and Figure 3.21 shows the case of the parallel arrangement. Comparing them to the cases equipped as-is vanes, the amplitudes and lock-in wind velocity ranges increase regardless of single or parallel arrangement. The as-is vanes contribute to mitigate the VIV and also shrinkage the lock-in wind velocity range. The as-is vanes are more effective for single bridge considering reduction ratios of the maximum amplitude with vanes to without vanes.

According to the preceding research, the modification of outer configuration of section using aerodynamic additives such as fairings improves the performance for VIV (Meng et al, 2011). Several alternative aerodynamic attachments are investigated whether any possible enhancement in reducing the VIV (see in Figure 3.22). According to the results, the performances of alternatives considered are not better than that when the as-is vanes are used. However, a wider range of possible fairing shapes is not considered in this paper.

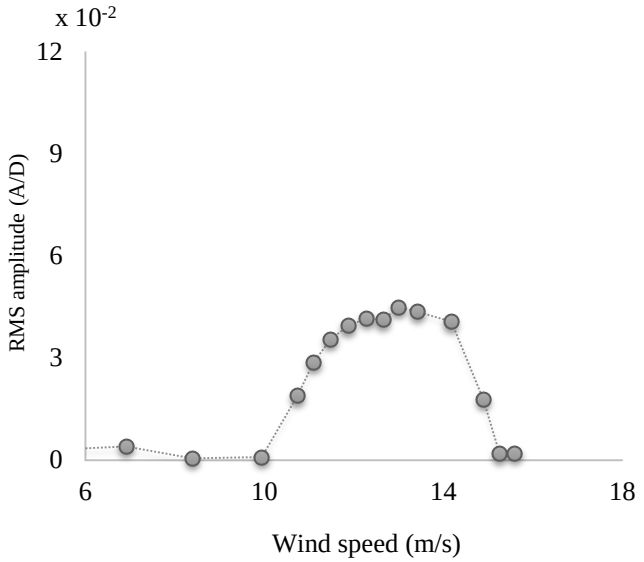

Figure 3.20. A-V curve of B2 without vanes

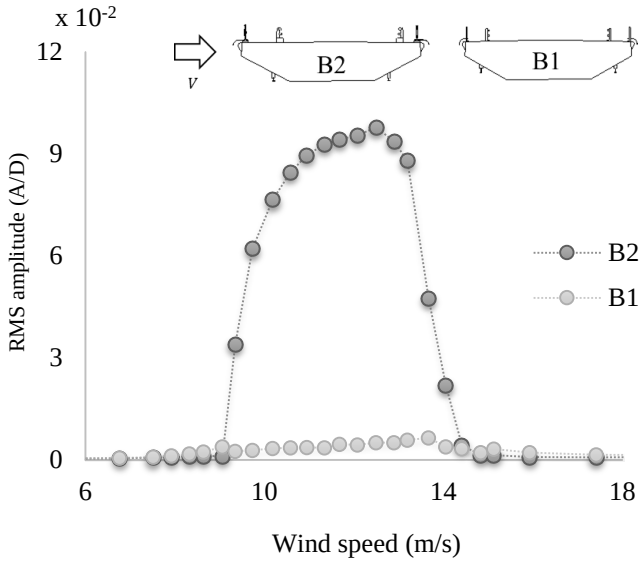

Figure 3.21. A-V curves of as-is parallel arrangement without B2's vanes

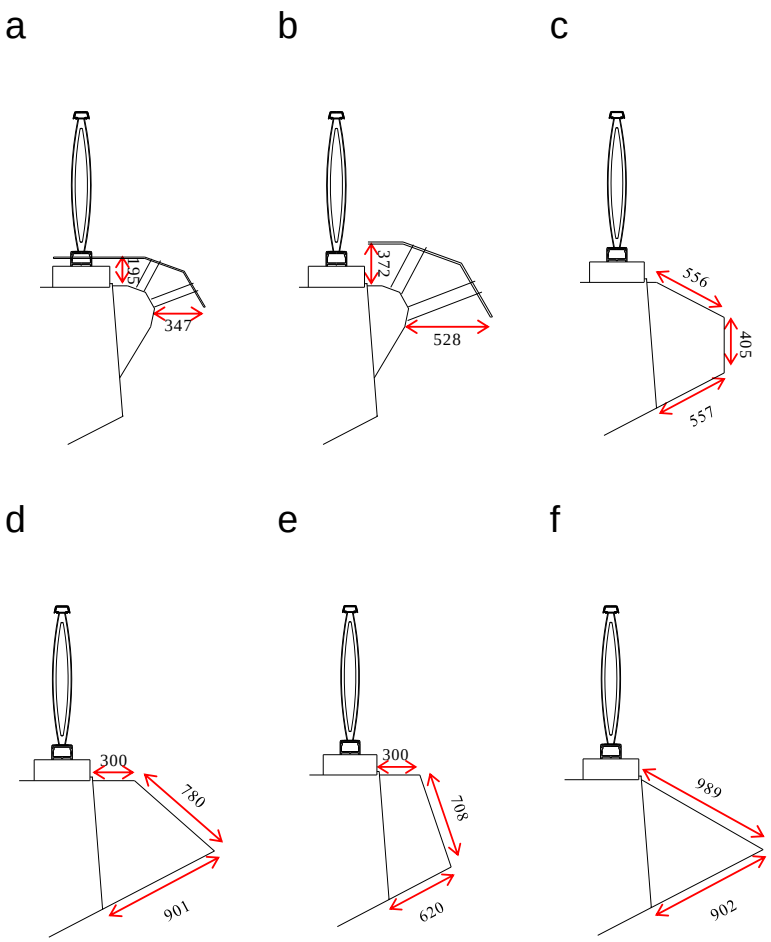

Figure 3.22. As-is vanes and alternative aerodynamic attachments (a) as-is vanes (b) enlarged vanes (c) fairing 1 (d) fairing 2 (e) fairing 3 (f) fairing 4 (unit: mm)

3.2.6 Effects of damping on the interactive VIV and journal publications

Since the structural damping is the critical factor even for the interactive VIV (Honda et al, 1993), the effect of damping on the amplitude of VIV is estimated in the wind tunnel. The damping ratio for the vertical mode is varied from 0.10% to to 0.9% to the critical damping ratio and corresponding change in amplitude is obtained as shown in Figure 3.23. As expected, the interactive VIV decrease rapidly with an increase of damping ratio.

Kim et al (2013) also reported that the damping ratios of the 1st vertical mode of the target bridges are estimated by using the Natural Excitation Technique paired with the Eigensystem Realization Algorithm methods for ambient vibration data. Since the results of this were investigated by another researcher in the author group, the following results of estimated damping ratios are quoted from the paper. The mean of scattered values of the estimated damping ratio is 0.63% for B1 and 0.29% for B2. Especially, the value of B2 is lower than the value of 0.4% recommended for the aerodynamic design of a steel deck cable-stayed bridge with welded connections by the design guideline (Korean Society of Civil EngineersKSCE, 2006). A low-level inherent damping ratio of B2 also potentially contributes to the observation of the interactive VIV in the field.

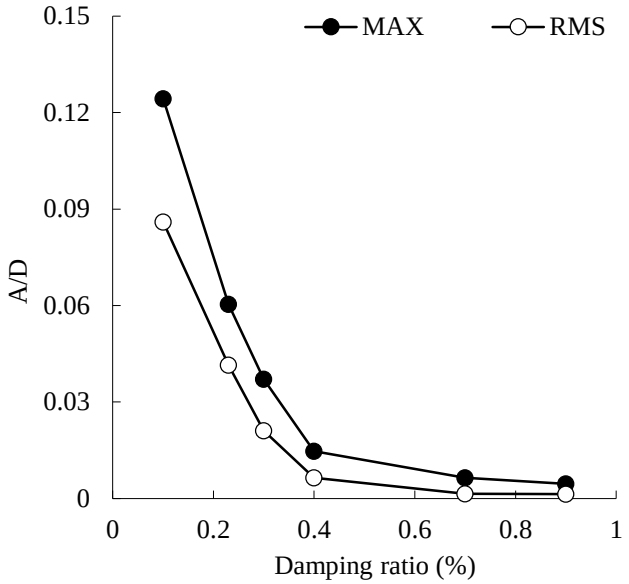

Figure 3.23. Effect of damping on mitigating the interactive VIV

3.3 Flow fields observation in the gap

The PIV tests are managed to figure out the relationship between vibration of B2 and flow field. The trigger generator, synchronized to the position of B2 during the vertical motion, was utilized for the capturing of phase information. The phase (ϕ) is defined as shown in Figure 3.24. The investigated area of flow field is from the leeward edge of B2 to the windward edge of B1 in the case of tandem arrangement. Since the observed area generally exceeded the size of a single frame of camera, an entire flow field between two decks was synthesized with divided frames obtained from different position of camera, by overlapping consecutive frames as shown in Figure 3.25.

Because of limitation of PIV devices, it was necessary to reduce wind speed in which a series of PIV tests was carried out. The frequency scale of $\lambda_f = 11.7$ during vibration tests was temporarily modified to $\lambda_f = 6.8$. The modified frequency information is summarized in Table 3.1.

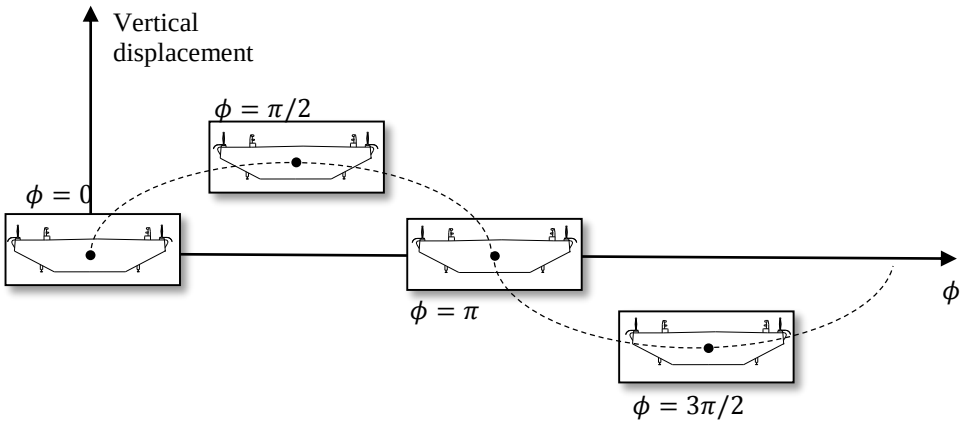

Figure 3.24. Phases (ϕ) of heaving motion

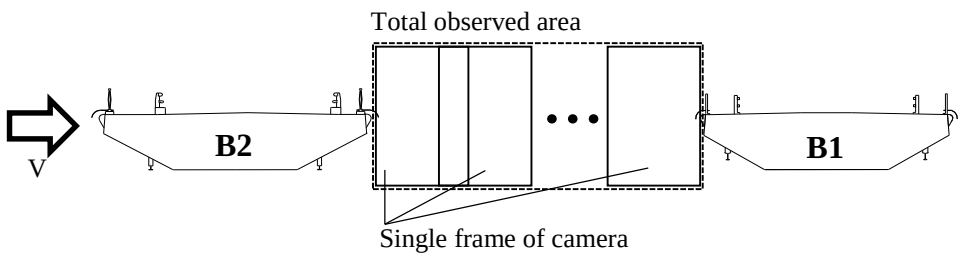

Figure 3.25. PIV observation area

Table 3.1. Frequency setup for PIV tests

Parameters	Similarity scale	B1		B2	
		Prototype	Model	Prototype	Model
Vertical frequency (Hz)	λ_f =6.8	0.513	3.491	0.436	2.960
Torsional frequency (Hz)	λ_f =6.8	1.490	10.03	1.834	12.66

3.3.1 Time-frequency analysis of velocity field

Wavelet transform decomposes the signal into a series of basis functions of finite length which is called a parent wavelet, ψ. The wavelet transform compares the signal to shifted and compressed or stretched version of a parent wavelet. Compressing and stretching a function is referred to as scaling. Using wavelet transform, then, the signal is decomposed into wavelets of different scales at various positions in time or space. The form of the wavelet transform for the signal, $g(t)$, is

$$a(i,j) = \int_{-\infty}^{\infty} g(t)\psi(i,j,t)dt \tag{3.2}$$

where *i* is a scale parameter and *j* is position parameter. Note that this form is referred to the continuous wavelet transform distinguished from the discrete wavelet transform. In this study, the continuous wavelet transform is adopted to improve frequency resolution. There are many different admissible wavelets that can be used. The analytic Morlet wavelet provided by Matlab is used in this study and is defined in the Fourier domain by:

$$\psi(\omega) = \pi^{-\frac{1}{4}} e^{-\frac{(\omega-6)^2}{2}} H(\omega) \tag{3.3}$$

where $H(\omega)$ is the Heaviside step function.

The wavelet coefficients are well proper for analyzing time-variant events. The coefficients describe the energy at the corresponding frequency band, and the coefficients in a particular band mean the energy at time intervals. When the squared coefficients on time-axis, the transfer of energy can be analyzed along the time scale. Flow fields obtained from PIV tests are consist of a pair of vertical and horizontal velocity components at various positions. The wavelet transform is applied at different positions within observed area by PIV. Since the results are similar at the same case, the only representative results are introduced here. Positions of analysis points are marked in Figure 3.26.

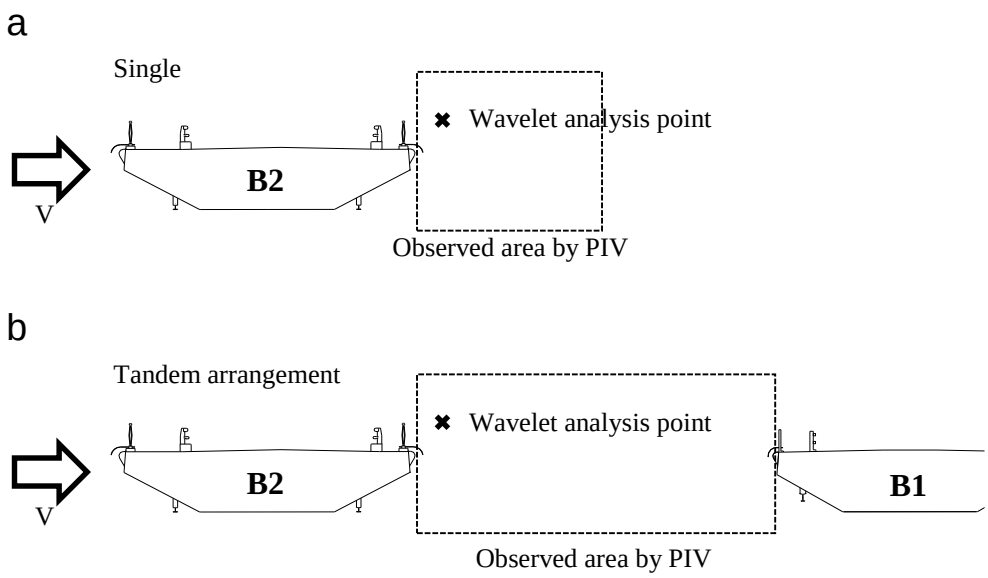

Figure 3.26. Position of wavelet analysis at (a) single B2 and (b) tandem arrangement

Analysis results of the horizontal velocity of flow at single B2 or tandem arrangement are illustrated in Figure 3.27 and Figure 3.28, respectively. Figures show the squared value of wavelet coefficient on the time-frequency domain. Both cases shows that the energy is concentrated around the frequency component of 3 Hz. When B2 placed alone, the dominant frequency band changes in time within a range of 2 to 4 Hz. The magnitude of coefficient also keeps changing, then the frequency component of 3 Hz sometimes disappears. When two sections placed in tandem, a strong stationary result is obtained. The energy is very concentrated in a narrow frequency band of 3 Hz. This implies that a strong motion-induced flow structure is formed while B1 is placed downstream of B2.

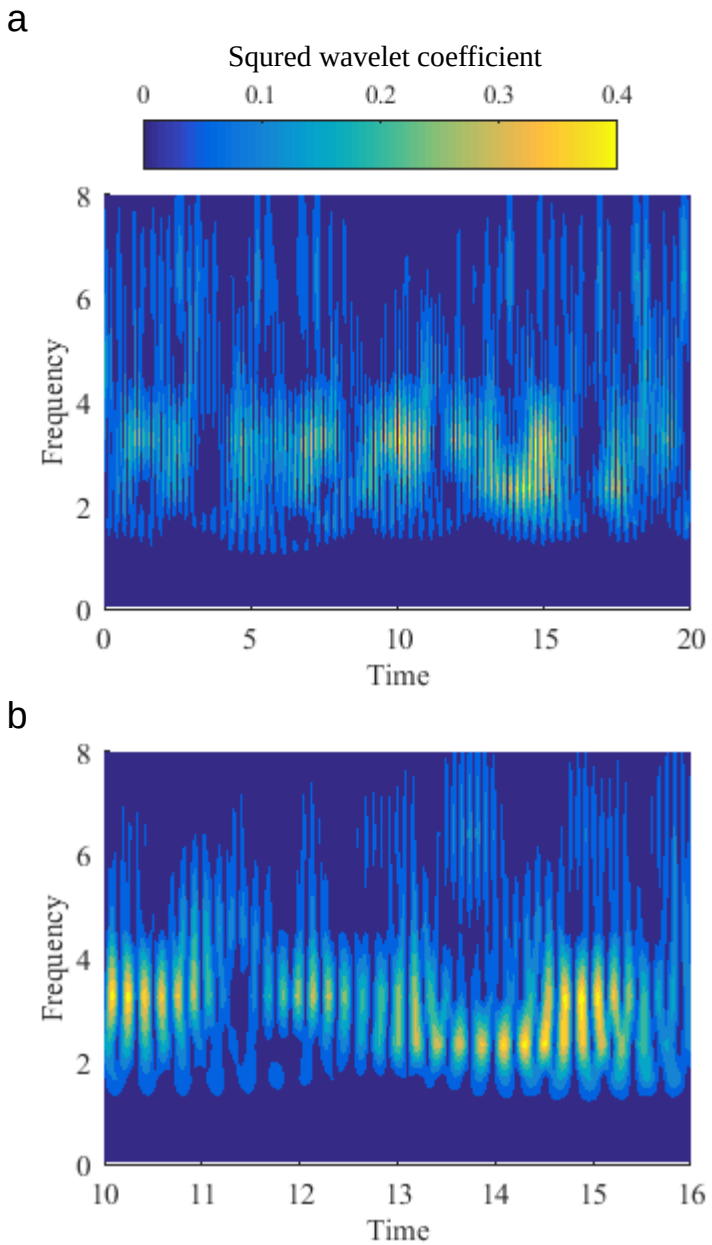

Figure 3.27. (a) Time-frequency analysis of flow at single B2 and (b) zoomed-in at the time range

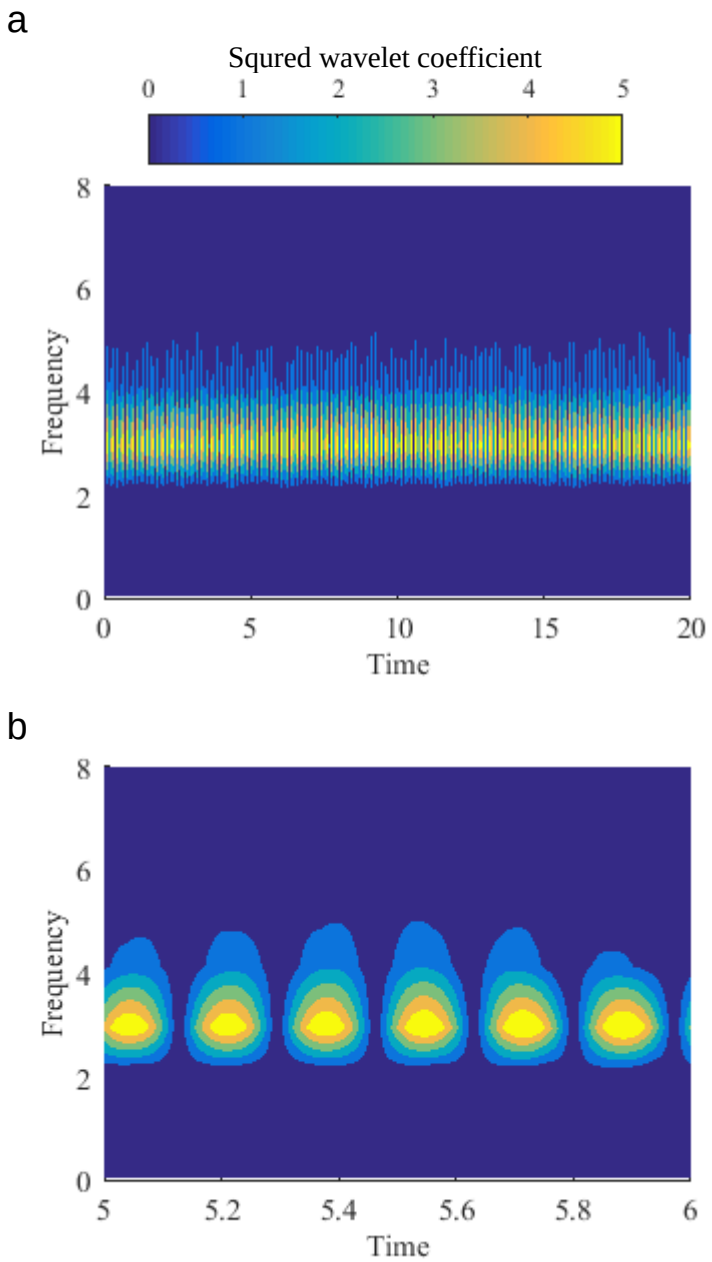

Figure 3.28. (a) Time-frequency analysis of flow at tandem arrangement and (b) zoomed-in at the time range

3.3.2 Motion induced flow fields

From the wavelet analysis, it is confirmed that the motion induced flow dominates the area behind B2, particularly in tandem arrangement. The phase average method is well suited for analyzing frequency oriented data (Hussain and Reynolds, 1970). The averaging is carried out for a particular phase within a range of ± 2 degrees. The wind velocity was set to 11.5m/s at which B2 showed a large amplitude in tandem arrangement. For the case of single B2, the wind velocity was set to 12.2m/s which showed also a large amplitude for the VIV.

Figure 3.29 shows the change in flow patterns for the consecutive increments in phase for an entire period of oscillation. The upper side figures show the case of the single B2 while the lower side figures illustrate the case of tandem arrangement. The velocity contours show that the wind speeds behind Bridge 2 in both cases are relatively low.

The variation in flow field for the case of parallel disposition is discussed first. At $\phi = \pi/2$, B2 is located at the top position (Figure 3.29 (c)), the flow makes a "Ω" shape in which the wind flow enters from the bottom side and moves upward, resulting in an upward force on B2. However, the flow turns down and passes under B1. As B2 moves back to the neutral position of $\phi = \pi$, a counterclockwise eddy is initiated behind B2 (Figure 3.29 (d) and (e)). This eddy travels down to B1 making a "Ʊ" shape

streamline and the overall flow pattern changes to a downward direction behind B2. However, the flow turns up and passes over B1 (Figure 3.29 (f) and (g)). As B2 moves back to the neutral position again ($\phi = 0$) after reaching the bottom point ($\phi = 3\pi/2$), the clockwise eddy is initiated (Figure 3.29 (h) and (a)). This eddy travels down to B1 making a "Ω" shaped flow field (Figure 3.29 (b)). Consequently, the consecutive PIV images for the case of the parallel disposition shows a clear change of flow pattern between the "Ω" and "ʊ" shapes alternating the streamlines upward and downward behind B2.

The PIV images for the case of single B2 are also shown in Figure 3.29 for the same phase angle even though the amplitude is smaller than that of comparative tandem arrangement. The weak vortices are also observed for the single B2 as shown in Figure 3.29 (b) and (d). However, the flow patterns are quite different from those for tandem arrangement. Some of shear flows separated from B2 rolls up behind B2, then forms vortices in both upper and lower sides of deck. Furthermore, the change of streamlines corresponding to the phase is not obvious.

The comparative investigation of PIV images demonstrates that the existence of downstream deck changes wake structures and flow patterns, then the alternating "Ω" and "ʊ" shaped flow fields appear at tandem arrangement. Consequently, the wind velocity of the streams between two consecutive eddies is in the range of 5 to 6 m/s

while the wind velocity behind B2 is less than 2 m/s for all of the phases at single B2 alone. The low-speed area develops freely downstream without any hindrance by B1.

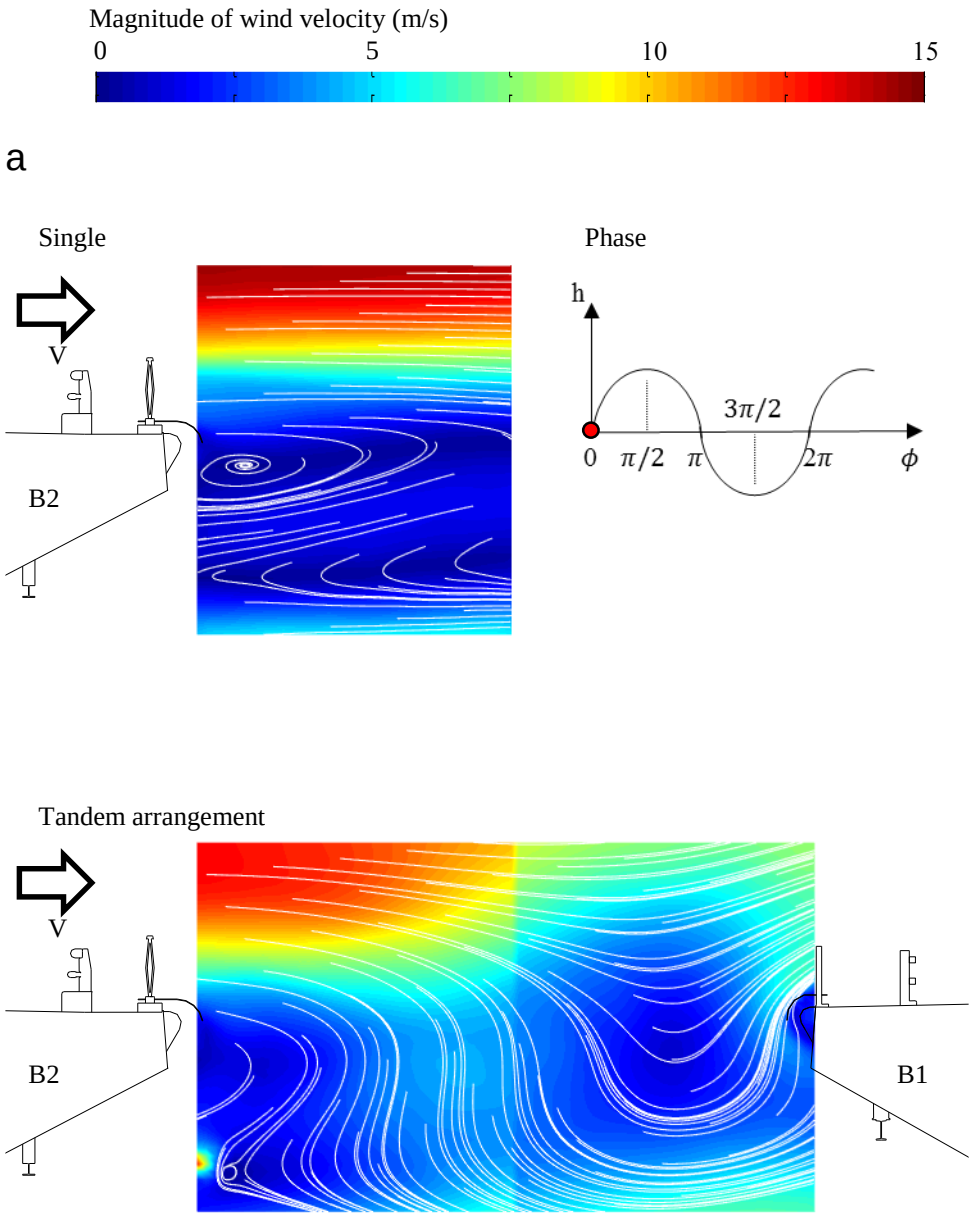

Figure 3.29. Wind velocity field and streamlines during one period of vertical motion in B2 at $\phi =$ (a) 0, (b) $\pi/4$, (c) $\pi/2$, (d) $3\pi/4$, (e) π, (f) $5\pi/4$, (g) $3\pi/2$ and (h) $7\pi/4$

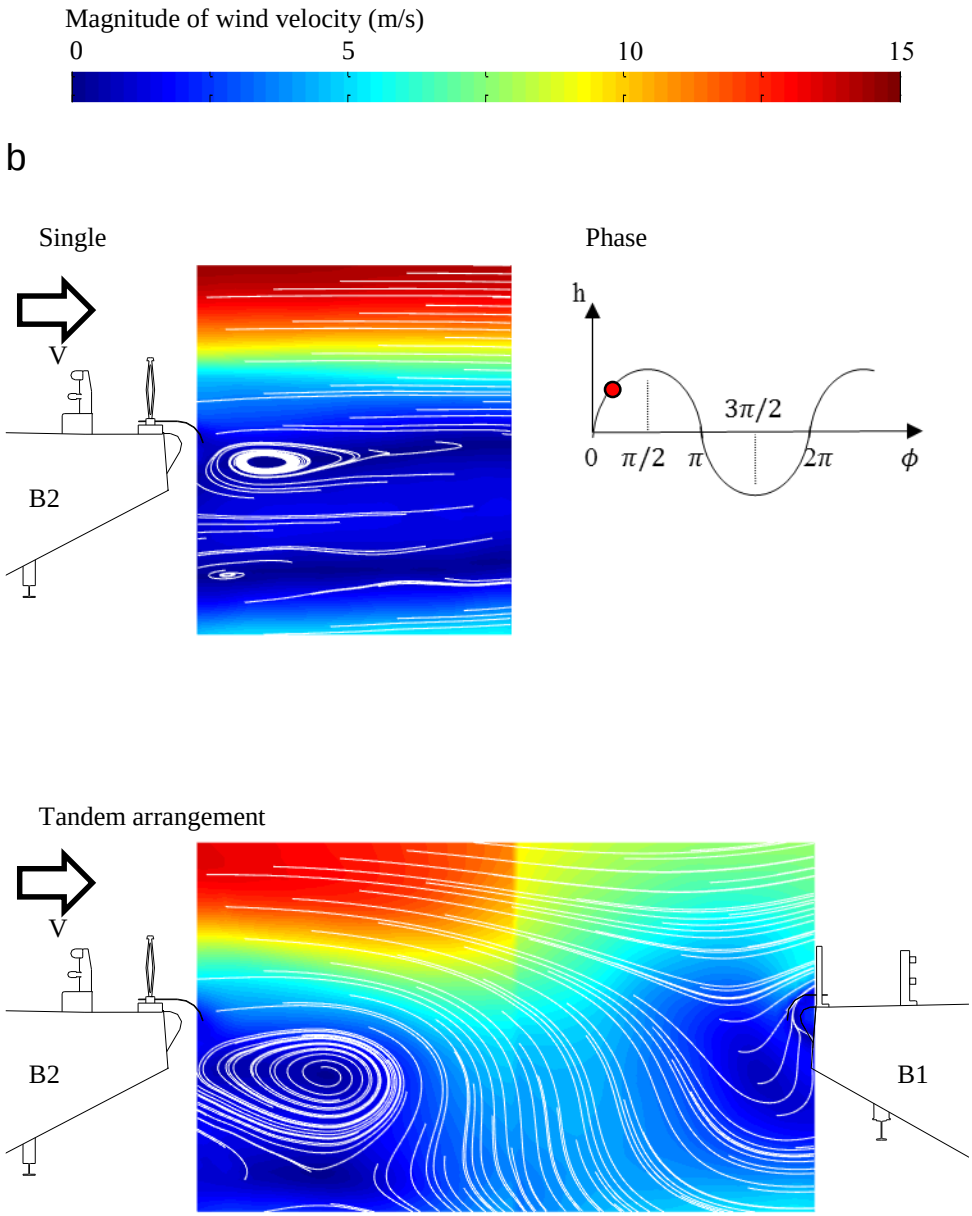

Figure 3.29. Continued.

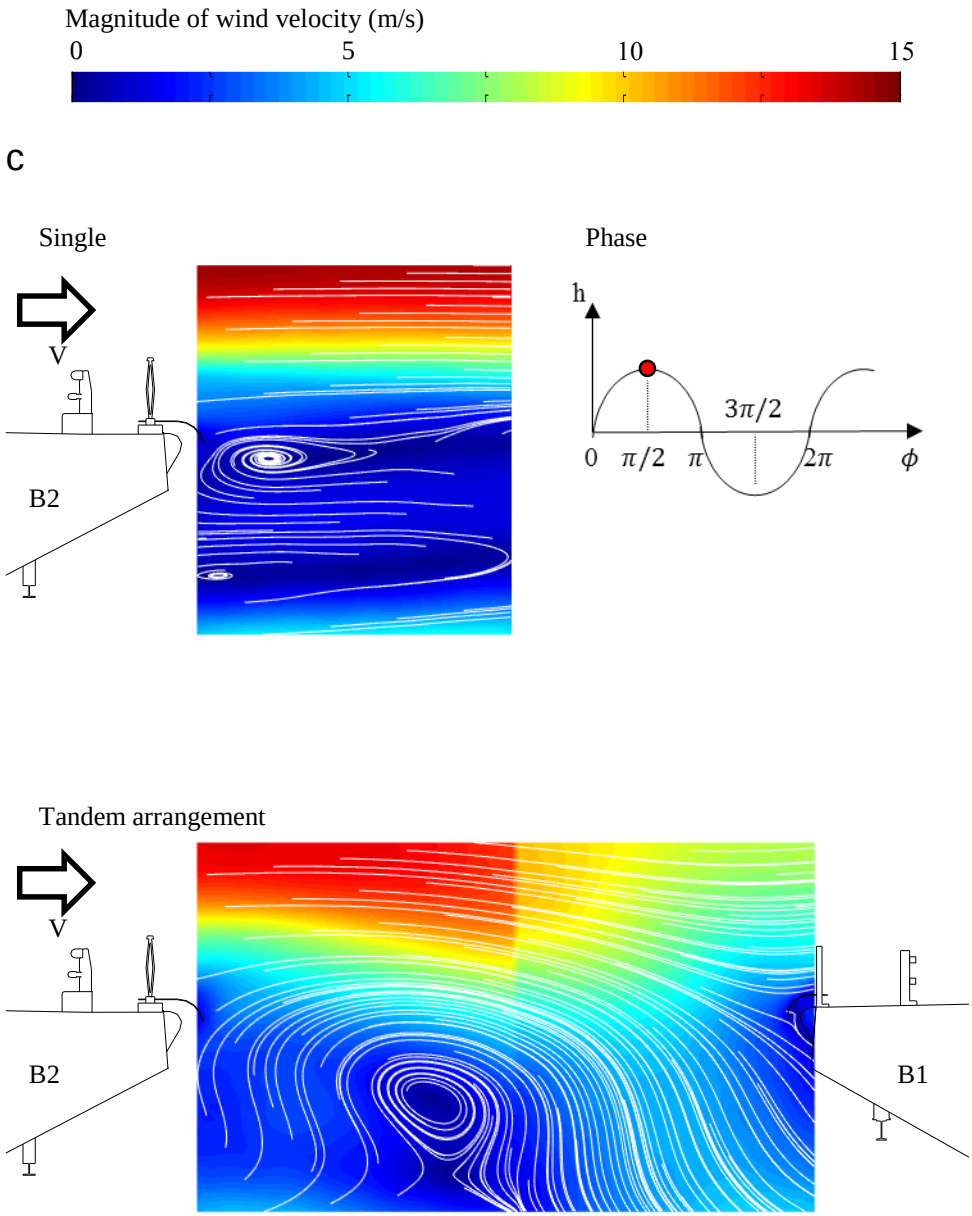

Figure 3.29. Continued.

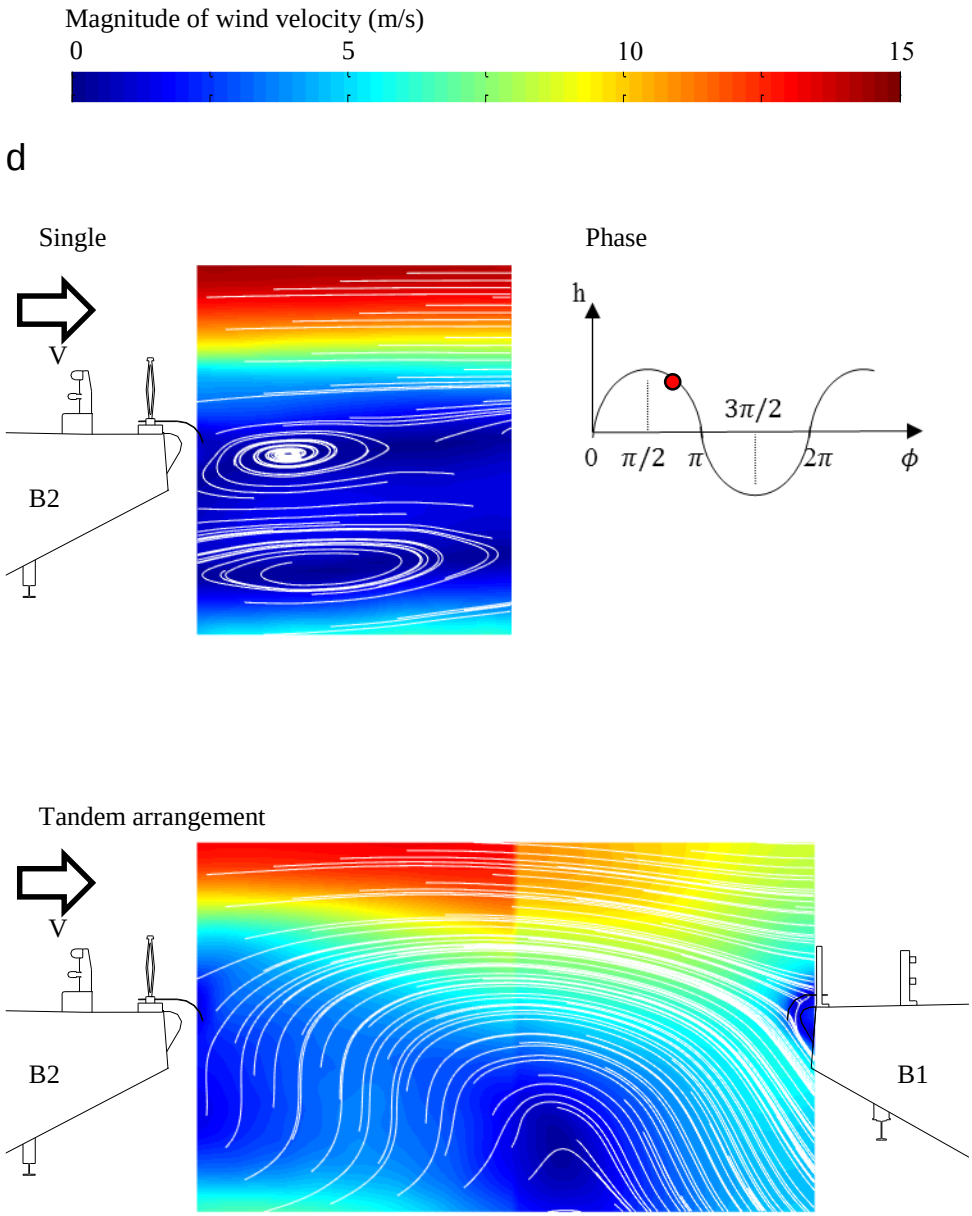

Figure 3.29. Continued.

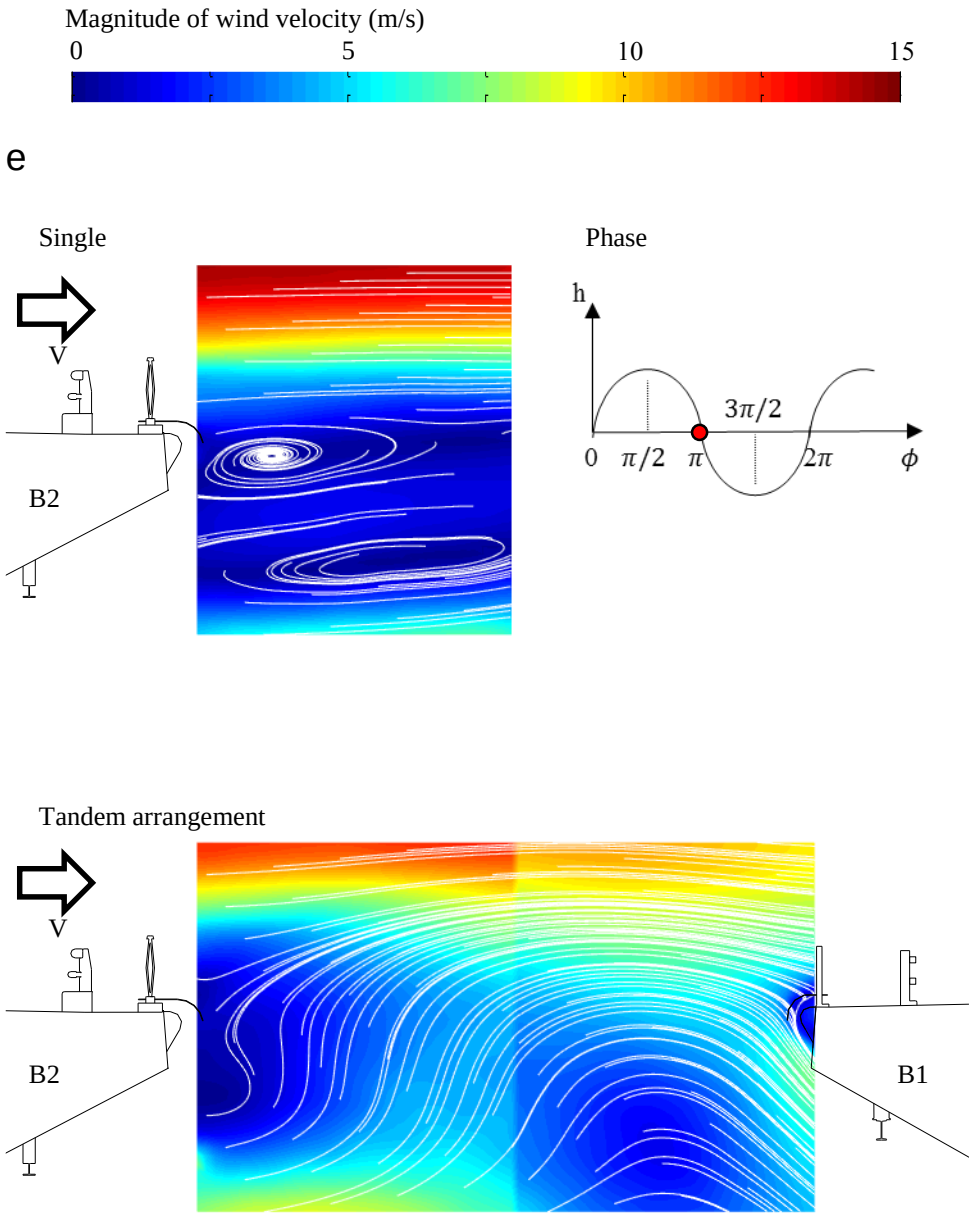

Figure 3.29. Continued.

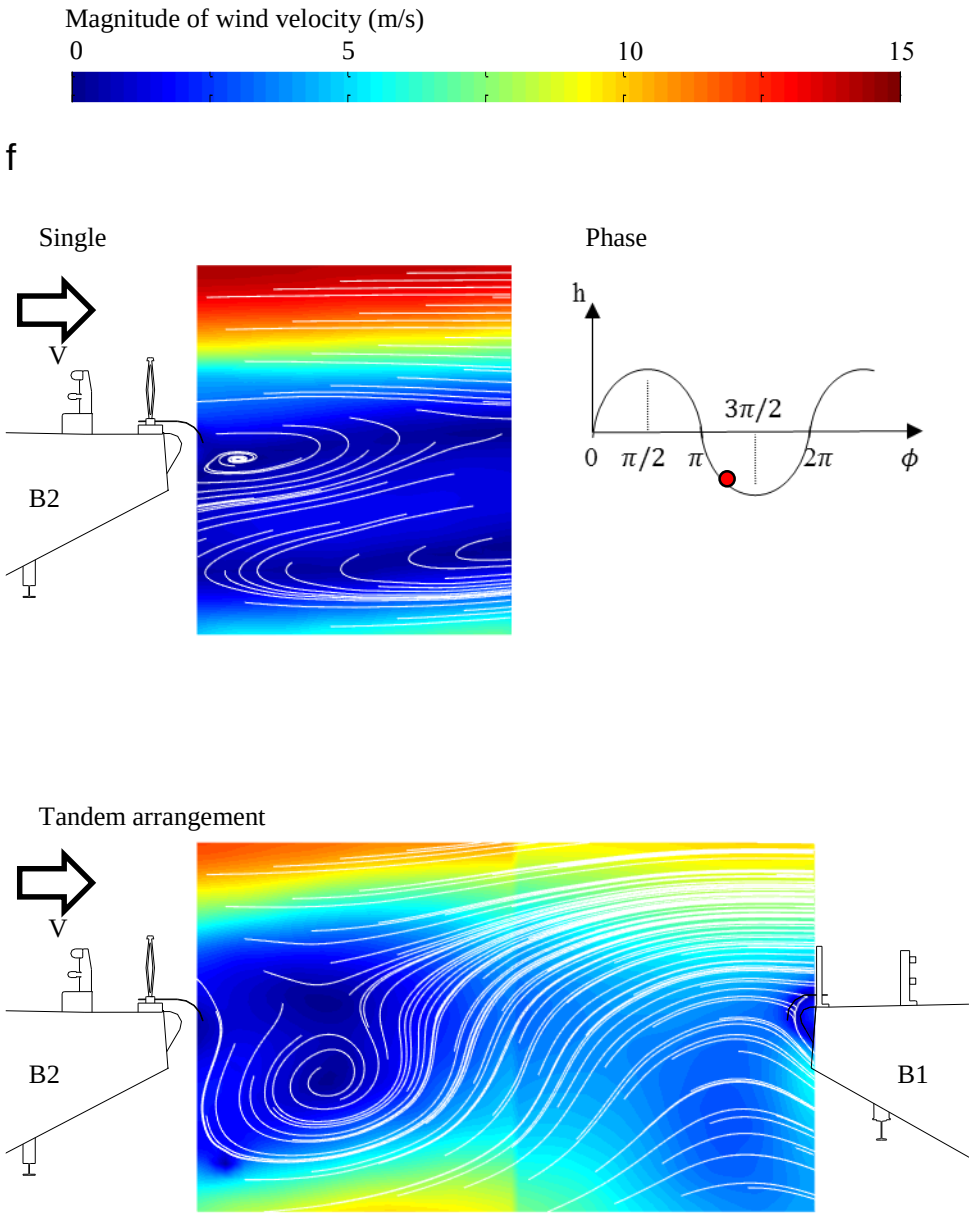

Figure 3.29. Continued.

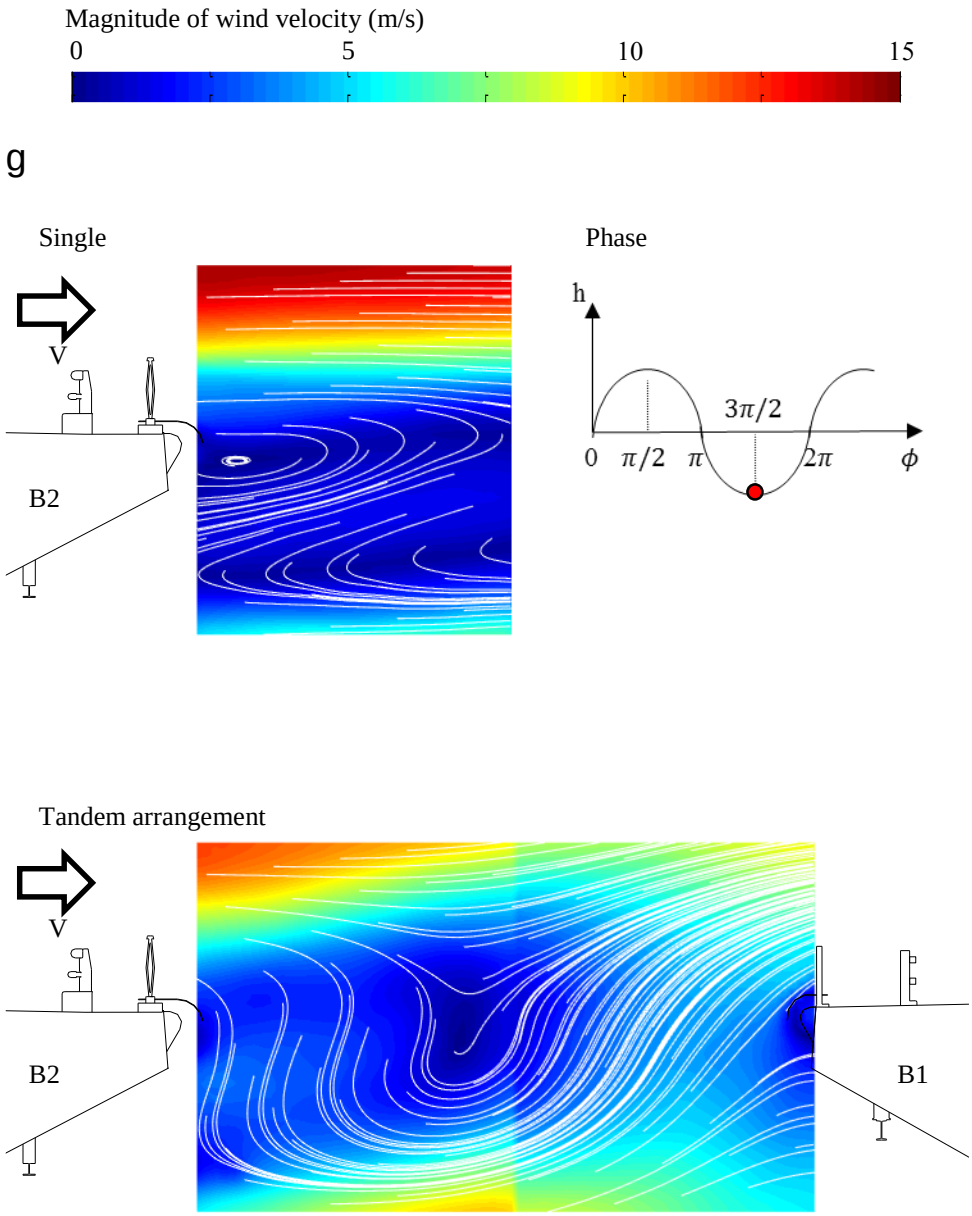

Figure 3.29. Continued.

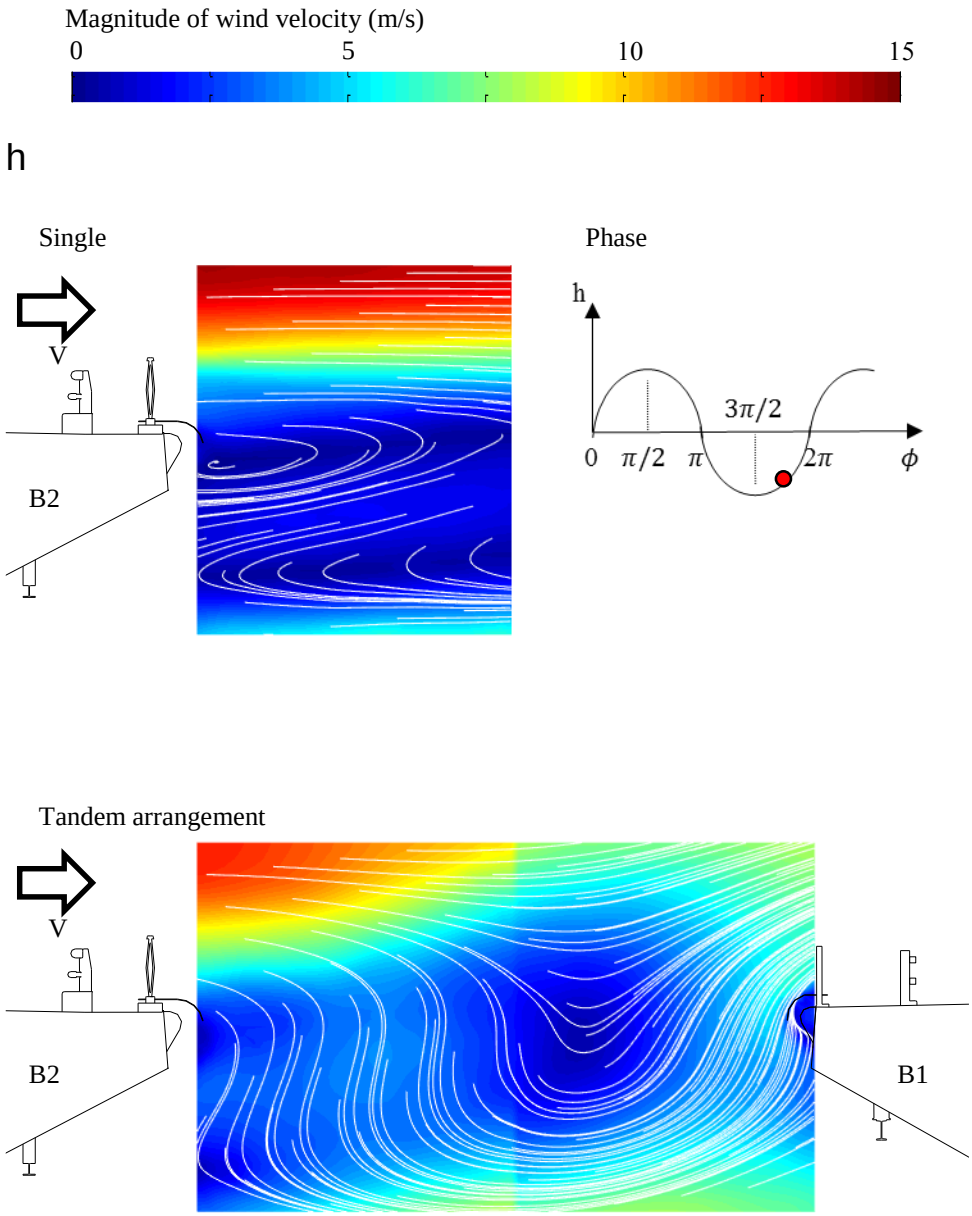

Figure 3.29. Continued.

3.3.3 Vortex identification by swirling strength method

The swirling strength method (Zhou et al, 1999) is utilized for vortex identification. The swirling strength method is based on the decomposition of velocity gradient tensor, $\boldsymbol{D}$, in Cartesian coordinate (x, y, z). The velocity gradient tensor is written as,

$$\boldsymbol{D} = \begin{bmatrix} \frac{\partial u}{\partial x} & \frac{\partial u}{\partial y} & \frac{\partial u}{\partial z} \\ \frac{\partial v}{\partial x} & \frac{\partial v}{\partial y} & \frac{\partial v}{\partial z} \\ \frac{\partial w}{\partial x} & \frac{\partial w}{\partial y} & \frac{\partial w}{\partial z} \end{bmatrix} \tag{3.4}$$

where, u, v, and w are the velocity component of flow particle along x, y and z directions, respectively. Then, $\boldsymbol{D}$ can be decomposed as,

$$\boldsymbol{D} = [\boldsymbol{v_r} \quad \boldsymbol{v_{cr}} \quad \boldsymbol{v_{ci}}] \begin{bmatrix} \boldsymbol{\lambda_r} & & \\ & \boldsymbol{\lambda_{cr}} & \boldsymbol{\lambda_{ci}} \\ & -\boldsymbol{\lambda_{ci}} & \boldsymbol{\lambda_{cr}} \end{bmatrix} [\boldsymbol{v_r} \quad \boldsymbol{v_{cr}} \quad \boldsymbol{v_{ci}}]^{-1} \tag{3.5}$$

where λ_r and $\lambda_{cr} \pm \lambda_{ci} i$ ($i = \sqrt{-1}$) are the real and the conjugate pair of the complex eigenvalues for the corresponding eigenvectors, $\boldsymbol{v_r}$ and $\boldsymbol{v_{cr}} \pm \boldsymbol{v_{ci}}$, respectively. The three vectors $[\boldsymbol{v_r} \quad \boldsymbol{v_{cr}} \quad \boldsymbol{v_{ci}}]$ defines a local coordinate (y_1, y_2, y_3) system. The local streamlines can be expressed as

$$y_1(t) = C_r exp\lambda_r t$$

$$y_2(t) = exp\,\lambda_{cr} t\,[C_c^1\,cos(\lambda_{ci} t) + C_c^2\,sin(\lambda_{ci} t)] \tag{3.6}$$

$$y_3(t) = exp\,\lambda_{cr} t\,[C_c^2\,cos(\lambda_{ci} t) - C_c^1\,sin(\lambda_{ci} t)]$$

where C_r, C_c^1 and C_c^2 are constant for the initial vales at $t = 0$. The strength of the local swirling motion is quantified by the imaginary part of the complex eigenvalue, λ_{ci}. Since the PIV test in this study identifies only two-dimensional flows, the velocity gradient tensor can also be represented in two-dimensional form. The determinant for two-dimensional form of the velocity gradient tensor gives two real eigenvalues or a conjugated pair of complex eigenvalues, $\lambda_{cr} \pm \lambda_{ci} i$, then λ_{ci} is used as the swirling strength. By definition, since the magnitude of the swirling strength corresponds to angular frequency of rotational motion of fluid, it can be used as an index of vortex strength. It is always larger than zero. For distinguishing rotational direction of vortex, the definition of the vorticity at the same position is utilized. The vorticity for a two-dimensional incompressible flow is defined as

$$\omega_{2D} = \frac{\partial v}{\partial x} - \frac{\partial u}{\partial y} \tag{3.7}$$

Figure 3.30 shows the vortex strength fields for the consecutive increments in phase for an entire period of oscillation. The figure compares the results at the case of the single B2 and of tandem arrangement. The counterclockwise rotation of vortex is represented as positive as mentioned above. As long as the shear flows from B2 roll up into the gap and form the vortex behind the section, the vortex from upper side has clockwise rotation (negative direction) and from lower side has counterclockwise rotation (positive direction).

The vortex strength fields for the case of single B2 show that relatively small size of vortices are developed and strength of them are weaker than that of comparative tandem arrangement. Any motion induced feature such as a change corresponding to the phase angles does not appear.

The vortex strength fields for the case of parallel disposition are strongly related with the motion of B2. At $\phi = \pi/2$, B2 is located at the top position (Figure 3.30 (c)), the vortex from upper side of the deck (in negative direction) is placed at the middle of the gap. At both end of lower side of the gap, two positive directional vortices exist. The left-hand side one newly begins to roll up at the bottom of B2 while the right-hand side one formed one period ago escapes the gap. As B2 moves back to the neutral position of $\phi = \pi$, a counterclockwise vortex is formed from lower side of the deck (Figure 3.30 (d) and (e)) and travels down to B1 until B2 reaches the bottom position (Figure 3.30 (f) and (g)). At $\phi = 3\pi/2$, the vortex from lower side of the deck (in

positive direction) travels to the middle of the gap. As B2 moves back to the neutral position again ($\phi = 0$) after reaching the bottom point ($\phi = 3\pi/2$), the clockwise vortex is initiated (Figure 3.30 (g) and (h)). Consequently, at the case of tandem arrangement, the motion-induced vortices are alternately generated from upper and bottom side of B2, then those vortices travel down and escape the gap during one period of motion.

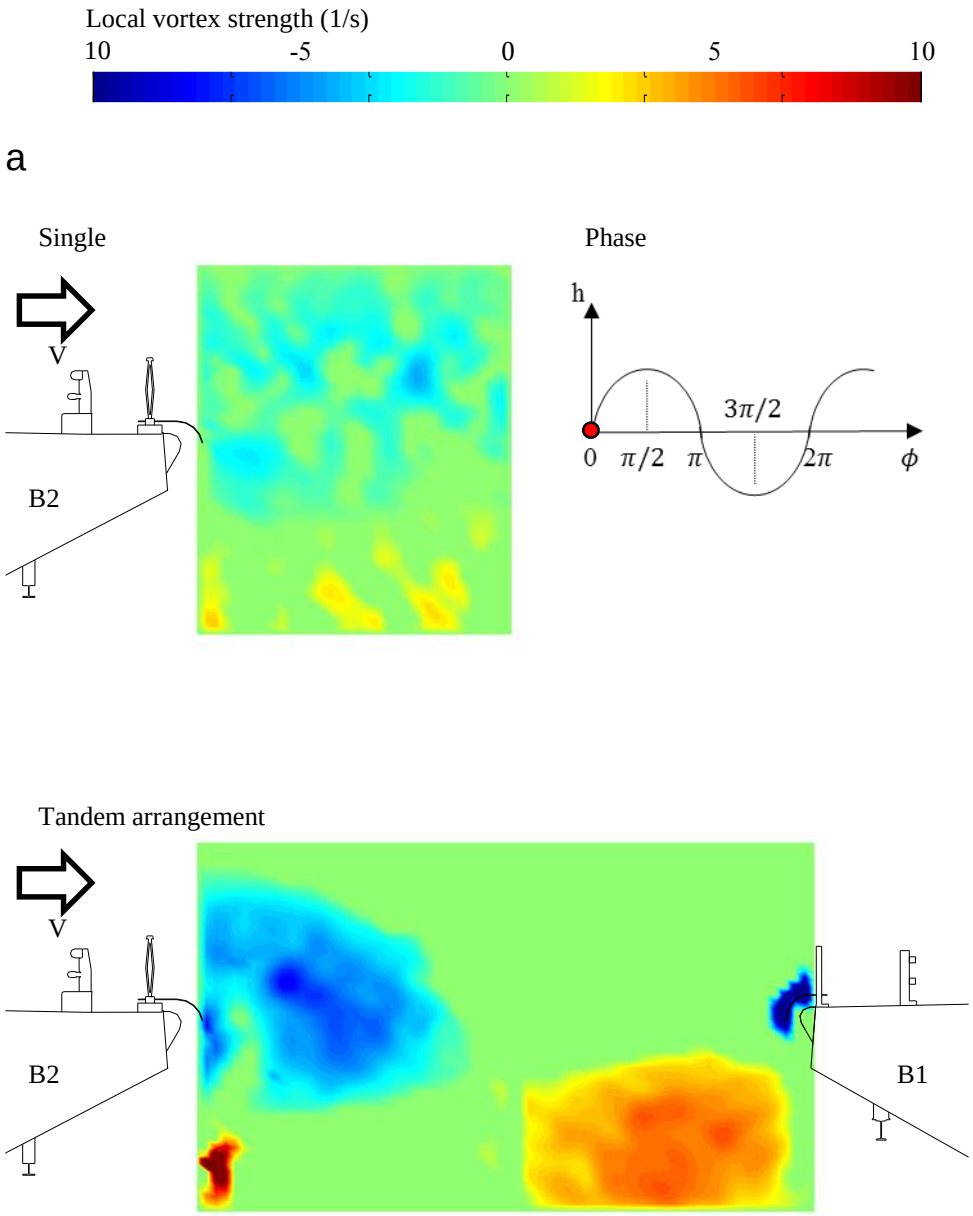

Figure 3.30. Vortex strength field during one period of vertical motion in B2 at $\phi =$ (a) 0, (b) $\pi/4$, (c) $\pi/2$, (d) $3\pi/4$, (e) π, (f) $5\pi/4$, (g) $3\pi/2$ and (h) $7\pi/4$

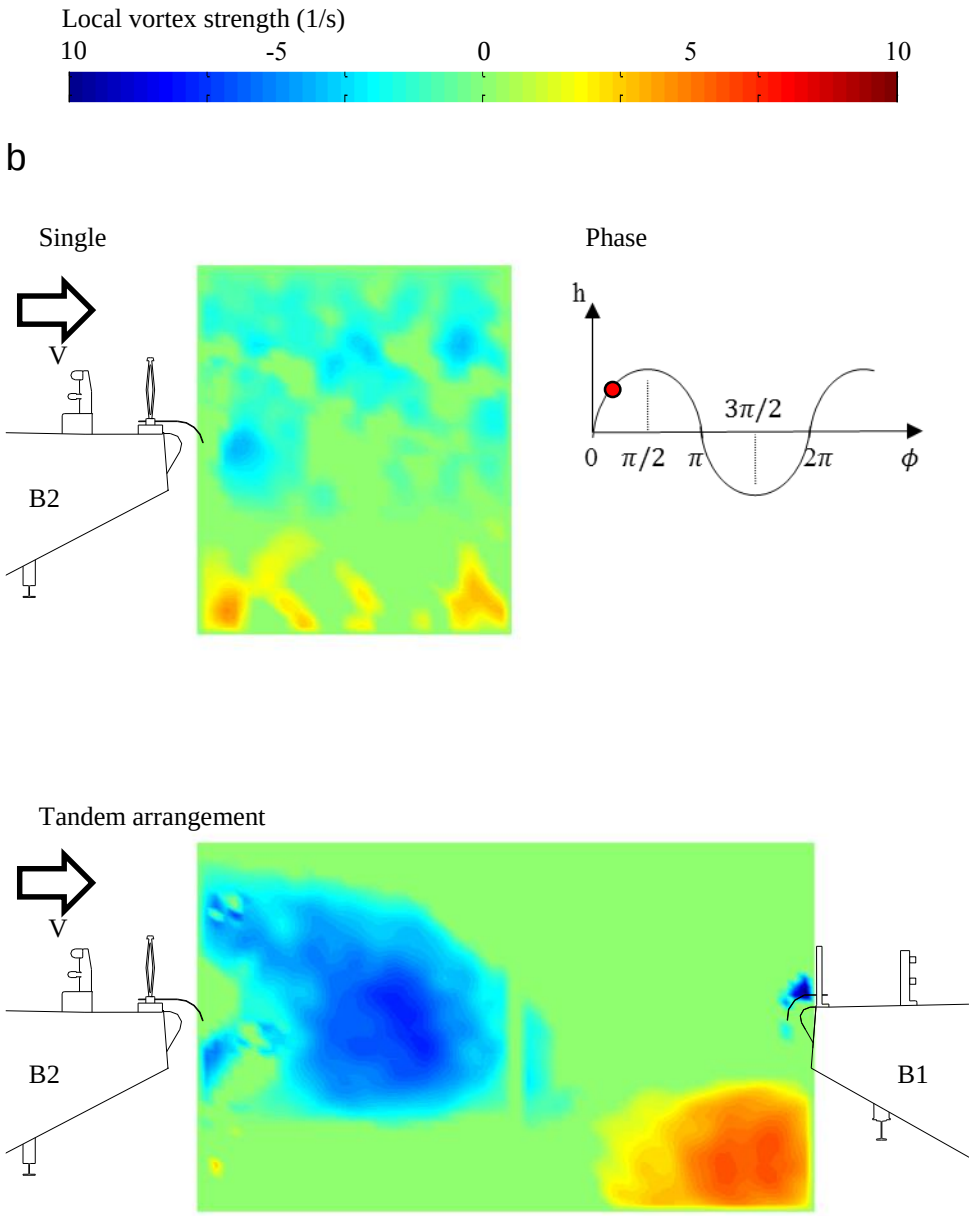

Figure 3.30. Continued.

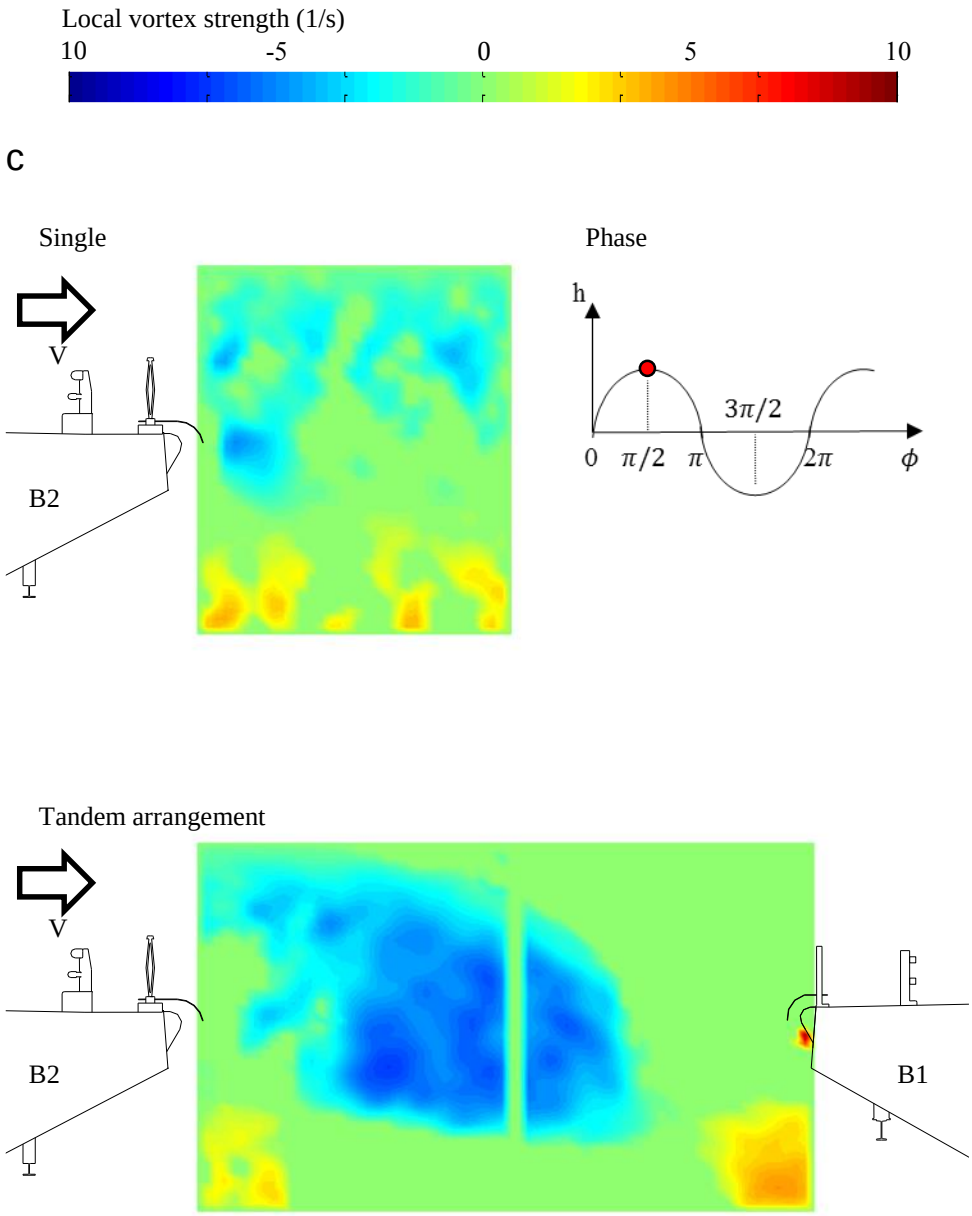

Figure 3.30. Continued.

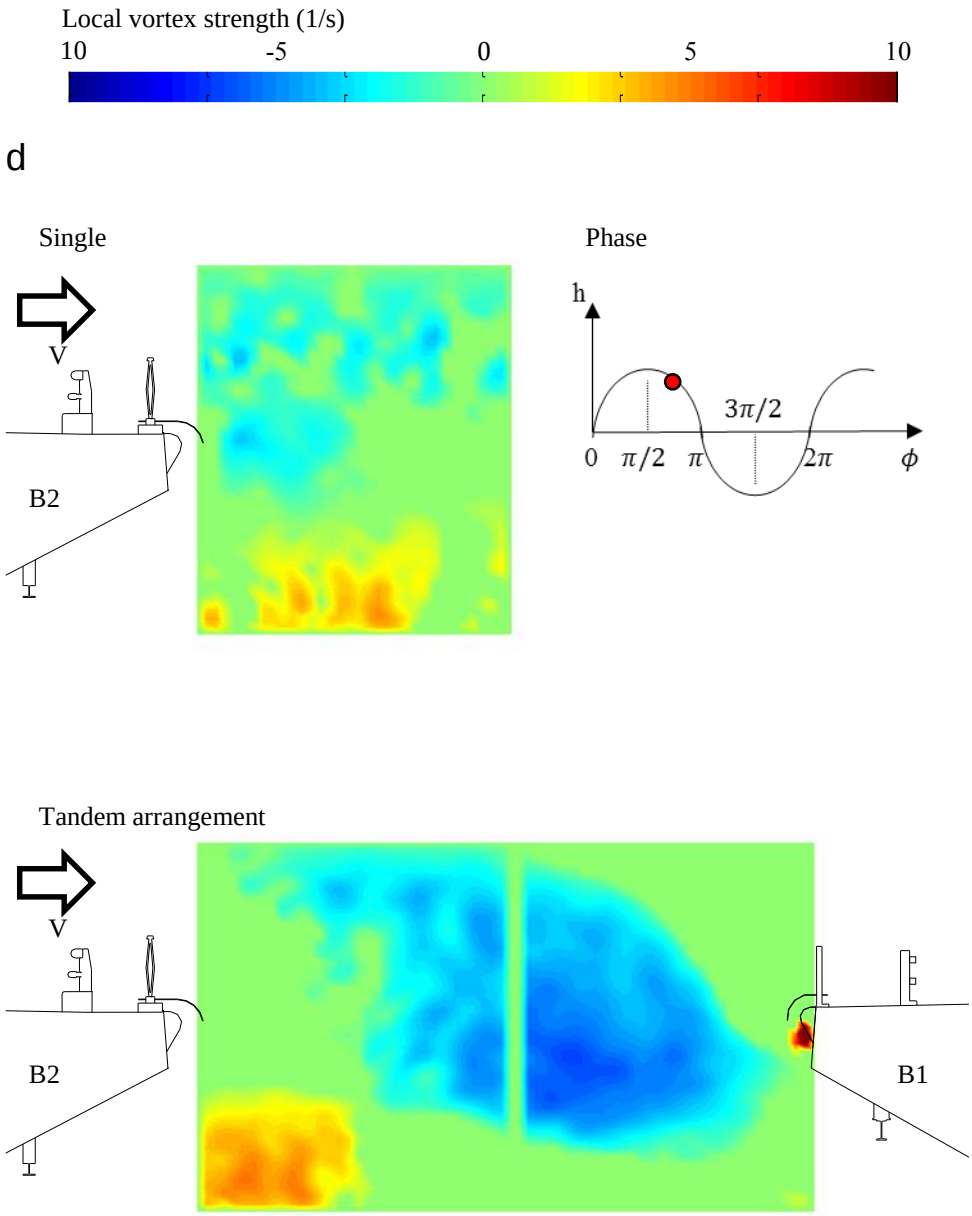

Figure 3.30. Continued.

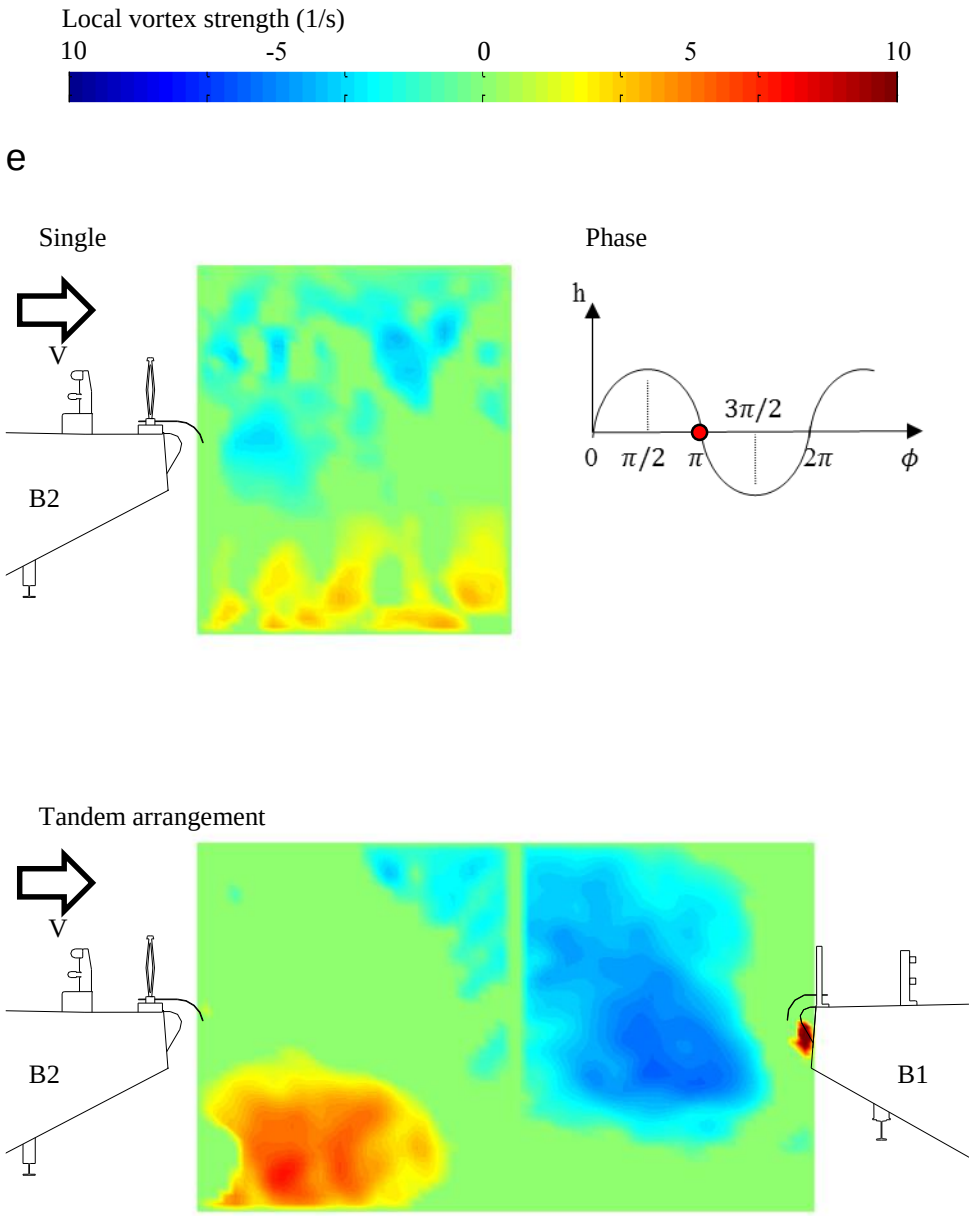

Figure 3.30. Continued.

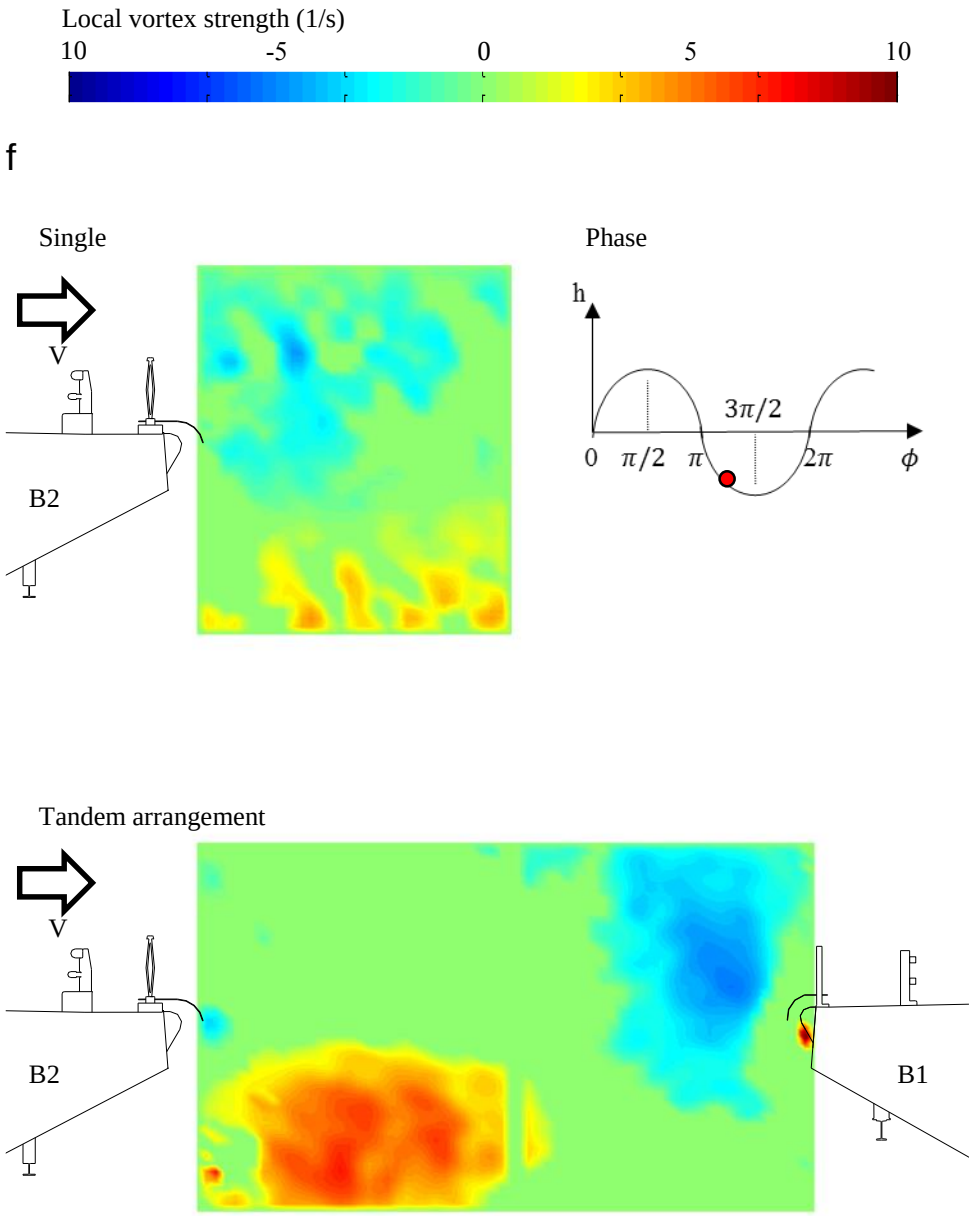

Figure 3.30. Continued.

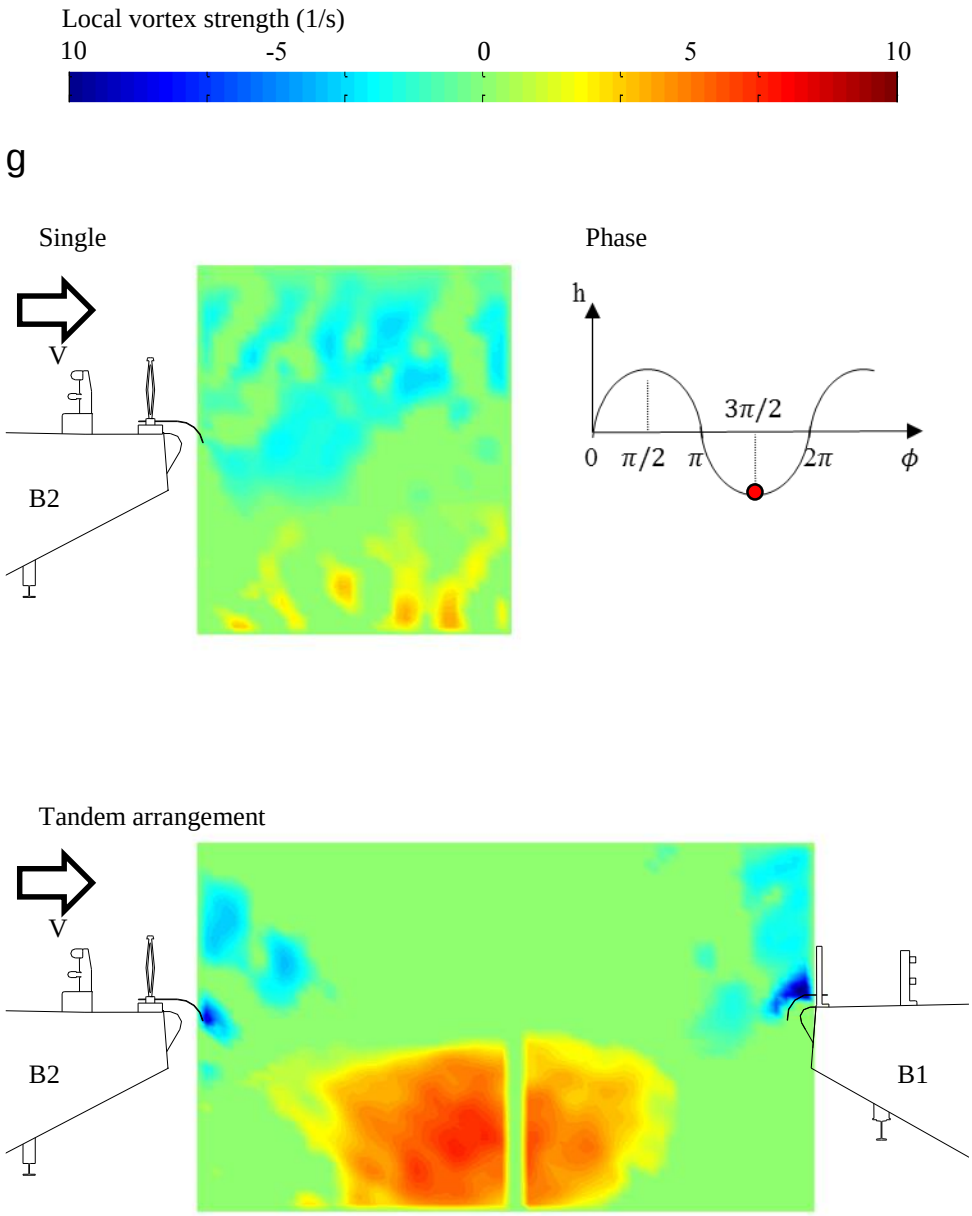

Figure 3.30. Continued.

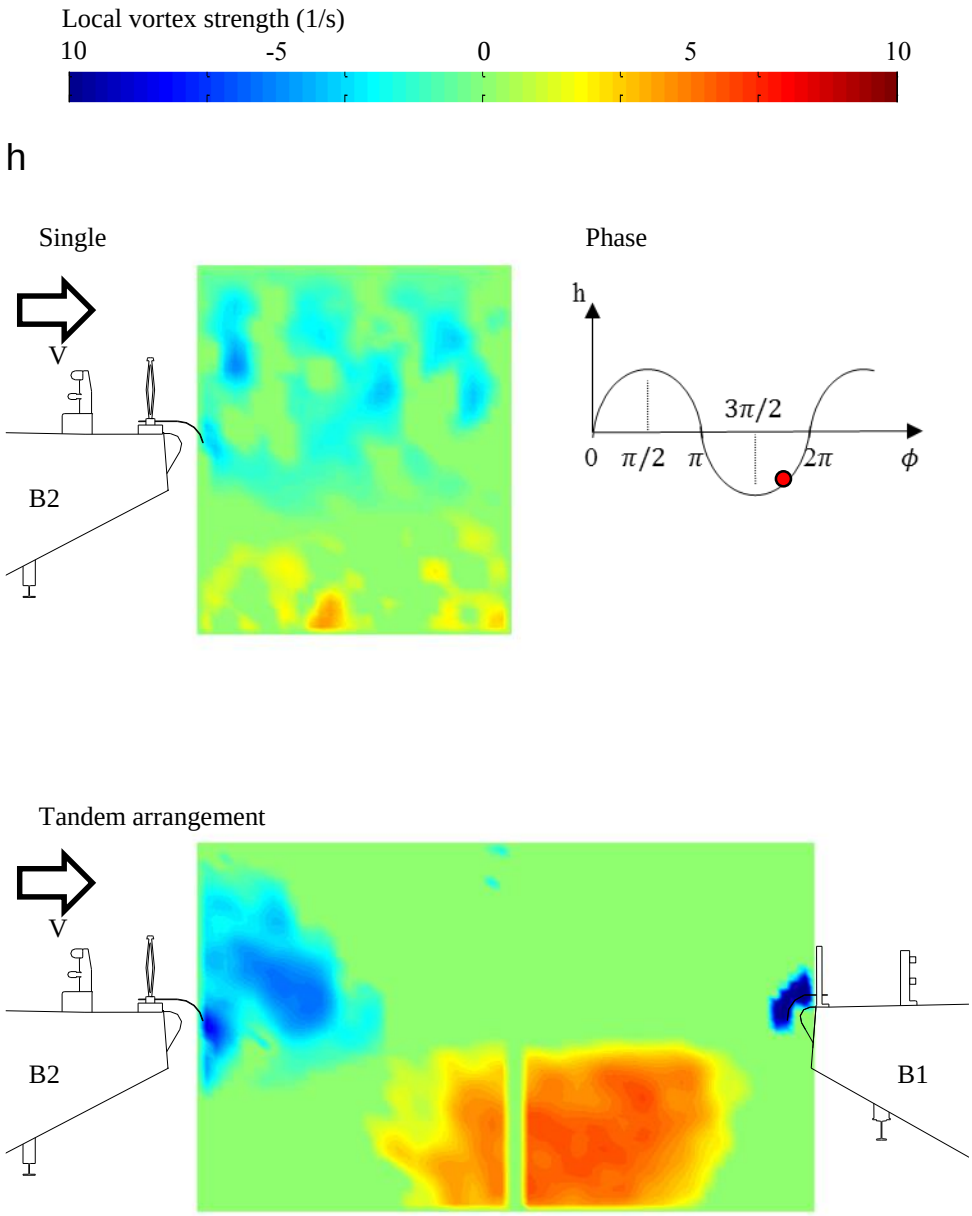

Figure 3.30. Continued.

Chapter 4

Influence of gap distances on vortex-induced vibration

4.1 Influence of gap distances on characteristics of vortex-induced vibration

The previous chapters focus on the VIV in a point of actual Jindo Bridges, resulting in the fixed gap distance. As long as it helps to understand for the current state of the target bridge, the extension of investigation on various gap distances is indispensable for more deep insight on this complicate phenomenon. Also, study about gap distance helps to evaluate how the current gap distance affect to VIV of the target bridges.

Based on this, the vibration responses are intensively investigated for L/D=0.7, 1.3, 2.1, 2.5, 3.0, 3.6, 3.9, 4.6, 5.4, 7.4, 10.6, 14.7, 17.6, 19.5 and ∞. L/D=3.6 is the gap distance of the as-built bridges. The infinity denotes a single deck case.

The results of the Strouhal number with various gap distance clearly show that an existence of the critical gap distance of L/D=2.5 where the vortex begins to form in the gap (Figure 4.1). The PIV tests are conducted after the critical gap distance, so for L/D=2.5, 3.0, 3.6, 3.9, 4.6, 7.4 and 11.3.

The maximum RMS single amplitudes are obtained at fully-developed VIVs in both decks for each gap distance, and summarized in Figure 4.2. In the previous chapter, the VIV of B2 was amplified by the parallel arrangement of two decks, based on the comparative wind tunnel tests between parallel and single deck arrangements with the fixed gap distance of as-built bridges. The same pattern of amplified VIVs are also identified in Figure 4.2 for the gap distances between L/D=2.1 and 5.4, even though the level of amplification is dependent to gap distance. Not only in the windward deck, B2, but also in the leeward deck, B1, the amplification in magnitude of VIV is observed for those gap distances. In fact, the amplitudes of B1 generally exceed those of B2. The peak amplitude of VIVs appears at the gap distance of L/D=3.0, which is close to the case of as-built bridges. The peak amplitudes in both bridges are then decreasing as increasing the gap distance up to L/D=5.4. When the gap distance exceeds over the value of L/D=7.4, the amplitudes of VIV in both decks are not much affected by the gap distance.

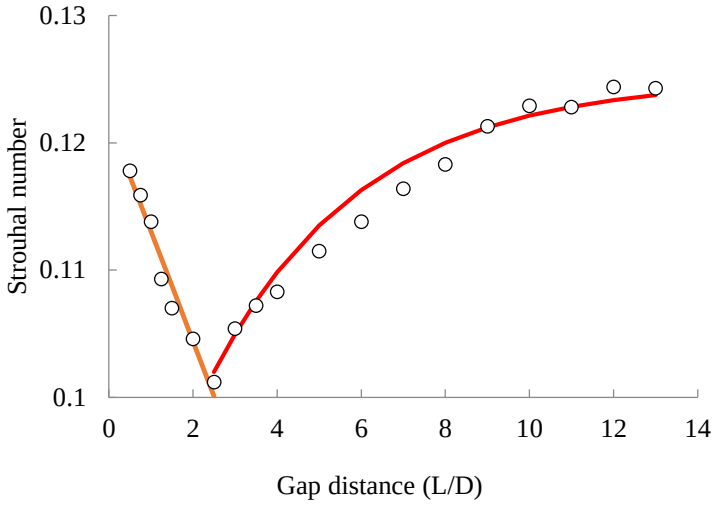

Figure 4.1. The Strouhal numbers for various gap distances

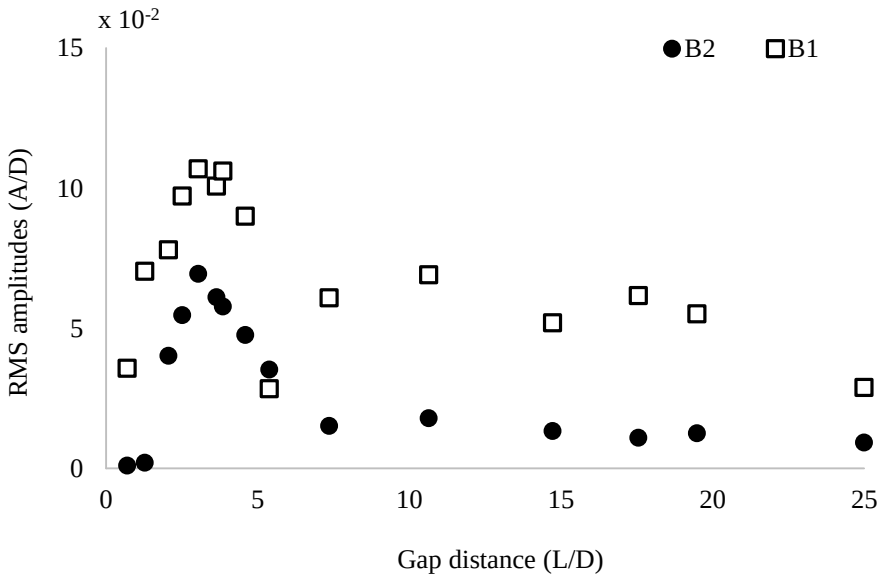

Figure 4.2. The maximum single RMS amplitudes for each gap distance

4.1.1 Interactive VIVs for the gap distances of L/D=0.7-1.3

The A-V curves are shown in Figure 4.3 covering all gap distances considered. Note that Figure 4.3(f) and (o) repeats from Figure 3.11 and Figure 3.8, respectively, for the purpose of comparison. As shown in Figure 4.3(a) and (b), VIV is observable in only the leeward deck (B1) for the narrow gap distance of L/D=0.7 and 1.3. The reduced lock-in wind velocity ranges from V=11 to 16 m/s, and the magnitude of the VIV is also amplified when compared with that for the single deck in Figure 4.3(o). The gap distances between 0.7 and 1.3 seem not to be enough in admitting the formation of vortex trails behind the windward deck.

4.1.2 Interactive VIVs for the gap distances of L/D=2.1-5.4

As the gap distance reaching to L/D=2.1, the VIV starts in the windward deck (B2) as shown in Figure 4.3(c). Further increasing the gap distance leads the VIV in B2 to the peak amplitude at the gap distance of L/D=3.0, as shown in Figure 4.3(e).

Even though the magnitude of VIV in the leeward deck (B1) is also increasing up to the gap distance of L/D=3.0, the lock-in wind velocity of B1 is affected by the VIV motion in the windward deck. As shown in Figure 4.3(c), both decks come into VIV at the same wind speed of 11 m/s. The range of lock-in wind velocity of B2 is enclosed with that of B1. The amplitude of B1 decreases according to the increase of amplitude of B2 at the wind speed of 13 m/s. For the gap distances of $2.5 \leq L/D \leq 4.6$ (see Figure

4.3(d)-(h)), B1 shows VIV in a relatively higher wind velocity than for the case of L/D=2.1 in Figure 4.3(c). The range of lock-in wind velocity of B1 is getting narrow as increasing in gap distance, and finally being enclosed with the lock-in range of B2 at the gap distance of L/D=5.4 as shown in Figure 4.3(i). The amplitude of the VIV in B1 is temporary suppressed to the level of single deck at this gap distance.

Figure 4.4 shows the motional effect of B2 on the VIV in B1. For comparison, the motion of the windward B2 is artificially restrained and the motion of B1 is monitored. As shown in Figure 4.4(a)-(e), the VIVs in B1 become more active with higher amplitudes as well as wider lock-in wind velocities when the motion of B2 is restrained. The motional effect of B2 on the VIV in B1 is maximized at the critical gap distance of L/D=3.0 for this examined bridges and getting weaker as the gap distance increases. However, as the gap distance reaches to L/D=5.4, the lock-in wind velocities in both decks come to the same range and the motional effect of B2 results in four-times difference in the amplitude of B1, as shown in Figure 4.4(f).

4.1.3 Interactive VIVs for the gap distances of L/D=7.4-19.5

The A-V curves of each deck looks similar regardless of gap distance for these range, as shown in Figure 4.3(j)-(n). The motion of B2 is no more severely affected by the parallel disposition of two decks and becomes to the level of single deck case in Figure 4.3(o).

However, the motions in B1 are still different from the single deck case in terms of the amplitude as well as the lock-in range. The time-history of heaving motion and its spectral density for B1are demonstrated in Figure 4.5 for the gap distance of L/D=7.4. B1 is no more in a steady-state VIV motion, as shown in Figure 4.5(a). The spectral density of the motional history also shows relatively spread frequency components around the natural frequency of B1.

Figure 4.6 also shows the spectral density of vertical wind velocity fluctuation measured behind B2. By passing through windward B2, the smooth wind flows in front of B2 come to contain turbulent components. Two peaks corresponding to motional frequencies for B2 (5.1Hz) and B1 (5.9Hz) are shown in Figure 4.6. This implies that the wind flows between two decks are composed of the motion-induced components tuned to each deck oscillation as well as the white-noise turbulent components. The turbulent flow induces B1 to oscillate with the peak factor of 2.2-2.7, which belongs to somewhere between VIV and buffeting vibration.

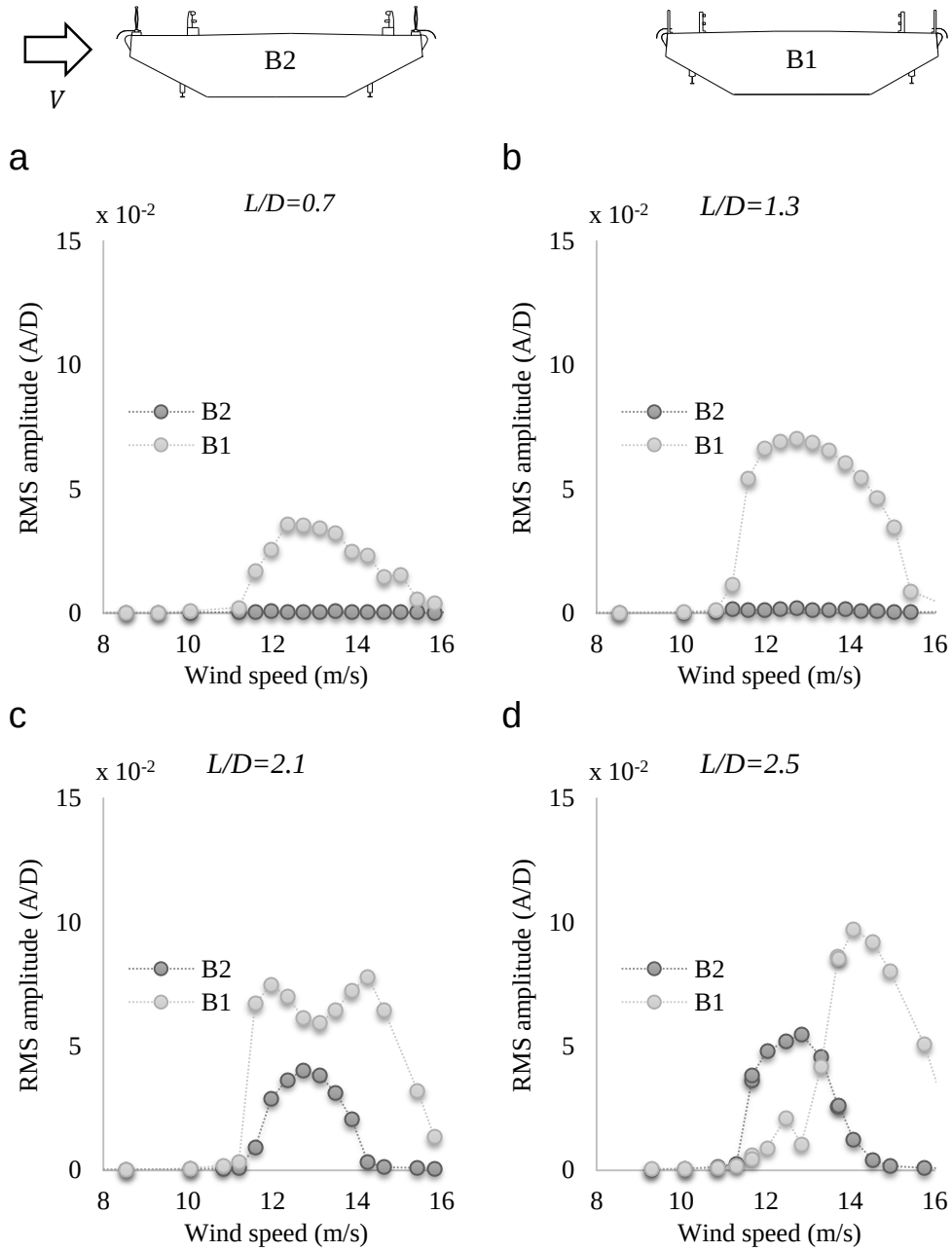

Figure 4.3. A-V curves for the gap distances of (a) 0.7, (b) 1.3, (c) 2.1, (d) 2.5, (e) 3.0, (f) 3.6, (g) 3.9, (h) 4.6, (i) 5.4, (j) 7.4, (k) 10.6, (l) 14.7, (m) 17.6, (n) 19.5 and (o) infinity

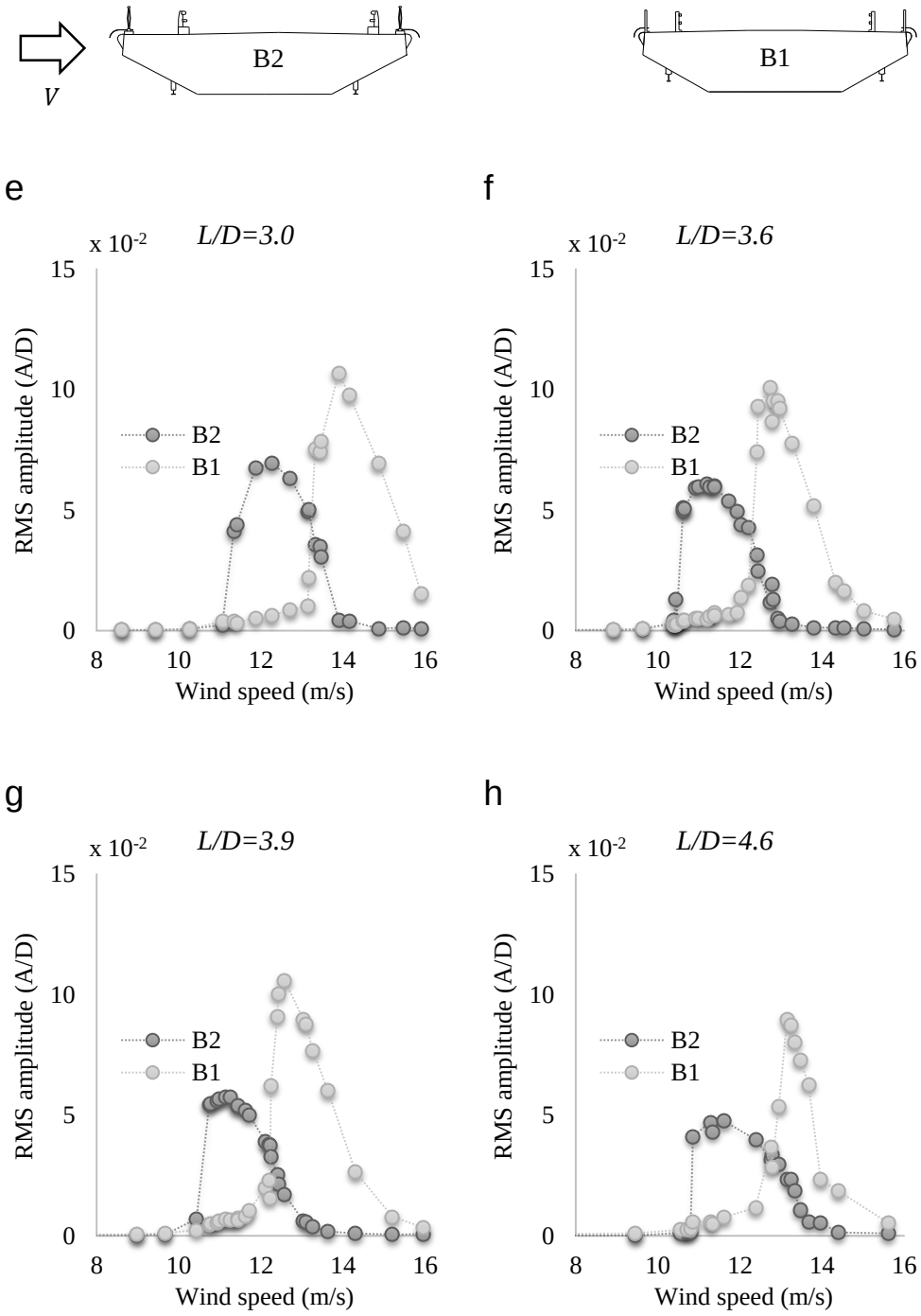

Figure 4.3. Continued.

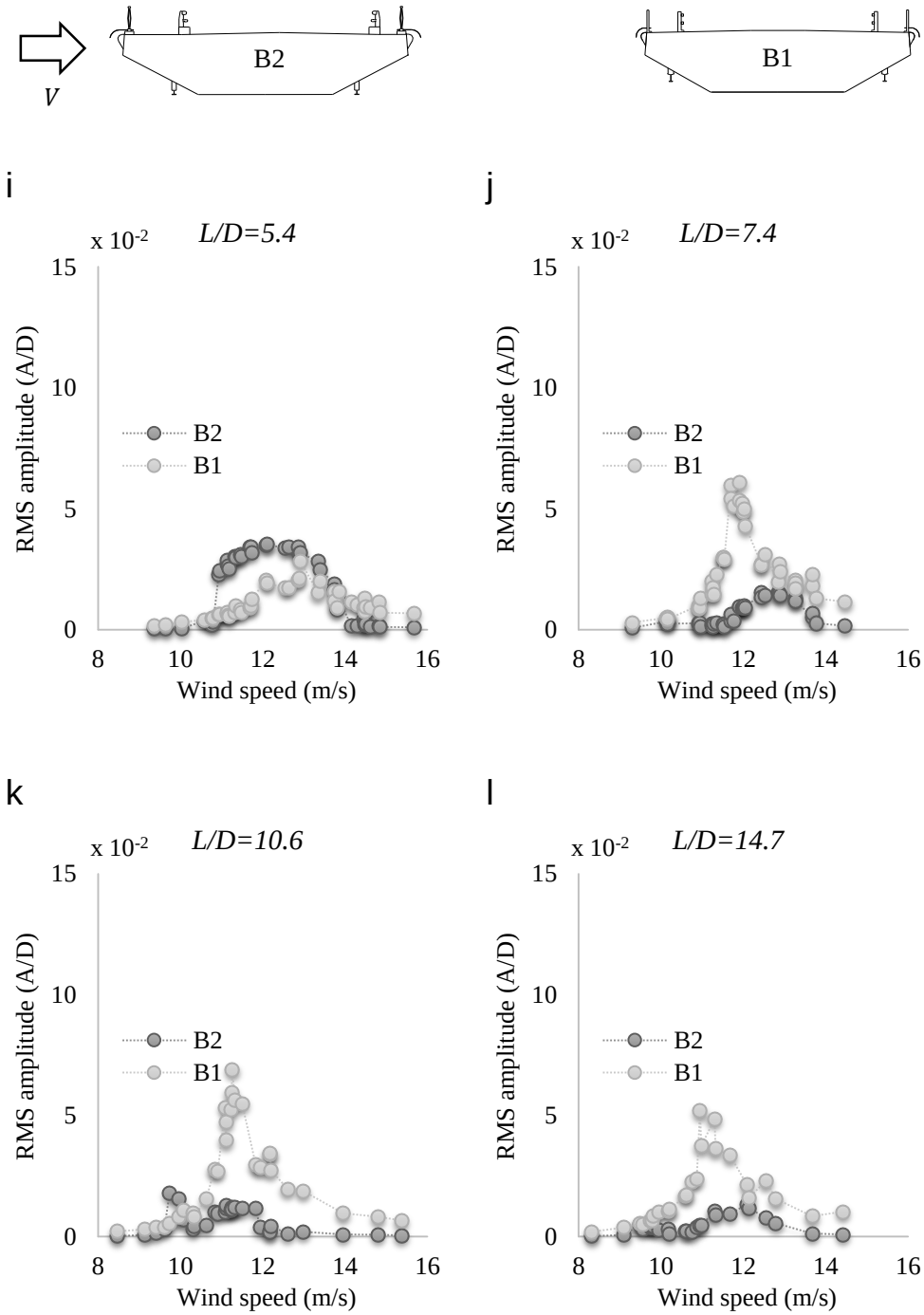

Figure 4.3. Continued.

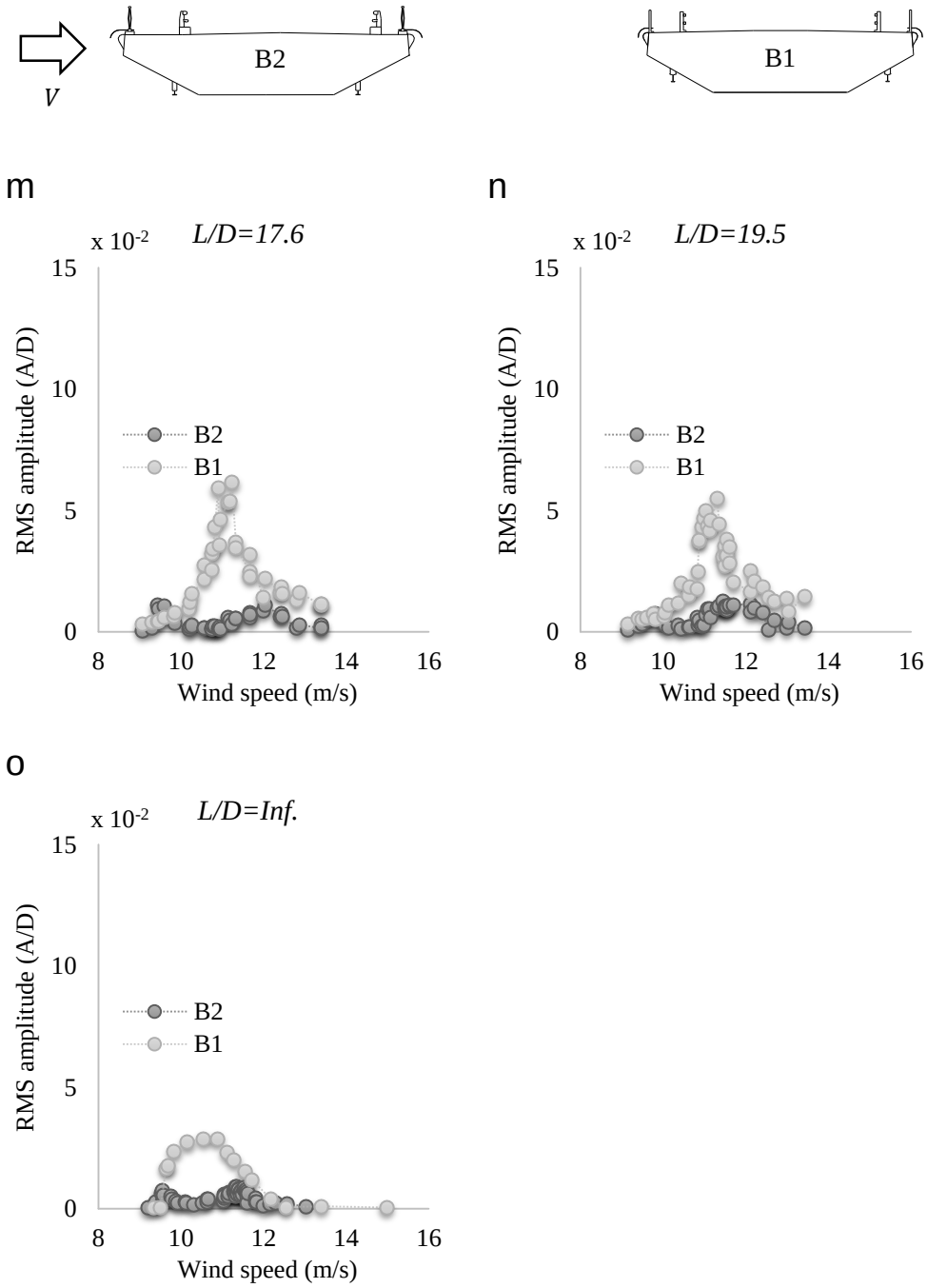

Figure 4.3. Continued.

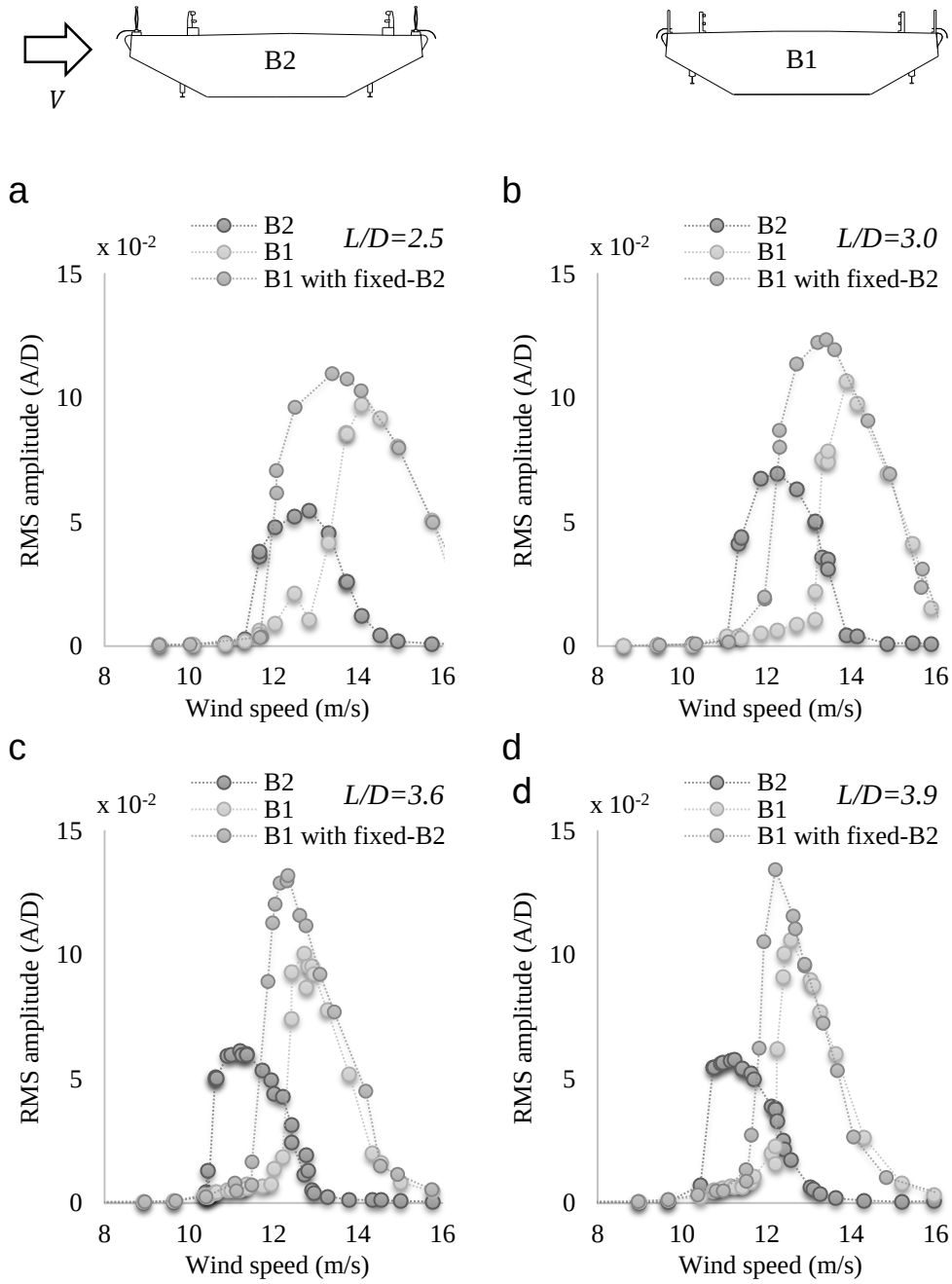

Figure 4.4. A-V curves of B1 while the motion of B2 is being restrained or released at gap distances of (a) 2.5, (b) 3.0, (c) 3.6, (d) 3.9, (e) 4.6 and (f) 5.4

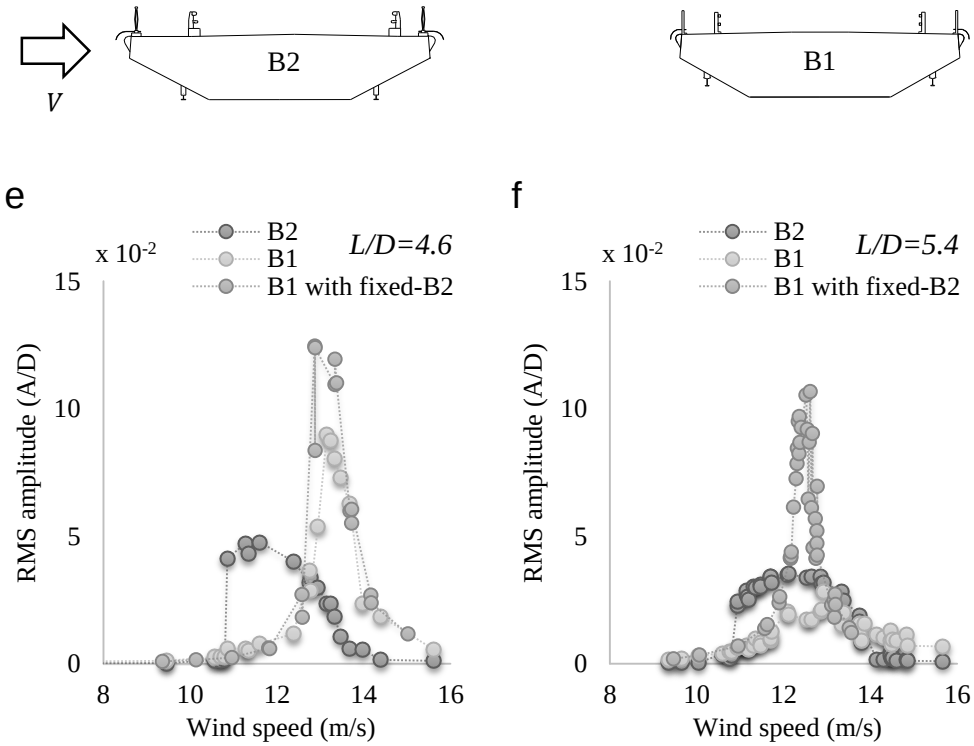

Figure 4.4. Continued.

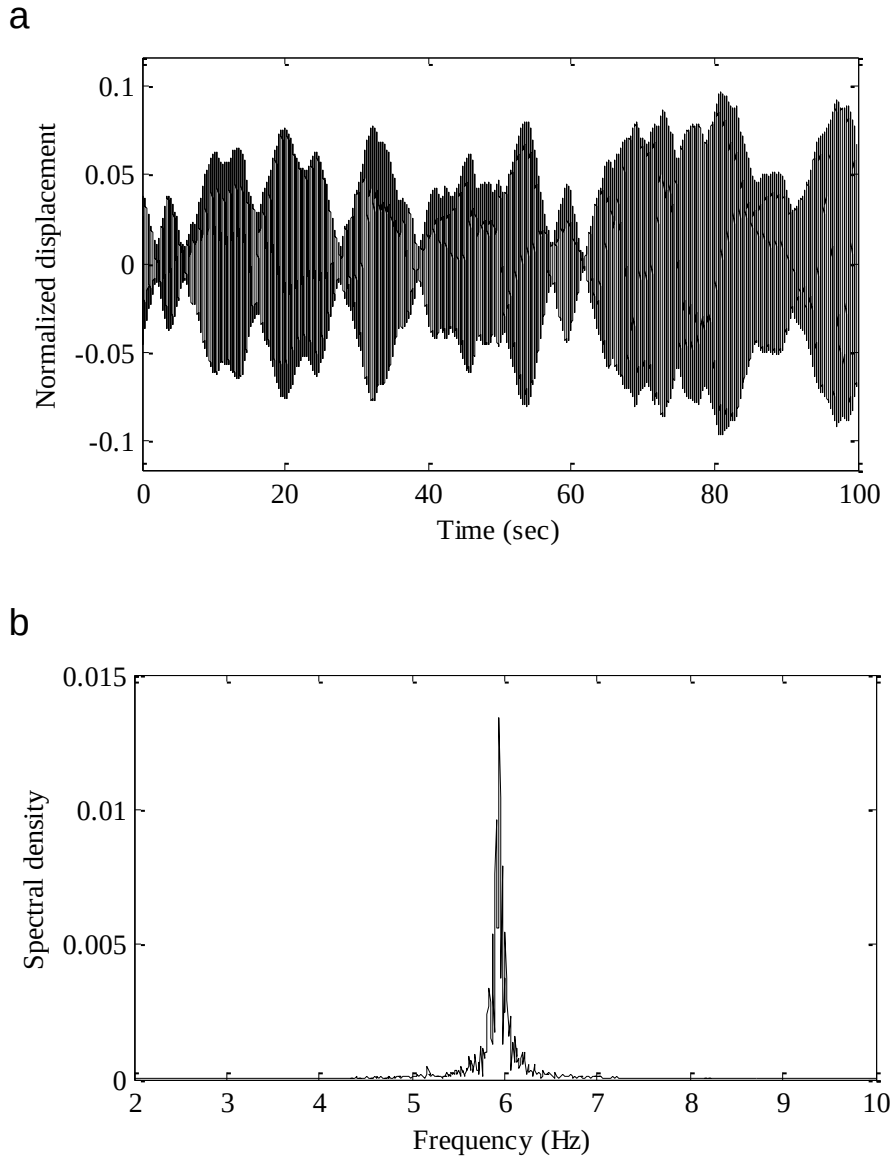

Figure 4.5. (a) Time history of normalized vertical displacement of B1 and (b) its spectral density at L/D=7.4 and V/nD=10.3

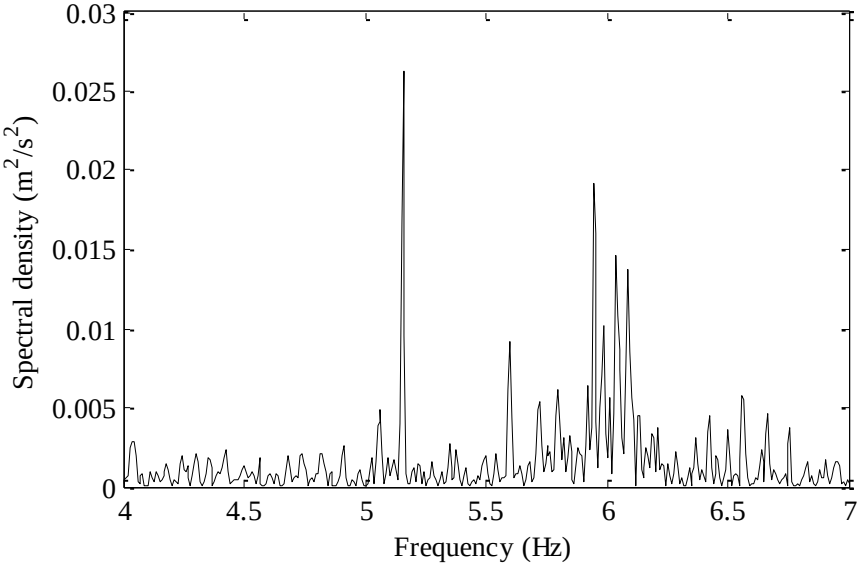

Figure 4.6. Spectral density of vertical wind velocity fluctuation measured behind B2 at L/D=7.4 and V/nD=10.3

4.2 Flow fields observation in the gap

4.2.1 Motion induced flow fields at various gap distance

The magnitude of wind velocity and stream line for the two particular phases of $\phi = \pi/2$ and $3\pi/2$ are illustrated in Figure 4.7. As discussed for L/D=3.6 in Chapter 3, the alternating Ω and ʊ -shaped streamlines are well identified behind B2 from L/D=2.5 to L/D=11.3. When the wind velocity was taken into consideration, the vertical upward and downward flows could be identified with sky-blue color for the gap distances of 3.0 and 4.6, which demonstrates the existence of relatively fast vertical flows between two decks for those gap distances. When the gap distance increase than 7.4, where the VIV of upstream deck escapes from the interference effect of tandem arrangement, low velocity area behind B2 expands till L/D= 5 to 6. The wind speed at area behind B2 decreases less than 2 m/s such as single B2 case. The magnitude of wind speed begins to increase after L/D=7 but the horizontal component is dominant.

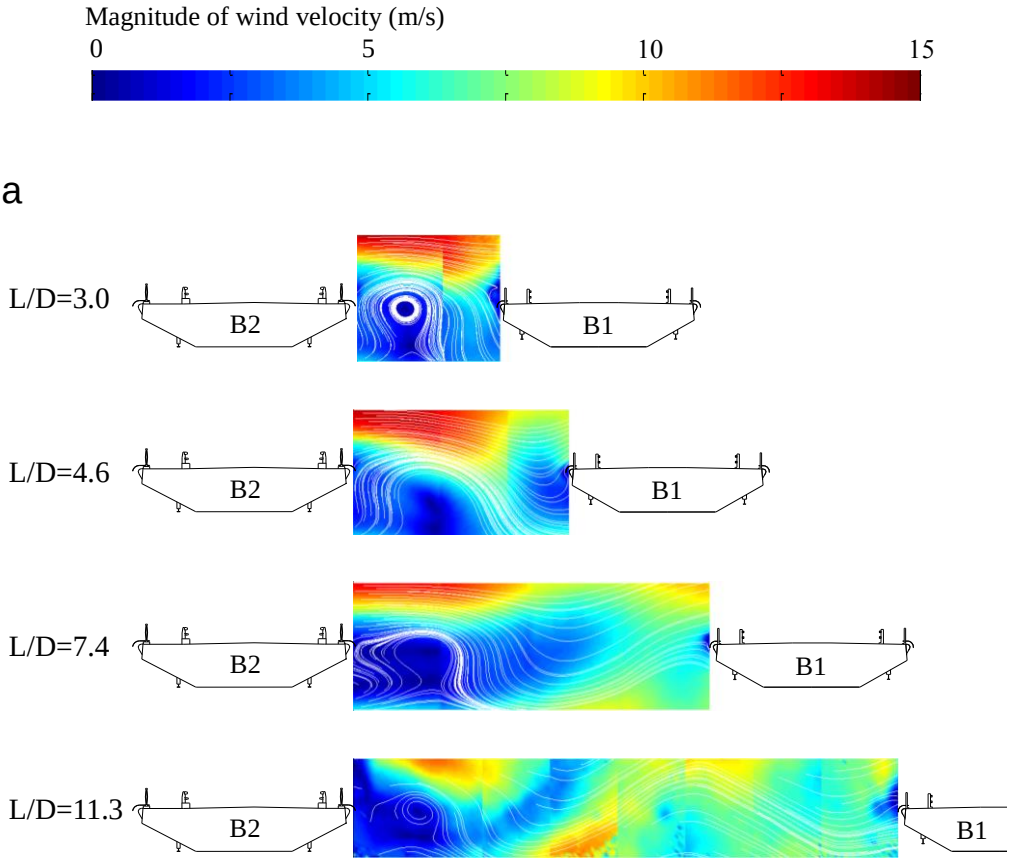

Figure 4.7. Magnitude of wind velocity and stream line according to the gap distances at $\phi =$ (a) $\pi/2$ and (b) $3\pi/2$

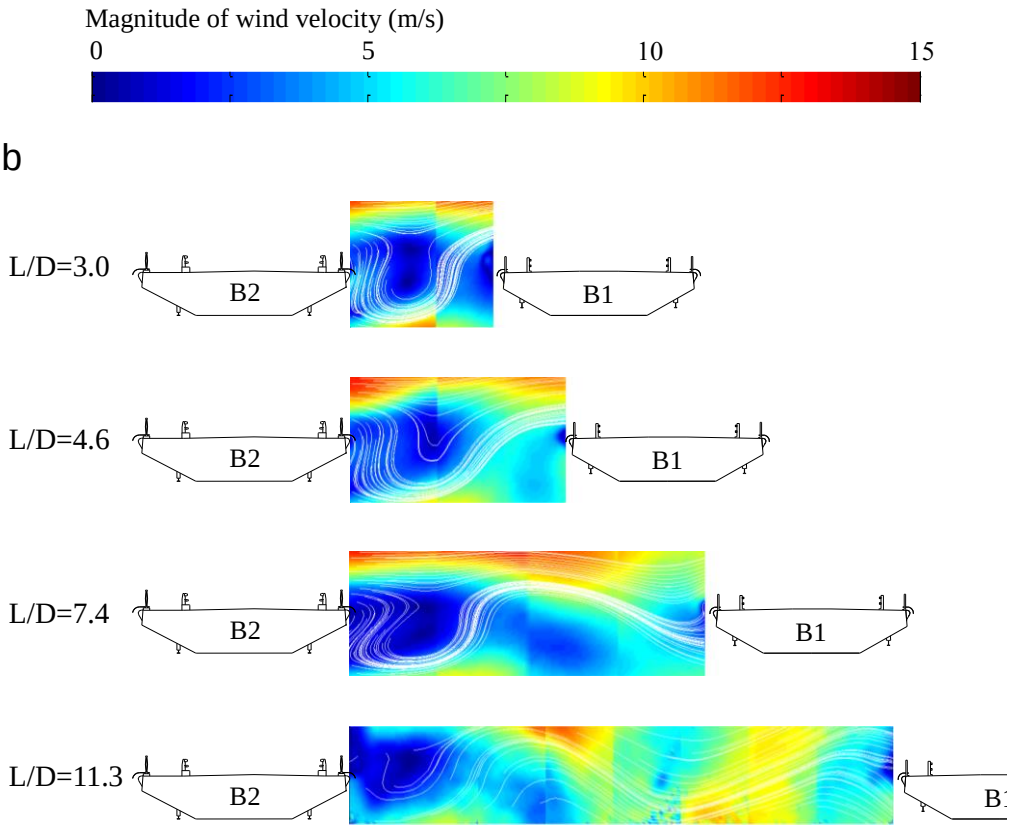

Figure 4.7. Continued

4.2.2 Influences of gap distances on vortex fields

The magnitude of wind velocity and stream line for the two particular phases of $\phi = \pi/2$ and $3\pi/2$ are illustrated in Figure 4.8. The vortex strengths are strong when the gap distance ranges from 3.0 to 3.9. For this range, the generated vortex from B2 almost reached B1 during one cycle of motion of B2. When the gap size increased, the shape of the generated vortex was spread out, and the swirling strength became weak. The moving distance of the generated vortex during the one cycle of motion of B2 became shorter than the distance between the two decks. This illustrates the fact that the vortices were well developed when the time duration for the vortices crossing the gap distance approximated the motional period of B2. As shown in Figure 4.8, the time duration and the motional period exactly matched at a gap distance of L/D=3.0, for which the strongest interactive VIVs were observed in both decks, as shown Figure 4.3 (e). Accordingly, the formation of magnified vortices was the result of the synchronization between the one period of the heaving motion of the windward deck and the time required for the vortex movement between two decks, particularly for gap distances that fell between 2.5 and 4.6. This can be considered another type of the lock-in phenomenon in a parallel deck disposition.

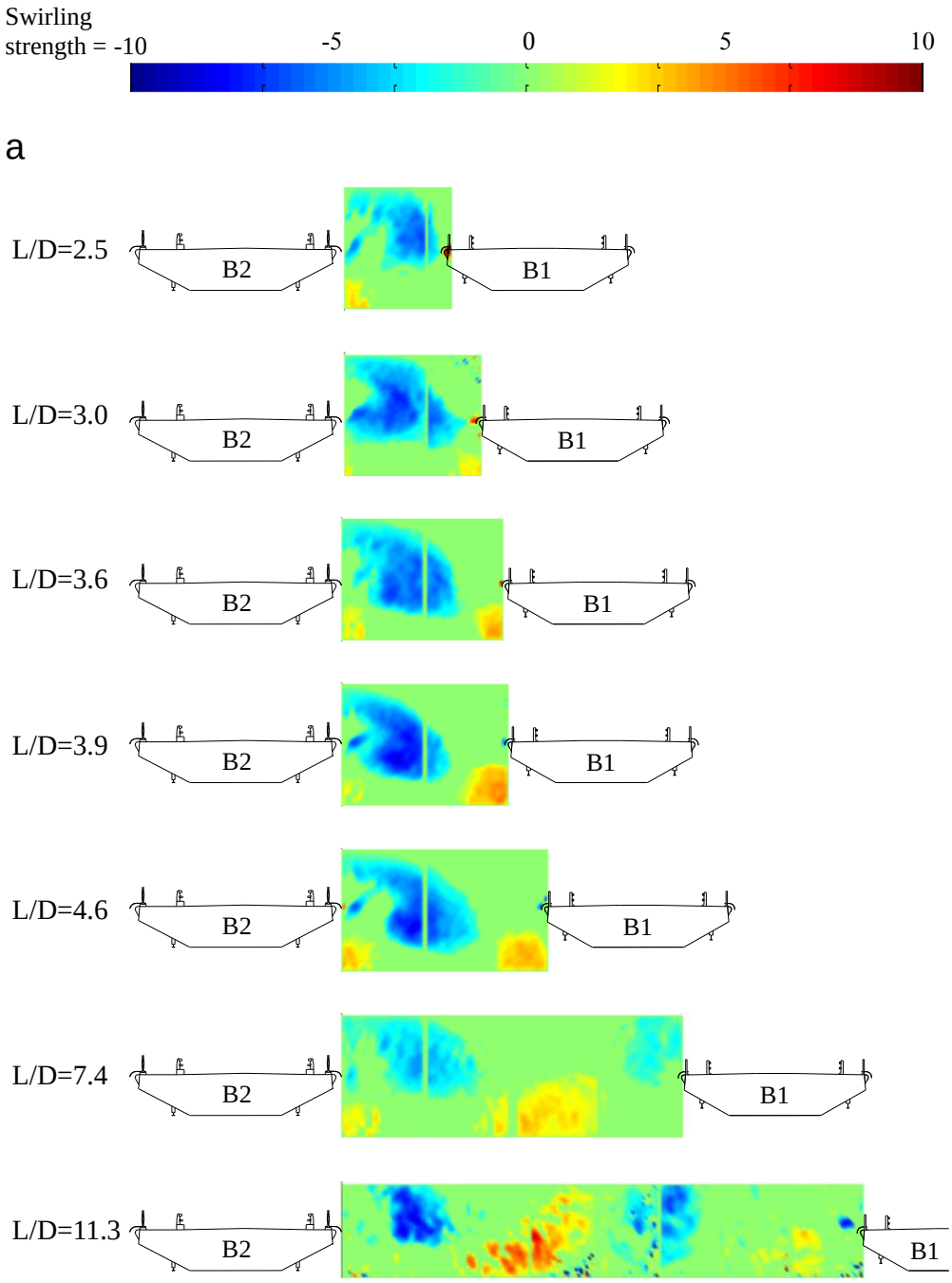

Figure 4.8. Swirling strength according to the gap distances at $\phi =$ (a) $\pi/2$ and (b) $3\pi/2$

b

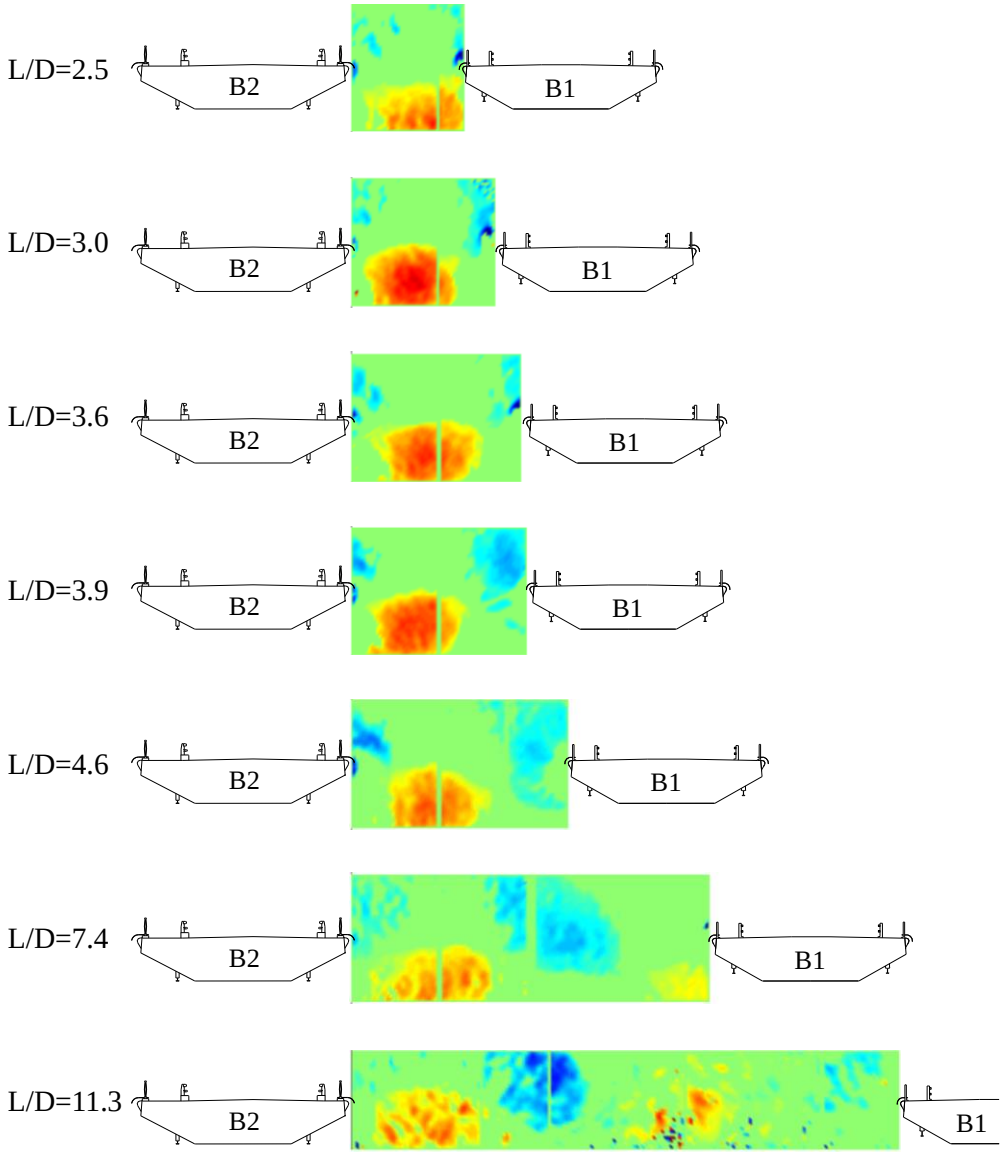

Figure 4.8. Continued.

4.2.3 Vortex moving speed analysis

The moving distance of the generated vortex during the one cycle of motion of upstream deck is an important factor for amplification of VIV. Then, the vortex moving speed in the gap directly decides the vulnerable gap distance. If v_{vor} is the vortex moving speed, then the moving distance of the generated vortex during the one cycle of motion of the deck can be expressed as

$$\frac{L}{D} = \frac{v_{\mathrm{vor}} \cdot T}{D} = \frac{v_{\mathrm{vor}}}{f \cdot D} = \frac{k}{St} \tag{4.1}$$

where a factor k is the ratio of the vortex moving speed to the free stream wind speed, $k = v_{\mathrm{vor}}/V$.

Plots in Figure 4.9 show the vortex strength on time-space domain. The x- and y-axis represent horizontal distance and time, respectively, then each slope corresponds to the vortex moving speed (Figure 4.9 (b)). As shown in figures, the slopes are consistent regardless of time and the gap distance. The factor, *k*, is calculated as value of 0.30. Thus, the gap distance for vulnerable can be calculated as L/D=2.5-3.0 with the Strouhal numbers at various gap distances shown in Figure 4.1.

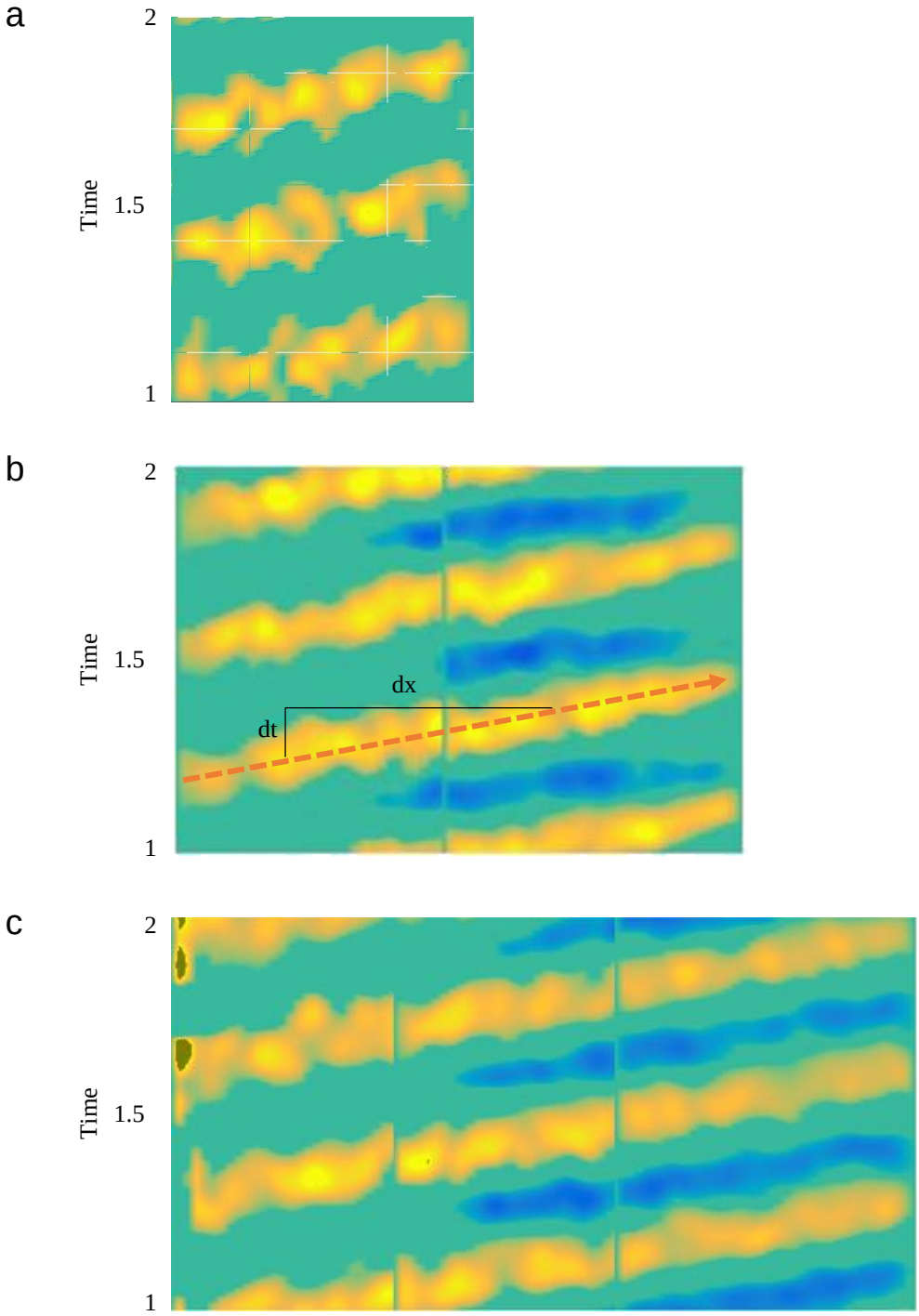

Figure 4.9. Trace of vortex moving at (a) L/D=2.5, (b) L/D=3.6 and (c) L/D=4.6

Chapter 5

Conclusions and further study

This study investigated the aerodynamic interactive vibrations of Jindo Bridges. The interfered effects of parallel arrangement were observed in VIV, flutter instability and buffeting response.

B2 in 2011 at upstream experienced a steady-state vibration tuning the lock-in velocity for the first vertical mode. A series of wind tunnel tests were carried out and the observed phenomenon was successfully reproduced. Through comparative wind tunnel tests for a single disposition of the bridge, it was found that the VIV of B2 was amplified due to the interactive effect between parallel decks. Through PIV tests, alternating eddies were observed at the top and bottom corners of the upstream deck in phase with the deck vibration. The comparative investigation of PIV images demonstrates that the parallel disposition amplifies alternating "Ω" and "℧" shaped flow fields between two decks.

In depth study for the gap distances was carried out. The considered gap distance covers from 0.7 to 19.5 in terms of non-dimensional variable defined as the actual distance divided by the depth of windward deck. It is found that the gap distance is a critical factor in estimating the interactive motions of two bridge decks. The maximum

amplitudes of VIVs and the ranges of lock-in wind velocity in both bridges changed a lot according to the gap distance. For small gap distances of 0.7 and 1.3, a VIV could only be identified in the downstream deck. As the gap distance was increased from 2.1 to 5.4, the vortices generated from the leeward edge of the upstream deck were magnified between the two decks. However, due to the differences in the natural frequencies between the two decks, strong oscillations in both decks were not simultaneously observed. The PIV tests demonstrated that the strength of the vortex reached its maximum level when the time duration for the vortices crossing the gap distance approximated that of the one-motional period of the upstream deck. As the gap distance increased to more than 7.4, the interactive VIVs almost disappeared and only buffeting-type vibrations were observed in the downstream deck due to the disturbed flow by the upstream deck.

Accordingly, it can be concluded that the interactive VIV in two cable-stayed bridges in tandem is critically affected by a gap distance up to five to seven times of the depth of the deck. Jindo Bridges have been built with close to the most vulnerable distance. If the 2nd Jindo Bridge had been constructed with a half or double of as-is gap distance, the VIV problem would not appear. This vulnerable gap distance is closely related to the moving distance of one vortex during one-period oscillation of the deck that corresponds to the vortex moving speed. The vulnerable gap distance can be estimated, if the vortex moving speed and the Strouhal number are known.

However, since the characteristics of interactive VIV seem to also be dependent on factors such as the relative differences in natural frequencies, inherent dampings, and external shapes of opposing decks, it is required more investigations for the generalization for the findings to apply on other bridge case.

To generalize the findings in this study, following investigations are recommended. Investigation for the flow fields during the VIV of downstream deck at higher wind speed provides more deep insight the relation between the motion and flow structure. Vibration of the upstream or the downstream deck may be simply a problem of relative displacement of two decks as long as the flow structure is mainly affected by the boundary conditions. Comparison the results from the VIV of the downstream with those in this study is expected to give an answer.

In this study, the differences in natural frequencies of both decks will be the new key parameter related with interference phenomena between two decks. A parameter study on this is required. A partial consequences where the upstream deck has higher frequency than that of the downstream deck were introduced through the change of wind direction. The section at lower natural frequency vibrated first regardless of its position, but results at intermediate wind speed were different. In this study, closely spaced two natural frequencies reduced the vibration of the downstream deck. In the case of circular cylinders, however, even instability appeared at downstream cylinder because of perfectly same frequencies.

References

Argentini, T., Rocchi, D., Zasso, A., 2015. Aerodynamic interference and vortex-induced vibrations on parallel bridges: The Ewijk bridge during different stages of refurbishment. Journal of Wind Engineering and Industrial Aerodynamics 147, 276-282.

Brika, D., Laneville, A., 1999. The flow interaction between a stationary cylinder and a downstream flexible cylinder. Journal of Fluids and Structures 13, 579-606.

Chen, W.-L., Li, H., Hu, H., 2014. An experimental study on the unsteady vortices and turbulent flow structures around twin-box-girder bridge deck models with different gap ratios. Journal of Wind Engineering and Industrial Aerodynamics 132, 27-36.

Grillaud, G., Chauvin, A., Bietry, J., 1992. Comportement dynamique d'un Pont à haubans dans une turbulence de sillage. Journal of Wind Engineering and Industrial Aerodynamics 42, 1181-1189.

HDEC, 2000. Report on the monitoring of Jindo Bridge (in Korean).

He, H.X., Li, J.W., 2015. Study on the Effect and Mechanism of Aerodynamic

Measures for the Vortex-Induced Vibration of Separate Pairs of Box Girders in Cable-Stayed Bridges. Shock and Vibration 2015, 1-11.

Honda, A., Shiraishi, N., Matsumoto, M., Fuse, Y., Sumi, K., Sasaki, N., 1993. Aerodynamic stability of Kansai International Airport access bridge. Journal of Wind Engineering and Industrial Aerodynamics 49, 533-542.

Hussain, A.K.M.F., Reynolds, W.C., 1970. The mechanics of an organized wave in turbulent shear flow. Journal of Fluid Mechanics 41, 241-258.

Irwin, P.A., Stoyanoff, S., Xie, J., Hunter, M., 2005. Tacoma Narrows 50 years later—wind engineering investigations for parallel bridges. Bridge Structures 1, 3-17.

Jang, S., Jo, H., Cho, S., Mechitov, K., Rice, J.A., Sim, S.H., Jung, H.J., Yun, C.B., Spencer, B.F., Agha, G., 2010. Structural health monitoring of a cable-stayed bridge using smart sensor technology: deployment and evaluation. Smart Structures and Systems 6, 439-459.

Kim, S.J., Kim, H.K., Calmer, R., Park, J., Kim, G.S., Lee, D.K., 2013. Operational field monitoring of interactive vortex-induced vibrations between two parallel cable-stayed bridges. Journal of Wind Engineering and Industrial Aerodynamics 123, 143-154.

Kimura, K., Shima, K., Sano, K., Kubo, Y., Kato, K., Ukon, H., 2008. Effects of separation distance on wind-induced response of parallel box girders. Journal of Wind Engineering and Industrial Aerodynamics 96, 954-962.

KSCE, 2006. Design guidelines for steel cable-supported bridges, Korea.

Kwok, K.C.S., Qin, X.R., Fok, C.H., Hitchcock, P.A., 2012. Wind-induced pressures around a sectional twin-deck bridge model: Effects of gap-width on the aerodynamic forces and vortex shedding mechanisms. Journal of Wind Engineering and Industrial Aerodynamics 110, 50-61.

Laima, S., Li, H., 2015. Effects of gap width on flow motions around twin-box girders and vortex-induced vibrations. Journal of Wind Engineering and Industrial Aerodynamics 139, 37-49.

Larsen, A., Savage, M., Lafrenière, A., Hui, M.C.H., Larsen, S.V., 2008. Investigation of vortex response of a twin box bridge section at high and low Reynolds numbers. Journal of Wind Engineering and Industrial Aerodynamics 96, 934-944.

Larsen, S.V., Astiz, M.A., Larose, G.L., 2000. Aerodynamic interference between two closely spaced cable supported bridges, Proceedings of the 4th International Colloquium on Bluff Body Aerodynamics and Applications, Bochum, pp. 33-37.

Lee, S.H., Yoon, J.G., Kwon, S.D., 2013. Aerodynamic Forces Acting on Yi Sun-sin Bridge Girder According to Reynolds Numbers. Journal of the Korean Society of Civil Engineers 33, 93-100.

Liu, Z., Chen, Z., Liu, G., Shao, X., 2009. Experimental study of aerodynamic interference effects on aerostatic coefficients of twin deck bridges. Shock Vib 3, 292-298.

Matsuda, K., Cooper, K.R., Tanaka, H., Tokushige, M., Iwasaki, T., 2001. An investigation of Reynolds number effects on the steady and unsteady aerodynamic forces on a 1 : 10 scale bridge deck section model. Journal of Wind Engineering and Industrial Aerodynamics 89, 619-632.

Meng, X., Zhu, L., Guo, Z., 2011. Aerodynamic interference effects and mitigation measures on vortex-induced vibrations of two adjacent cable-stayed bridges. Shock Vib 5, 510-517.

Schewe, G., 2001. Reynolds-number effects in flow around more-or-less bluff bodies. Journal of Wind Engineering and Industrial Aerodynamics 89, 1267-1289.

Schewe, G., Larsen, A., 1998. Reynolds number effects in the flow around a bluff bridge deck cross section. Journal of Wind Engineering and Industrial Aerodynamics

74-6, 829-838.

Spencer Jr, B., Cho, S., Sim, S.-H., 2011. Wireless monitoring of civil infrastructure comes of age. Structure 13.

Sumner, D., 2010. Two circular cylinders in cross-flow: A review. Journal of Fluids and Structures 26, 849-899.

Tanaka, H., 1990. Similitude and modelling in wind tunnel testing of bridges. Journal of Wind Engineering and Industrial Aerodynamics 33, 283-300.

Xu, G., Zhou, Y., 2004. Strouhal numbers in the wake of two inline cylinders. Experiments in Fluids 37.

Zdravkovich, M.M., 1985. Flow induced oscillations of two interfering circular cylinders. Journal of Sound and Vibration 101, 511-521.

Zhou, J., Adrian, R.J., Balachandar, S., Kendall, T.M., 1999. Mechanisms for generating coherent packets of hairpin vortices in channel flow. Journal of Fluid Mechanics 387, 353-396.

국 문 초 록

2011년 병렬배치를 이루고 있는 사장교량인 진도대교에서 사용성 기준을 크게 초과하는 와류진동이 발생하였다. 진동이 발생한 제 2진도대교가 풍상측에 위치했었다는 점과 비슷한 구조형식 및 외관의 제 1진도대교에선 유사한 보고가 없었던 점이 이슈가 되었다. 일련의 풍동실험을 결과 진도대교에서의 와류진동에 교량의 병렬배치로 인한 간섭현상이 중요한 요인으로 작용하고 있었다.

이에 대한 보다 자세한 연구를 위하여 두 교량의 간격을 주요 파라미터로 하여 거더의 단면 높이의 최대 20 배까지 간격에 대한 병렬교량의 와류진동의 특징을 분석하였다. 기류가사화 장비를 통한 유동장 관찰을 통해 교량의 병렬배치와 간격이 기류에 미치는 영향을 평가하였다. 기류가시화 실험 결과 후류에 단면이 위치함으로써 두 교량 사이에서 단면의 진동에 동조한 와류가 발달하여 양측 교량 모두에 영향을 주었다. 상대적으로 가까운 간격에서는 양 단면에서 증폭된 와류진동이 나타나지만 간격이 단면 높이의 5~7 배 이상 떨어지게 되면 풍상측의 교량은 빠르게 간섭현상을 잃어버리고 단독으로 위치했을 때의 사태로 회귀하였으며 풍하측의 교량은

관찰한 최대 간격에서도 풍상측 교량으로부터 떨어져 나오는 와류의 영향을 받았다.

일련의 실험을 통해 와류진동에 취약한 간격은 풍상측 단면에서 떨어져 나오는 와류가 단면이 진동하는 한 주기 동안 이동하는 거리와 밀접한 관계가 있다는 것을 밝혔다.